Master Thesis, Department of Geosciences

Ozone suppression of carbon uptake by vegetation

A model study of the effect of ozone on carbon uptake and storage in boreal forests in northern Europe

Kjetil Schanke Aas

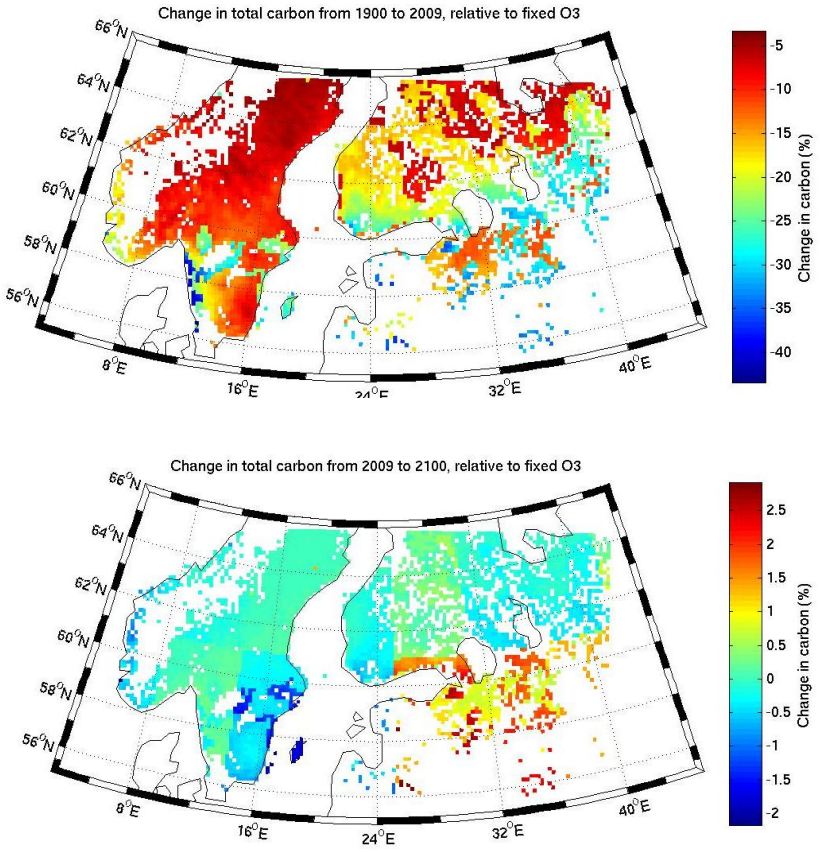

UNIVERSITY OF OSLO

FACULTY OF MATHEMATICS AND NATURAL SCIENCES

Ozone suppression of carbon uptake by vegetation

A model study of the effect of ozone on carbon uptake and storage in boreal forests in northern Europe

Kjetil Schanke Aas

Master Thesis in Geosciences

Discipline: Meteorology

Department of Geosciences

Faculty of Mathematics and Natural Sciences

University of Oslo

01.06.2012

Abstract:

Ozone is known to have adverse effects on both humans and vegetation and to affect the climate through its direct radiative forcing. In addition, recent studies have shown that ozone has an indirect effect on the climate as well, by suppressing the carbon uptake into vegetation. The purpose of the present study is to shed light on what past, present and future ozone concentrations mean for the radiative balance of the atmosphere through their suppression of CO2 uptake into vegetation, with a special focus on boreal forests in northern Europe.

With this purpose in mind, a regional climate model coupled with chemistry (WRF-chem) is used to simulate ozone concentrations in northern Europe for the year of 2009. The resulting concentrations are compared with observations from the EMEP network, and subsequently used in a land surface model (NoahMP) in off-line mode, adopted to include ozone effects on plants. The NoahMP model is validated with measurements from the SMEAR II station, and used to simulate changes in total stored carbon in the boreal forests of northern Europe. In addition, results from the OsloCTM simulations are used to produce concentrations representative for the year 1900, and the year 2100 according to the SRES A2 scenario.

The changes in total carbon compared to simulations without ozone effects show a clear impact of ozone for present day concentrations, resulting in a considerable reduction in stored carbon. The increase in land carbon from 1900 to 2009 from increased atmospheric CO2 is found to be considerably reduced due to increased ozone concentrations, whereas for the 2100 simulations the results show a reduced effect of ozone, even for the areas with substantial increase in ozone concentrations, due to reduced stomatal conductance, as a result of increasing CO2 concentrations.

Acknowledgements:

First of all, I would like to thank my supervisor Frode Stordal for his encouragement, guidance, as well as interesting and fruitful discussions. Thanks also to my co-supervisor Terje Berntsen for valuable help and comments along the way.

Secondly, I wish to say thank you to my fellow students and friends at MetOs, especially to Johanne Rydsaa for teaching me to use the WRF-chem model and for always taking time to answer questions or discuss problems, and to Øivind Hondebrog for great help with the WRF model and for providing data from the OsloCTM. Thanks also to Gunnar Wollan for help with a variety of computer issues.

A sincere thanks also to Dr. Guo-Yue Niu for providing me with a version of the NoahMP model before it became publicly available, and to the people at the Division of Atmospheric Sciences at the University of Helsinki, for providing measurements from the SMEAR II station in Hyytiälä, Finland.

Thanks also to Dr. Daniel Rasse and his fellow researchers at Bioforsk for great help with interpreting the NoahMP results and discovering unrealistic parameter values in the model.

Last, but not least, a huge thanks to my lovely wife, Selja. This thesis could not have been completed without your encouragement, understanding, and practical help in looking over the language of the thesis.

Oslo, 01.06.2012
Kjetil S. Aas

Contents

1. Introduction

The earth's temperature and climate are controlled by the balance of incoming solar radiation and outgoing longwave radiation. Of key importance in this balance are the gases and particles that act to absorb, scatter, or reflect radiation in the atmosphere, thereby altering the amount of radiation received by the earth's surface. A valuable concept in determining their effect on climate is therefore the radiative forcing (RF) of a gas or a particle, defined by the IPCC as "the change in net (down minus up) irradiance (solar plus longwave; in W m–2) at the tropopause after allowing for stratospheric temperatures to readjust to radiative equilibrium, but with surface and tropospheric temperatures and state held fixed at the unperturbed values" (IPCC, 2001). RF is thus a measure of how a gas or a particle effects the net radiation at the tropopause. A perturbation to the radiation balance will then lead to a climate response that will at some point establish a new balance. In first order, a positive RF will act to increase the temperature in the troposphere, and thereby increase the intensity of the outgoing longwave radiation until the balance is restored. The total climate response to a change in radiation is, however, much more complicated than this, and involves many, and sometimes poorly understood feedback mechanisms in the earth system. RF is therefore often used to evaluate and compare the effect of different human and natural changes to the climate system, as it can be determined with a relatively high level of certainty.

Since the pre-industrial time (around 1750), carbon dioxide has proven to be the most important pollutant in terms of RF. Its increase from 280 ppb around 1750 to around 380 ppb in 2005 is estimated to have an RF of 1.66 W/m^2 (Denman et al., 2007). Understanding what happens to this extra CO_2 in the atmosphere and how it enters the carbon cycle as a whole, is therefore of great importance in understanding climate change. In addition to getting good estimates of how much CO_2 is emitted, we must understand the processes that can alter the sinks of atmospheric CO_2. Here recent studies suggest that ozone could be of importance (Collins et al., 2010; Sitch et al., 2007). In addition to being a greenhouse gas (GHG) in itself, with an estimated RF of 0.35 W/m^2 in 2005 (Forster et al., 2007), ozone is a toxic gas that is damaging to both humans and vegetation. By limiting plant growth through its damaging effect on plant tissue, ozone suppresses the uptake CO_2 by vegetation. Sitch et al (2007) estimated that the radiative forcing of this extra amount of CO_2 in the atmosphere due to ozone damage to vegetation could be of the same magnitude as, or even

higher than, the direct radiative forcing of ozone. Research on this indirect RF of ozone through suppression of CO_2 uptake is, however, at an early stage.

The purpose of the present study is to further develop the understanding of this indirect radiative forcing of tropospheric ozone. The underlying question is what past, present and future ozone concentrations mean for the radiative balance of the atmosphere, through their suppression of CO_2 uptake into vegetation. This main question is, however, considered to be too extensive to be addressed here in its entirety, and we will therefore focus on the following narrower, but related, questions:

- What is the effect of ozone on the yearly uptake of CO_2 to evergreen needle leaf forests in northern Europe in the year 2009?
- What would be the steady state change in total land carbon in this ecosystem due to the above described ozone effect?
- How large would similar changes be in the year 1900, and in year 2100 under the SRES A2 scenario?

By looking at the year 2009, we want to attain an estimate that is representative for the present day ozone damage. Choosing one calendar year allows us to have a temporal resolution that can capture both diurnal and seasonal variations. Narrowing down the spatial domain to northern Europe makes it possible to get a high enough resolution to capture more local differences than could be done with a global model. The area is, however, still large enough to be able to represent a considerable area of the world's boreal forests, which together contain about 23 % of the total land carbon (IPCC, 2000b).

The structure of this thesis is as follows: Chapter 2 focuses on the carbon cycle, the tropospheric ozone chemistry and how they relate to climate change. In chapter 3 the modeling tools used in this study are described, along with the observations and measurements used to validate the models. Chapter 4 presents the test results with the subsequent adjustments and tuning of the models, the results from the final simulations, and a discussion of these. Finally, in chapter 5, the results from this study are summarized and some suggestions for further research in this topic are presented.

2. Theory

2.1 The carbon cycle

Much attention has been given to study the earth's carbon cycle to understand how different carbon reservoirs are changed by human activities. Figure 2.1, taken from IPCC's fourth assessment report (Denman et al., 2007), shows the sizes of the different carbon reservoirs in the earth system, and the fluxes between them. The red arrows and numbers represent the human perturbation to the system, which comes from changes in the land use (such as deforestation and agriculture) and burning of fossil fuels. This carbon is then emitted as CO_2 to the atmosphere, which has led to an increase in atmospheric concentrations from around 280 ppm in 1750 to nearly 380 ppm in 2005 (Denman et al., 2007). This increase has led to increased uptake of CO_2 by both vegetation and ocean. The fraction of human emitted carbon that accumulates in the atmosphere ('the air born fraction') is about 45 %. This percentage has been relatively stable since the 1950's, despite increasing atmospheric concentrations and increasing emission rates (Denman et al., 2007).

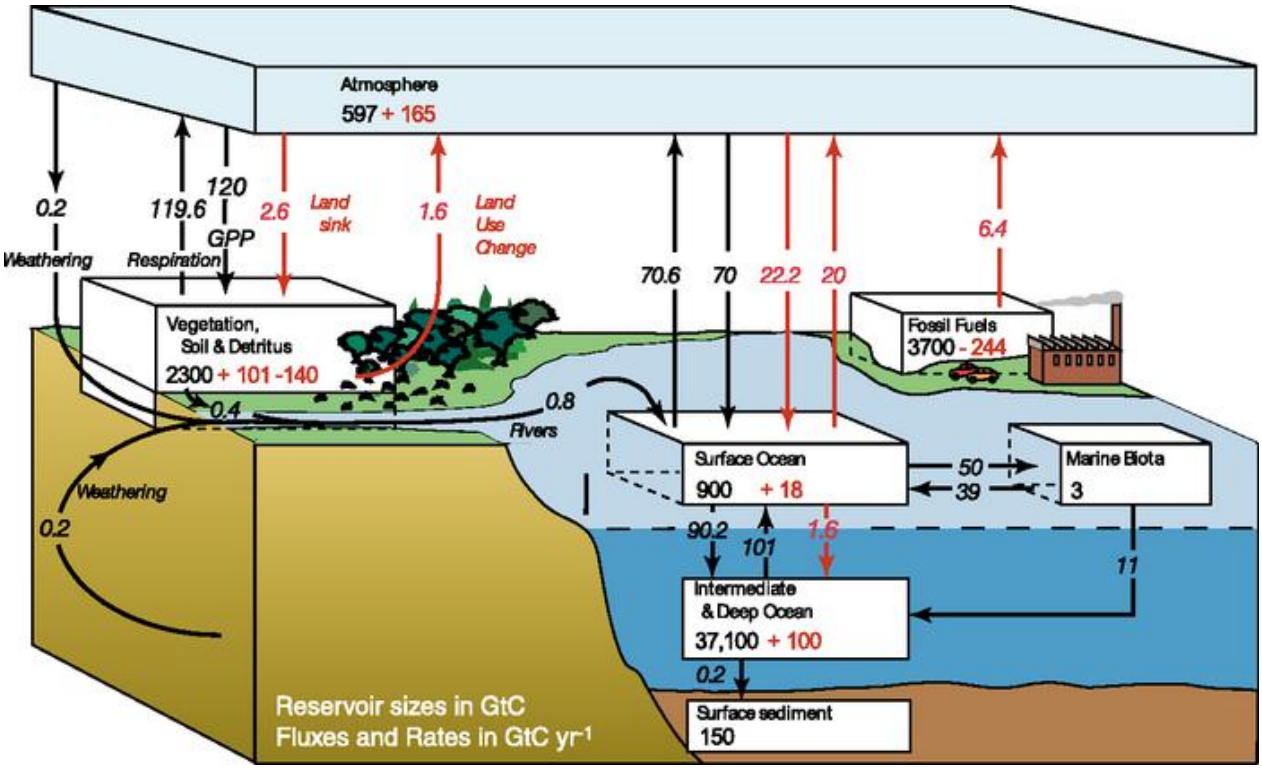

Figure 2.1: The global carbon cycle for the 1990s with "natural" reservoirs and fluxes in black and the "anthropogenic" fluxes and reservoir perturbations in red. From Denman et al. (2007)

2.1.1 Atmosphere – ocean exchange

The exchange of carbon between the ocean and the atmosphere happens in two main processes. First atmospheric CO_2 can be dissolved in the ocean to form bicarbonate (HCO3-) and carbonate (CO3-) ions, known as dissolved inorganic carbon (DIC) (Denman et al., 2007). Cold, DIC-rich surface water sinks to the deep oceans at certain locations at high latitudes during winter, and rises slowly in the rest of the ocean, especially in the tropics. In the warm conditions of the tropics the solubility of CO_2 is lower, and it is released back into the atmosphere. Secondly, CO_2 is taken up by the surface waters through plankton photosynthesis, forming particulate organic carbon (POC). A fraction of this POC sinks to the deep oceans and accumulates in the sediments, but most POC is oxidized to DIC either at the surface or in the deeper parts of the ocean. These two processes together contribute to a gradient of DIC ranging from high concentrations in the deep oceans to low concentrations in the surface oceans. Both of these processes could be affected by future climate change. First of all, changes in temperature, and sea ice formation and melting, could alter the intensity of the ocean circulation (Dickson and Osterhus, 2007). A slowing down of the deep water formation would decrease the uptake of ocean CO_2. Also, it would lead to a slower accent of nutrition to the surface, leading to less plankton activity. Plankton activity is also determined by available sunlight, which can also change in a future climate with different cloud coverage.

2.1.2 Atmosphere – land surface exchange

The terrestrial ecosystem carbon reservoirs, which will be referred to as the land surface carbon or the land carbon, make up the other great reservoir of carbon that interacts with atmospheric carbon. In the present study this reservoir is divided into vegetation and soil, where vegetation is the living part of the land carbon and soil is the dead part, which is the litter from the vegetation and the by-products of this[1]. In the model simulations the vegetation will be divided into leaves, wood and fine roots, and the soil carbon into different soil carbon pools. In the model simulations, the leaf carbon is directly linked to the Leaf

[1] 'living' and 'dead' are not entirely accurate terms in this context, as there is much life in the soil apart from the roots, and the whole wood part of the plant is not necessarily 'living' in the sense that it contributes to vegetation respiration.

Area Index (LAI), defined as the one sided average leaf area per unit area at the ground (Nobel, 2005). The total amount of carbon assimilated through photosynthesis is called the Gross Primary Production (GPP). Both vegetation and soil loses carbon back to the atmosphere through respiration. The vegetation respiration, also known as autotrophic respiration, consists of maintenance respiration and growth respiration. Subtracting this autotrophic respiration from the GPP gives the Net Primary Production (NPP), whereas subtracting in addition the soil respiration, also known as heterotrophic respiration, gives the Net Ecosystem Exchange (NEE). In addition to respiratory losses, the land surface loses carbon as volatile organic compounds (VOC), CH4 and dissolved organic carbon, in addition to harvests, forest fires and erosion (Luyssaert et al., 2007). To describe the sum of all processes that contribute to carbon exchange between the land surface and the atmosphere, the term Net Ecosystem Carbon Balance (NECB) is commonly used (Luyssaert et al., 2007). These processes will, however, not be the focus of the present study, and hence the results presented will be based on GPP, NPP, NEE, and their influence on the land surface carbon.

The fluxes of carbon described above can change both as a result of changing climatic conditions, changes in atmospheric composition, and changes in land use (Denman et al., 2007). The changes in carbon fluxes due to changes in climate are difficult to predict, as responses to a change in one parameter can have different signs and magnitudes in different locations. Increase in temperature and soil moisture can, for instance, increase heterotrophic respiration in well-aerated soils, but decrease it in wet soils (Denman et al., 2007). Increase in atmospheric CO_2 concentrations on the other hand, has a more definite effect on uptake to vegetation. Free air CO_2 enrichment experiments (FACE) and chamber studies both show an increase in CO_2 uptake with elevated atmospheric CO_2 (Denman et al., 2007). With a 50% step increase in ambient concentrations, eleven FACE studies showed an average increase in net primary productivity (NPP) of 12%, with higher values for woody plants (Denman et al., 2007). This CO_2-fertilization is, however, believed to be limited by the availability of nutrition and can therefore reach a saturation point at a certain CO_2 concentration, with further increase having little effect on plant growth. Still, the changes in land use probably have the greatest effect on land carbon storage, and consequently atmospheric CO_2 concentrations. Deforestation, mainly in the tropics, contributes to up to one third of the total anthropogenic emissions (Denman et al., 2007). In addition, forest fires, both natural and manmade, release CO_2 and CH4 to the atmosphere. These two processes are, however, to some extent compensated for by forest regrowth and new agricultural practices that bind

more soil carbon. Due to more efficient farming methods, large areas at middle and high latitudes that used to be cultivated land are now open for forest growth (Denman et al., 2007. In addition to this, new techniques in forest management also give higher carbon contents per area. Finally, carbon uptake can also be limited by the presence of other air pollutants limiting plant growth, such as ozone. Ozone's suppression of photosynthesis is the central process that is the focus of in this thesis, and its mechanisms will be looked at in more detail in chapter 2.3. There has not been much research to quantify this effect before, but first estimates suggest that ozone will on a global scale reduce the effect of CO_2-fertilization by 17-31% in 2100 (Sitch et al., 2007).

2.2 Tropospheric ozone

Ozone is in itself the third most important GHG, after CO_2 and CH4 (Forster et al., 2007). Being a toxic gas that damages biological tissue, it has also an adverse effect on both humans and vegetation. Before we look closer at its impacts on vegetation and its photosynthetic ability in Chapter 2.3, we will briefly look at the main chemical processes that control its concentrations in the troposphere.

Ozone is not emitted directly to the troposphere, but is a secondary pollutant formed through a complex interaction with different chemical species in the presence of sunlight. The main components contributing to ozone production are NO_x ($NO + NO_2$) and volatile organic compounds (VOC), in the following including CO and CH4. These so called ozone precursors exist naturally in the atmosphere, but they have increased greatly in concentration due to human activities. NO_x, which is produced naturally in lightning and forest fires, is now between 3-4 times more abundant in the troposphere as a global average than pre-industrial levels, with large spatial and temporal differences (Denman et al., 2007). This is mainly due to fuel combustion and increased biomass burning. CO and CH4 have in the same time period increased 3-4 and 2-3 times respectively (Denman et al., 2007; Jacob, 1999). In addition to chemical production, there is also a net influx of O_3 from the stratosphere of about 540 Tg per year (Fowler et al., 2008). This accounts for roughly 10% of the total production of ozone in the troposphere. Ozone is lost in troposphere mainly by chemical means. In addition, dry deposition is the other major sink of ozone in the troposphere, estimated to be about 1000 Tg per year, or 20% of the total loss (Fowler et al.,

2008). Together the two loss mechanisms give ozone an average lifetime of 1-2 days in the planetary boundary layer where the dry deposition takes place, and several weeks in the free troposphere. The relatively long lifetime in the free troposphere, combined with the fact that ozone can be produced away from its precursors' sources makes it not only a regional but also a global problem.

2.2.1 The Ozone chemistry

The ozone chemistry is highly dependent on hydroxyl, which is formed by the photolysis of ozone and the subsequent reaction of atomic oxygen with water vapor (R1-R2):

R1 O3 + hv => O(1D) + O2

R2 O(1D) + H2O => 2OH

The further path of the hydroxyl in relation to ozone is in its turn highly dependent on the concentration of NO_x. There are therefore considered to be three different regimes in ozone chemistry, depending on the NO_x concentration: The very low NO_x regime with net O_3 loss, the low NO_x regime where the production of $O_3$is limited by NO_x, and the high NO_x regime where VOCs are the limiting components. The following description of the three regimes is based on that given by Fowler et al. (2008).

Regime 1: Very low NO_x

The first regime (Figure 2.2) is characterized by a net loss of O_3. VOCs like CH4 and CO oxidize to produce peroxy radicals like CH3O2 and HO2. These can then be removed through a reaction with HO2 (R3 and R4). Alternatively, HO2 can react with O_3 to regenerate HO (R5) resulting in a cyclic removal of O_3.

R3 CH3O2 + HO2 => CH3OOH +O2

R4 HO2 + HO2 => H2O2 +O2

R5 HO2 + O3 => OH + 2O2

The rate of which O_3 is removed by (R5) depends on the relative size of the reaction rates of (R4) and (R5). As decreasing O_3 concentrations decreases the reaction rate of (R5), this does not lead to rapid O_3 destruction. Altogether the ozone destruction rate in this regime is relatively small compared to the formation rates in the next two regimes. Still, it is important because it occurs over large regions, such as the remote ocean areas in the Southern Hemisphere.

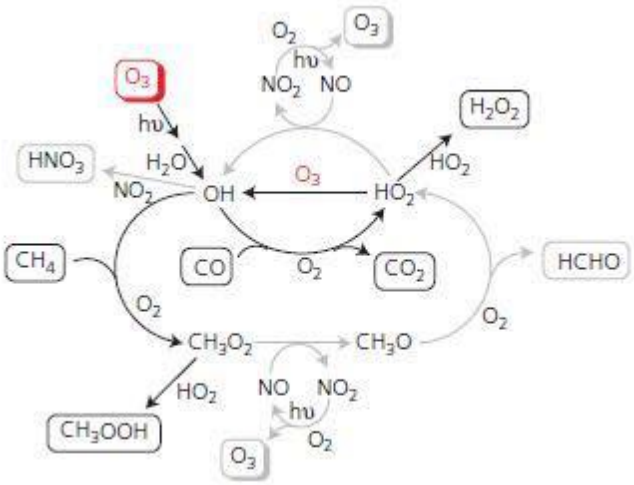

Figure 2.2 Schematic overview of the ozone production and loss mechanisms in the very low NO_x regime. From Fowler et al. (2008)

Regime 2: low NO_x

The second regime (Figure 2.3) is characterized by net production of O_3. As in regime 1 peroxy radicals are formed by VOCs reacting with OH. However, in the presence of NO, these can also react to form oxy radicals and NO_2 (R6 and R7).

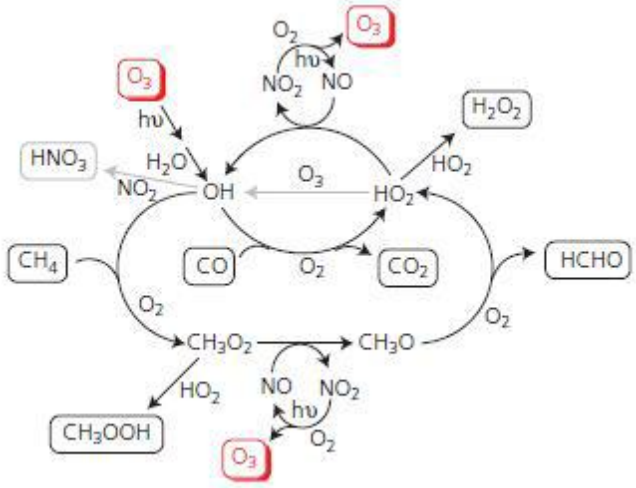

Figure 2.3 Same as Figure 2.2, but for the low NO_x regime.

R6 CH3O2 + NO => CH3O + NO2

R7 HO2 + NO => HO + NO2

NO_2 is then photolyzed, and creates O_3 by reactions R8 and R9, where 'M' denotes an external colliding molecule necessary for the reaction:

R8 NO2 + hv => NO + O(3P)

R9 O(3P) + O2 + M => O3 +M

As can be seen in Figure 2.3, this forms a cycle in which O_3 is produced. The rate of which O_3 is formed in this regime is dependent on how fast reactions R5 and R6 are going compared to reactions R3 and R4 respectively, which is determined by the abundance of NO_x. This regime is therefore often referred to as 'NO_x limited'. Although VOCs are also needed to complete the cycle, the formation rate of ozone in this regime is insensitive to its concentrations as there are no competing reactions to terminate them.

Regime 3: high NO_x

When the concentration of NO_x reaches a certain level OH starts reacting with NO_2 to create nitrogen acid (HNO3):

R10 OH + NO2 + M => HNO3 + M

Further increase in NO_x concentrations now leads to removal of OH, which terminates the cycle (see Figure 2.4[2]). The production of O_3 is then dependent on OH reacting with VOCs rather than NO_2, making VOCs the limiting factor. This regime is therefore referred to as 'VOC limited'. This regime can be found in urban areas where NO_x emissions are high.

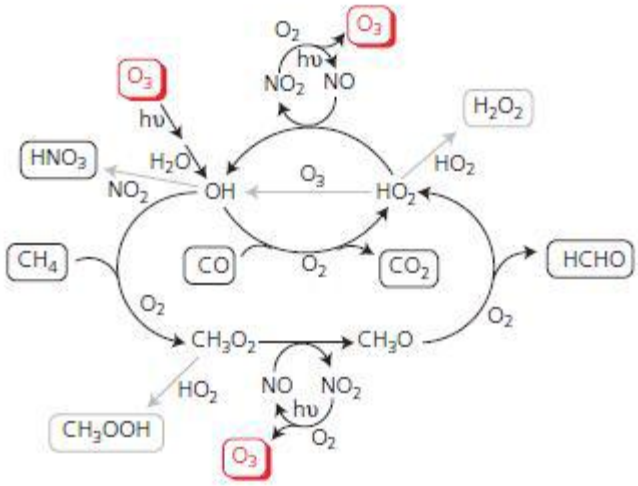

Figure 2.4 Same as Figure 2.2, but for the high NO_x regime.

The effect of these different regimes is that there is a strong non-linearity in the O_3 production's dependence on its precursors NO_x and VOC. The kind of control mechanism that will work to reduce O_3 concentrations is therefore strongly dependent on the regime you are inn. In some cases, a reduction of one O_3 precursor (NO_x) can actually lead to an increase in O_3 concentration. This is, however, seldom the case on a regional or global scale, but can be the case in certain urban areas.

[2] In this figure the arrow from OH to HNO3 should be black, not gray, indicating that this reaction is important in this regime.

2.3 Ozone effect on plants

The damage caused by ozone to vegetation is associated with the uptake of ozone through stomata (Mills et al. 2010). This uptake can have a series of adverse effects on the plant, ranging from acute visible injury to reduction in photosynthetic rates and accelerating leaf senescence (Ashmore, 2005). For plant species grown for sale at a local market it is obvious that the first effect is a great problem. There have been reported cases where entire crops could not be sold, due to damages from ozone, carrying severe economic implications for local farmers (Ashmore, 2005). Seen in the context of global carbon balances the latter effects are, however, of greater importance and must be looked more closely at.

Much work have been done to examine and quantify the effect that ozone has on plant biomass. As it was realized that ozone damage on vegetation is linked to the actual stomata uptake and not just the ambient concentration, we have seen a shift over the last 10 years from focusing on concentration measurements, such as the AOTx (ozone concentration accumulated over a threshold of X ppb), to calculation of accumulated stomata uptake, such as the PODy (the phototoxic ozone dose over a threshold flux of Y nmol m^-2 PLA s^-1) (Mills et al., 2011). In relation to the LRTAP convention, critical dose levels for when damage occur, as well as dose-response functions, have been developed for a set of agricultural and horticultural crops, forest trees and (semi-)natural vegetation (Mills et al., 2010). This work has been conducted by leading European experts, and represents the current "state of knowledge" about ozone damage to vegetation. They have found 1 nmol m^-2 PLA s^-1 to be the best estimate of the threshold flux, above which damage occurs for birch, beech and Norway spruce. For birch and beech, a 4% annual reduction in whole tree biomass is found for an accumulated dose of 4 mmol m^-2 PLA over a growing season (POD1 of 4). For Norway spruce, which is found to be less ozone sensitive, a 2% reduction was found for POD1 of 8. The POD1 (threshold flux of 1 nmol m^-2 PLA s^-1) is lower than what was used by Sitch et al. (2007). This is, however, based on more recent work that suggest that damage occurs at lower fluxes than the 1.6 threshold used by Sitch et al (2007). In fact, POD0 and POD1 corresponded equally well with observed damages. However, the threshold has been set to 1 based on "expert judgement" and the fact that there is "strong biological support for the use of a threshold to represent the detoxification capacity of the threes" (Mills et al., 2011). It should also be mentioned that the scientific certainty of the response functions was lower (lower R^2 for the linear regression) for trees than for other plant types. In fact, some studies have showed increase in stem growth under elevated ozone

concentrations for some tree species, although these findings were not statistically significant (Manninen et al., 2009).

In addition to tree biomass reduction being linked to ozone flux, reports from the Aspen FACE experiment have shown reduction in soil carbon as well (Loya et al., 2003). When CO_2 and ozone concentrations were both increased by 50% compared to ambient air, Loya et al. found a 50% reduction in acid-insoluble soil carbon, relative to the amounts of carbon entering the soil when only CO_2 concentrations were increased. This indicates that the increase in soil carbon storage from increased CO_2 concentrations expected in a future climate will, to some extent, be offset by increase in ozone concentrations.

2.4 Modeling ozone uptake

In contrast to estimations of ozone concentrations, stomata flux of ozone is difficult to measure directly in the field, and must therefore be estimated through modeling. Chemistry models are also important for making prognoses of future concentrations of atmospheric gases. We therefore need to look closer at how uptake of different trace gases can be modeled. A widely used approach in determining the rate at which a gas or particles are taken up by the land surface (the deposition velocity, Vd) is the multiple resistance analogy (Hicks et al., 1987; Wesely, 1989), as illustrated in Figure 2.5. The trace gas at a given reference height in the atmosphere must go through different resistances in series or in parallel, in the same way as in electricity, before being deposited on the ground. The deposition velocity is defined as

$$Vd = -\frac{F}{C}, \qquad 2\text{-}1$$

where F is the total flux, usually in mol/m^2/s, and C is the concentration in mol/m^3. Negative flux is defined as flux from the atmosphere to the ground. In the resistance analogy the deposition velocity is then the inverse of the sum of the resistances, when the resistances are in series:

$$Vd = \frac{1}{Ra + Rb + Rc} \qquad 2\text{-}2$$

Here Ra represents an aerodynamic resistance that is determined by atmospheric properties, such as turbulent exchange, Rb represents a quasi-laminar boundary layer resistance in the vicinity of the receptor surfaces, affected by the molecular diffusivity, and Rc is the bulk surface, or canopy resistance that combines all uptake processes of different surface elements (Hicks et al., 1987). Figure 2.5 shows these resistances schematically, including one example of the different pathways that make up the total surface resistance Rc. This figure is taken from Wesely (1989) who was the first to present a detailed parameterization of the different surface resistances for different gases. This parameterization has been implemented in many chemical transportation models (CTMs) and is also used in some of the chemistry schemes in the Weather Research and Forecasting model (WRF-chem) used in this study. In short, the different surface resistances are according to Wesely (1989) found as follows:

The stomatal resistance (Rs) is calculated as a minimum stomatal resistance (Ri) modified by a factor accounting for the amount of solar radiation (G) and one accounting for temperature (Ts):

$$Rs = Ri * (1 + (200(G + 0.1)^{-1})^2) * \left(400\left(Ts(40 - \mathrm{Ts})\right)^{-1}\right) \qquad 2\text{-}3$$

The buoyant convection in canopy transfer resistance (Rdc) is dependent on G and the slope of the local terrain in radians (θ):

$$Rdc = 100(1 + 1000(G + 10)^{-1})(1 + 1000\theta)^{-1} \qquad 2\text{-}4$$

Ri, Rlu, and Rac, in addition to Rgs and Rcl for both ozone and SO2 are given as table values for eleven different land use categories and five different growing seasons. The leaf mesophyll resistance (Rm), is taken to be zero for both ozone and SO2. For other gases, Wesely proposes that Rm, Rlu, Rcl and Rgs can be found using the values for ozone and/or SO2, Henrys law constant (H*), and a reactivity factor (f0). The conductances (inverse of the resistances) are then found as the sum of a solubility term dependent on H* (dominating for soluble gases) and a reactivity term dependent on f0 (dominating for highly reactive gases). Although this parameterization gives individual values for the different resistances, it is not meant to be accurate at that level of detail. Instead, Wesely (1989) clearly says that several of the individual resistances have been adjusted to give a realistic total surface resistance rather than giving realistic individual estimates.

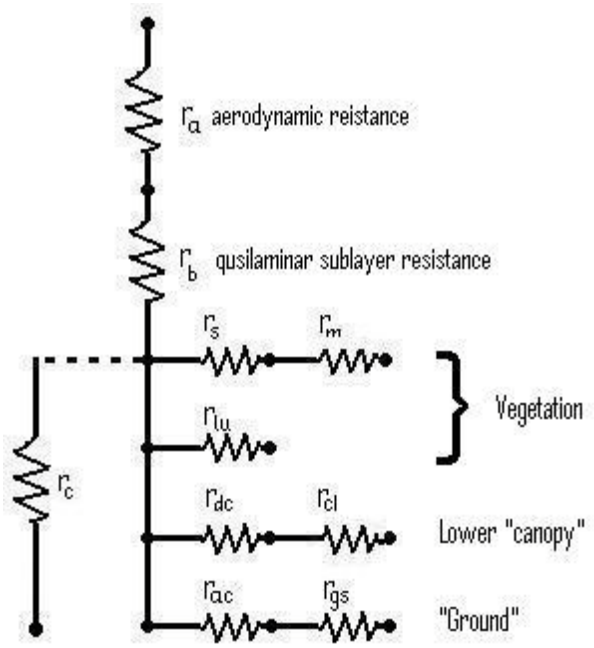

Figure 2.5: Schematic overview of the resistances used in the Wesely scheme. Modified from Wesely (1989)

Of special interest when modeling stomatal fluxes is the way stomatal resistance is parameterized. Here much work has been done and much more sophisticated methods are available than the one used by Wesely. There are two different main approaches when modeling this (de Beeck et al., 2007). The first possible approach, introduced by Jarvis (1976), finds stomatal conductance by multiplying a maximum stomatal conductance with different functions giving values between 0 and 1. These functions represent stomatal closure as a response to lack of sunlight, water pressure deficit (VDP), lack of available soil moisture, etc. Each factor is dependent on one variable alone, making the total stomatal conductance linearly dependent on each of these functions with no interactions between them. The Wesely scheme can be seen as using a simple form of this approach, taking into account radiation and temperature alone.

The second possible approach is more mechanistic, linking stomatal conductance to the photosynthesis and transpiration (de Beeck et al., 2007). A widely used, and much further developed, method of this kind is the Ball-Berry model (Ball et al., 1987). A version of this will be described in more detail in Chapter 3.1.2 as part of the description of the Noah-MP model. In brief, however, this method can be described as having a linear relationship between stomatal conductance and the rate of photosynthesis (An) divided by the CO_2

concentration at the leaf surface and multiplied with the relative humidity at the leaf surface (Ball et al., 1987). In this approach, radiation, canopy temperature, and in more recent versions; foliage nitrogen and soil moisture, are accounted for by their influence on An.

3. Methods and Data

In the study of tropospheric ozone and its impact on the carbon cycle we have used two modeling tools: the Weather Research and Forecasting model coupled with chemistry (WRF-chem) and the Noah land surface model with multiparameterization options (Noah-MP LSM). We used the WRF-chem model to produce meteorological data and ozone concentration fields. The Noah-MP model was then run offline with the input from WRF-chem to get a closer look at the vegetation and carbon cycle than was possible using the WRF-chem model alone. In the following we will describe each of these two models including two augmentations to the Noah-MP model involving soil carbon and ozone damage, before we look at the measurement data used to validate and adjust the model.

3.1 Models

3.1.1 WRF-Chem

WRF is a community numerical weather prediction (NWP) model that is used in both operational weather forecasting and for research and educational purposes around the world (Skamarock et al., 2008). It can be used with two different dynamical solvers: The Advanced Research WRF (ARW) and the Nonhydrostatic Mesoscale Model (NMM). In this study the ARW was used, which is mainly developed at the National Center for Atmospheric Research (NCAR), who also has the community support for it. It uses fully compressible non-hydrostatic equations, complete coreolis and curvature terms, mass-based terrain-following coordinates, and has the option for both nesting and grid analysis or observation nudging among its key features (Wang et al., 2012). The version used in this study was ARW3.3, which was released in April 2011 (Wang et al., 2012).

The chemistry part of the model is online with the rest of the WRF model (Wang et al., 2012). It has several choices for gas-phase chemical reaction schemes, includes dry deposition, and has the option of including both biogenic and anthropogenic emissions. Figure 3.1 shows the flow chart for the ARW modeling system including the chemistry part. As can be seen in the figure, the modeling system has three main parts. The WRF Pre-Processing System (WPS), which defines the simulation domains, interpolates terrestrial data, and incorporates meteorological data from another model to be used in WRF (Wang et al., 2012). The WRF-Var is the variable data assimilation part which can be used when

observational data are to be combined with the meteorological data from the WPS. This option has not been used in this study. Finally, there is the WRF-ARW model. It first creates initial and boundary condition files from the WPS output ('Real Data Initialization'), and then performs the actual simulation ('ARW MODEL'). For the initial and boundary conditions for the chemistry, one can either use a standard profile, coded into the model, or read it in from another chemistry model. In this study, data from the OsloCTM2 model (Sovde et al., 2008) was used as initial and boundary conditions for the chemistry. These where read in with the CTMBC program developed by Øyvind Hodnebrog (Hodnebrog et al., 2012). For biogenic emissions, the online MEAGAN option was used, whereas for anthropogenic emissions TNO-MACC data (Kuenen et al., 2011) was used. This was read in with another program developed by Hodnebrog (Hodnebrog et al., 2012). Also, data from the Oslo-CTM2 model was used to update the total column of ozone above -the top model level in WRF to produce better calculations of photolysis.

The RADM2 chemical mechanism (Stockwell et al., 1990) without aerosols was used for the chemical simulations. This scheme was chosen, because it balances accuracy and computational speed in a good way (Hodnebrog, 2008), and because it works with the above mentioned improvements and programs for using the Oslo-CTM2 data.

For meteorological initial and boundary conditions, ECMWF-IFS data with 0.25 x 0.25 degree resolution was used (ECMWF, 2009). Because of problems with the sea surface temperature (SST) data from ECMWF, these were taken from NCEP/MMABs[3] global SST analysis available online (NCEP/MMAB, 2012). In addition, the new feature to calculate skin SST in the model was used (Zeng and Beljaars, 2005).

[3] National Centers for Environmental Prediction/Marine Modeling and Analysis Branch

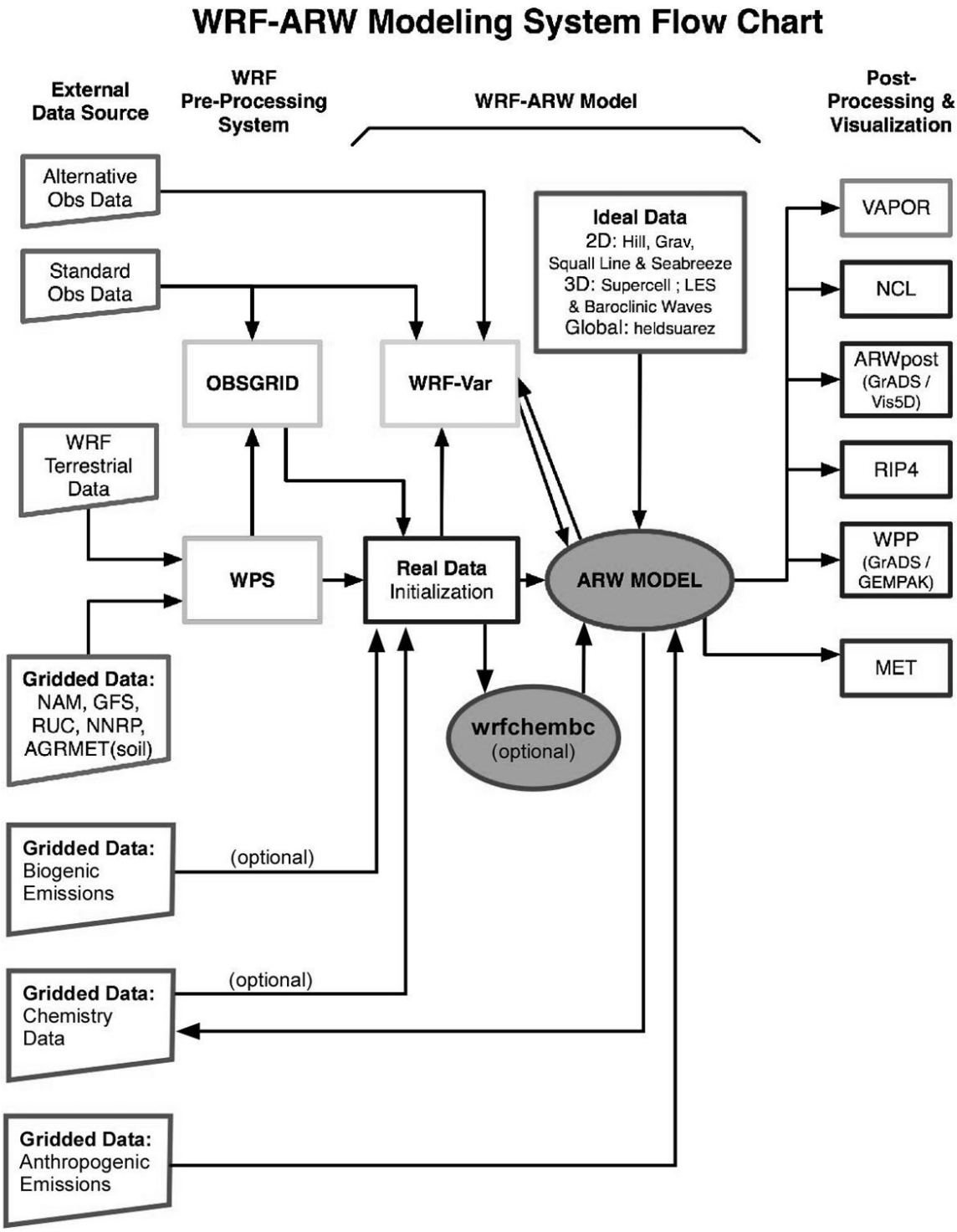

Figure 3.1: WRF Modeling System flow chart. From Wang et al. (2012)

3.1.2 NoahMP

The Noah LSM is a community land surface model, which has been developed over time with many different contributors. It is one of the options for LSMs in the WRF model, in addition to being a standalone offline surface model, needing only a set of atmospheric forcing data to run.

Noah LSM is based on the OSU LSM developed in the 1980's (Mitchell, 2005). The OSU LSM was chosen out of several different LSMs to be the one to be further developed by the Environmental Modeling Center (EMC) at NCEP in the 1990's, to find a "modern-era LSM suitable for use in the NCEP operational weather and climate prediction models" (Mitchell, 2005). In year 2000 it was named "Noah" after the main contributors[4] to its development.

Over the last couple of years, several new features have been added to the Noah LSM, resulting in a model that has multiple parameterization options for a set of physical processes called Noah-MP (Jiang et al., 2009; Niu et al., 2011; Yang et al., 2011). An offline, non-public version, of this model was kindly provided by Dr. Guo-Yue Niu at the University of Texas at Austin for use in the present study, for which the most important one of the new features was the implementation of dynamical vegetation (DV) based on the work of Dickinson et al (1998). This DV model includes simulation of carbon uptake, storage, and release, in different parts of the vegetation. This was needed to calculate changes in the total land carbon in response to ozone. We will therefore look more closely at this part of the model, both as it was originally described by Dickinson et al (1998), and as it was implemented in the Noah-MP model used in this study. We here follow Dickinson et al (1998) when describing the original formulation, and Niu et al. (2011) for the Noah-MP implementation. In addition, some numbers and equations not described in these articles have been looked up in the code.

Dickinson's DV model

Dickinson's DV model calculates carbon uptake and allocation to different parts of the vegetation and carbon losses back to the atmosphere through respiration (Dickinson et al., 1998). It divides the total land carbon into three living carbon pools (leaf, wood and root)

[4] N: National Centers for Environmental Prediction (NCEP), O: Oregon State University (OSU), A: Air Force (both AFWA and AFRL), H: Hydrologic Research Lab –NWS (now office of Hydrologic Dev. – (OHD)

and two soil carbon pools (fast and slow). The leaf carbon budget is used to calculate LAI and greenness vegetation fraction (GVF), which is important in calculating photosynthetic rate and other surface fluxes, like heat flux and evapotranspiration. The model is thereby intended to improve simulation of atmosphere – land surface fluxes in climate models. For the present study it is, however, the carbon budgets in themselves that are of most interest. In the following, we will therefore look at the equations that govern the amount of carbon in each pool.

Carbon is taken up by the vegetation through photosynthesis, witch in Noah-MP is calculated independently form the DV option (see the description of Ball-Berry stomatal resistance below). The carbon entering the plants then passes into either leaves or the non-leaf living parts of the vegetation (wood and root). The leaf fraction of the assimilated carbon is a function of LAI, so that leaves grow quickly in the beginning of spring and then gradually more of the carbon is allocated to wood and roots with increasing LAI. The original leaf fraction (f_{cl}) function in Dickinson was:

$$f_{cl} = e^{-0.25*LAI} \qquad 3\text{-}1$$

Noah-MP uses a somewhat different function, which gives higher values of f_{cl} for low LAI and a quicker transaction to low f_{cl} with increasing LAI. For all vegetation types except 'Evergreen Broadleaf Forest' Noah-MP uses the following function:

$$f_{cl} = e^{0.01*(1-\exp^{0.75*LAI})*LAI} \qquad 3\text{-}2$$

The assimilated carbon that is not going into leaves is allocated to wood or roots, with the following equation giving the root fraction (f_r) of this carbon:

$$f_r = \beta^{-1} e^{\left(-r_w \beta \frac{C_r}{C_w}\right)} \qquad 3\text{-}3$$

Here C_w is the wood carbon, C_r is the root carbon, and r_w is a vegetation dependent approximate wood to root ratio that the equation is designed to make $\frac{C_w}{C_r}$ approach. β is an adjustable constant close to but less than 1.0.

All three living carbon pools release carbon back to the atmosphere by respiration. In Dickinson, the leaf respiration is proportional to the photosynthetic capacity. In Noah-MP, leaf respiration is a function of foliage nitrogen, vegetation temperature, LAI (proportional to

leaf mass), soil water, and a vegetation specific maximum respiration rate. Wood and root respiration is calculated in a similar manner, but without soil moisture and foliage nitrogen dependence, and proportional to the respective carbon masses instead of LAI.

In addition the maintenance respiration described above, Noah-MP calculates a separate growth respiration. It is calculated as 10% or 20% (depending on vegetation type) of the net assimilated carbon, i.e. the added carbon minus the maintenance respiration. The NPP is then found as the assimilated carbon minus the total respiration (maintenance and growth).

In addition to carbon lost through respiration, the living carbon pools are given a certain turnover time to account for loss through senescence, herbivory and mechanical means. In Noah-MP the leaf turnover coefficient is vegetation dependent, ranging from $0.5*10^{-6}$ (s^{-1}) ("evergreen needleleaf forest") to $1.8*10^{-6}$ (s^{-1}) ("irrigated cropland and pasture"). The wood and root turnover coefficients are $2.0*10^{-8}$ (s^{-1}) and $9.5*10^{-10}$ (s^{-1}), respectively. The original Dickinson formulation did not have wood turnover, and the leaf and root turnover coefficients were both $2.0*10^{-8}$ (s^{-1}).

Finally, leaves also loose carbon in response to cold or drought stresses. Originally, the total death rate by unit mass of carbon S_{cd} was calculated as:

$$S_{cd} = (S_c + S_d) * 2 * 10^{-7}\ s^{-1} \qquad 3\text{-}4$$

Here S_c and S_d are the unitless cold and drought stress factors, respectively, calculated as:

$$S_c = e^{-(T_c - T_{c0})} \qquad 3\text{-}5$$

and

$$S_d = e^{100(W_s - 1)} \qquad 3\text{-}6$$

where T_c is the canopy temperature, T_{c0} is the temperature below which rapid cold stress begins and W_s is a water stress term. Noah-MP uses similar functions, but with different, and vegetation type dependent, constants. In addition, the cold stress dying rate decreases with decreasing leaf mass. The temperature constant T_{c0} for evergreen forest was in Dickinson set to 228 K. For deciduous forest and tundra it was set to 268 K, and for all other types it was set to 278 K. The similar number in Noah-MP was 278 K (!) for evergreen needleleaf forest, which we will come back to in chapter 4.

We have now described the original three living carbon pools in Dickinson. In addition, a stem pool was added in the Noah-MP model for simulating stem-rich plants like corn (Niu et al., 2011). This acted much like the leaf pool, creating a certain stem area that was photosynthetically active. The leaf portion of the assimilated carbon (f_{cl} times the total assimilated carbon) was divided into leafs and stem. In this study, this stem portion was, however, omitted as it was taken to be irrelevant for forests. This resulted in the whole leaf portion going into the leaf carbon pool.

The soil carbon pools in the DV model are much simpler than the living carbon pools. The carbon lost from the living carbon pools through turnover and cold and drought stresses are added to the fast carbon pool. This pool loses carbon through respiration (microbial decomposition) at a rate depending on temperature and moisture, and in Noah-MP also depending on vegetation type. 10% of the carbon lost from the fast carbon pool goes into the slow carbon pool. This pool does not have loss mechanisms, and represents therefore a net carbon sink for the atmosphere, even at a steady state. This does however make it useless for actual estimations of total soil carbon. Another soil carbon model (the RothC soil carbon model described below) was therefore implemented in the Noah-MP model, replacing the fast and slow carbon pools.

Stomatal conductance in Noah-MP

As the stomatal conductance is directly linked to both carbon and ozone uptake we need to look closer at how it is calculated in Noah-MP. Noah-MP includes options to calculate the stomatal conductance with both a Ball-Berry formulation and the Jarvis formulation used in the other versions of Noah. However, since the Ball-Berry option is the only one that works with the DV calculations, it was the only option in this study. Following closely the description in Niu el al (2011), the Ball-Berry stomatal conductance formulation in Noah-MP is as follows:

$$\frac{1}{r_{s,i}} = m\frac{A_i}{c_{air}}\frac{e_{air}}{e_{sat}(T_v)}P_{air} + g_{min} \qquad 3\text{-}7$$

Here $r_{s,i}$ is the stomatal resistance for sunlit and shaded leafs ($r_{s,sun}$ and $r_{s,shd}$ respectively), m is an empirical parameter relating transpiration to CO_2 flux, A_i is the rate of photosynthesis per unit LAI (sunlit and shaded) in $\frac{\mu mol}{m^2 s}$, c_{air} is the CO_2 concentration at leaf surface, e_{air} is the vapour pressure at the leaf surface, $e_{sat}(T_v)$ is the saturation vapor

pressure inside leaf, P_{air} is the surface air pressure and g_{min} is the minimum stomatal conductance in $\frac{\mu mol}{m^2 s}$.

The total carbon assimilation (A) is the sum of the sunlit and shaded photosynthetic rates multiplied with its respective LAIs. The sunlit and shaded photosynthetic rates are calculated as:

$$A_i = I_{gs} * \min\left(A_c, A_{L,i}, A_S\right) \quad 3\text{-}8$$

Here I_{gs} is a growing season index depending on the leaf temperature and A_c, $A_{L,i}$ and A_S are the carboxylase-limited, light-limited, and export-limited (for C3 plants) photosynthesis rates per unit LAI, respectively. These are:

$$A_c = \frac{\left(c_i - c_{cp}\right)V_{max}}{c_i + K_c\left(1 + \frac{o_i}{K_o}\right)} \quad 3\text{-}9$$

$$A_{L,i} = \frac{\left(c_i - c_{cp}\right)4.6\alpha PAR_i}{c_i + 2c_{cp}} \quad 3\text{-}10$$

$$A_S = 0.5V_{max} \quad 3\text{-}11$$

Here c_i is the CO_2 concentration inside leaf cavity in pa (about 0.7 times c_{air}), o_i is the atmospheric O2 concentration in pa, PAR_i is the photosynthetically active radiation in $\frac{W}{m^2}$ per unit shaded and sunlit LAI with the factor 4.6 for converting to $\frac{\mu mol\ photons}{m^2 s^1}$. c_{cp} is the CO_2 compensation point given as $0.5\frac{K_c}{K_o}0.21o_i$ in pa, with K_c and K_o being the Michaelis-Menton constants for CO_2 and O2 respectively. α is the quantum efficiency in $\frac{\mu mol\ CO_2}{\mu mol\ photon}$. V_{max} is the maximum rate of carboxylation given as:

$$V_{max} = V_{max25}a_{v\,max}^{\frac{T_v - 25}{10}}f(N)f(T_v)\beta \quad 3\text{-}12$$

Here V_{max25} is the maximum value at 25℃. $a_{v\,max}$ is a temperature sensitive parameter set to 2.4 in the model. $f(N)$ and $f(T_v)$ are functions that mimic the effect of foliage nitrogen and metabolic break down at high vegetation temperatures, respectively. β is a soil moisture factor with three different parameterizations available in the Noah-MP model. $f(N)$, $f(T_v)$ and β all varies between 0 and 1.

For our purpose it can be useful to summarize these equations by observing that when sunlight (PAR) is abundant and we ignore variations in O2 and CO_2, the stomatal resistance is controlled by temperature, foliage nitrogen, soil moisture, and water pressure at leaf surface. In the absence of sunlight, under very dry conditions (in either soil or the air) or at too high or low temperatures the stomatal conductance goes to g_{min}.

3.1.3 The RothC soil carbon model

The RothC-26.3 (RothC) is a model to simulate turnover of organic carbon in soil (Coleman and Jenkinson, 1999). It has been developed in relation to the Rothamsted Long Term Field Experiment. In addition to being used as an independent model, it has been implemented in other models to simulate global carbon cycles, and is now used as an option in the JULES[5] (Clark et al., 2011). The following description of the model follows the description of Clark et al. (2011) unless otherwise is noted.

The RothC model has 4 soil carbon pools: Decomposable plant material (DPM), Resistant plant material (RPM), microbial Biomass (BIO) and long lived Humified (HUM) carbon pools. Litter from the vegetation is divided into DPM or RPM, with the relative portions depending on the type of vegetation. For trees the DPM part is 20% and RPM part 80%. The decomposed carbon from all four carbon pools (Rs) is then divided into BIO, HUM and a portion being released to the atmosphere as CO_2. The fraction going back to the soil (BIO and HUM) is supposed to be a function of clay content (Coleman and Jenkinson, 1999). In our implementation this was however taken to be a fixed fraction of 0.23, corresponding to 30% clay in the soil, as this parameter was not found in the Noah-MP model. As can be seen from Figure 3.2, 30% clay content is a representative value for a large range of soil characteristics, with the exception being soil with very low clay content. The non- CO_2 carbon is divided with constant portions of 46% and 54% to BIO and HUM, respectively. Figure 3.3 shows the carbon pools and their interactions schematically. Also shown in that figure is the inert organic matter (IOM) pool, which is not simulated in this study.

[5] Joint UK Land Environment Simulator

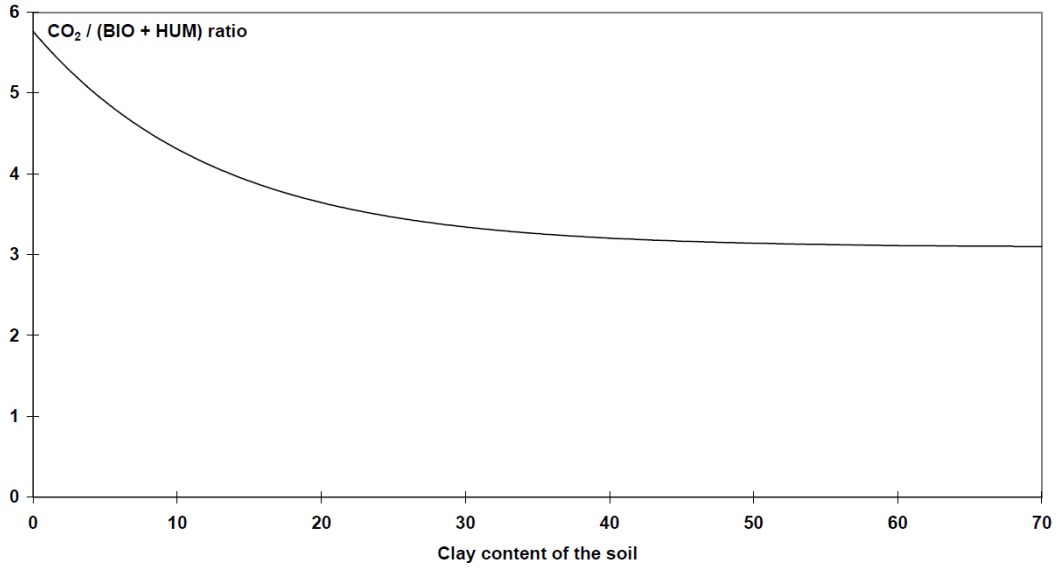

Figure 3.2: CO_2 to (BIO+HUM) ratio as a function of clay content in the soil in the original RothC soil carbon model. From Coleman and Jenkinson (1999)

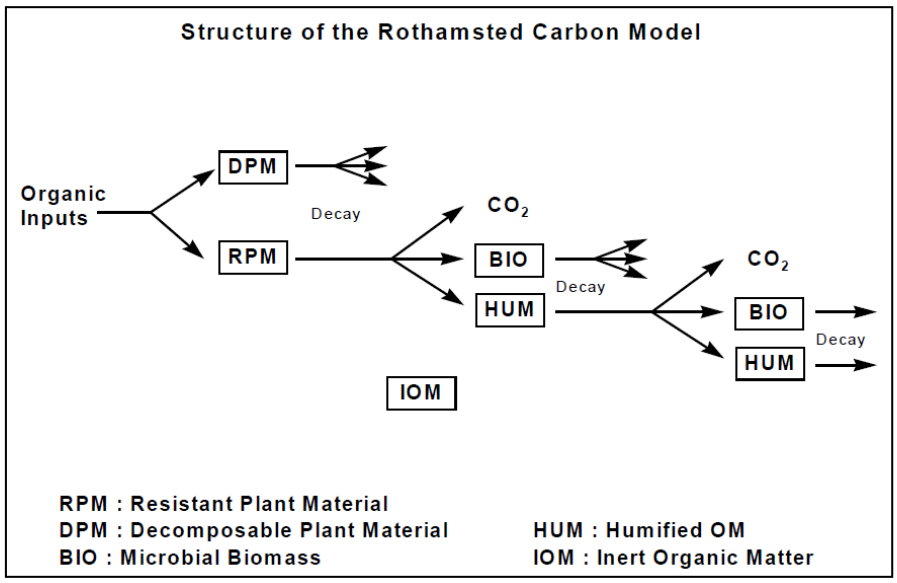

Figure 3.3: Schematic overview of the soil carbon pools in the RothC model. From Coleman and Jenkinson (1999)

The respiration R_{si} for each carbon pool (i) is calculated as the specific respiration rate κ_{si} multiplied with the carbon mass C_i, modified by a soil temperature function (F_T), a soil moisture function (F_S), and a vegetation-cover function (F_v):

$$R_{si} = \kappa_{si} C_i F_T(T_{soil}) F_s(S) F_v(v) \qquad 3\text{-}13$$

Here T_{soil}, S and v are the top soil temperature, the soil moisture content and the vegetation fractional cover, respectively. The values for κ_{si} is given in Table 3.1. The respiration modifying functions are given as[6]:

$$F_T(T_{soil}) = Q_{10_{soil}}^{\frac{T_{soil}-298.15}{10}} \quad 3\text{-}14$$

$$T_s(S) = \begin{cases} 1 - 0.8(s - s_o) & for\ s > s_o \\ 0.2 + 0.8\left(\frac{s - s_{min}}{s_o - s_{min}}\right) & for\ s_{min} < s \leq s_o \\ 0.2 & for\ s \leq s_{min} \end{cases} \quad 3\text{-}15$$

$$T_v(v) = 0.6 + 0.4(1 - v) \quad 3\text{-}16$$

Here the default value for Q_{10_soil} is 2, which is used in this study. s and s_o are the unfrozen soil moisture content of the top soil layer and the optimum soil moisture expressed as fractions of saturation. s_o is given as $s_o = 0.5(1 - s_w)$ and s_{min} as $s_{min} = 1.7s_w$ where s_w is the soil moisture at wilting point.

	DPM	RPM	BIO	HUM
Soil specific respiration rate κ_{si} (S^{-1})	$3.22 * 10^{-7}$	$9.65 * 10^{-9}$	$2.12 * 10^{-8}$	$9.65 * 10^{-10}$

Table 3.1: specific respiration rates (S^{-1}) for the four soil carbon pools in the RothC model. Modified from (Clark et al., 2011).

3.1.4 Ozone damage formulation

To simulate the effect of ozone on vegetation we follow the formulation used by Sitch et al. (2007), now standard in the JULES (Clark et al., 2011). This approach assumes a suppression of photosynthesis when the flux of ozone through stomata is above a certain critical flux. The actual simulated rate of photosynthesis (A) is then:

[6] The soil temperature function (F_T) and the soil moisture function (T_s) used here is not the original RothC formulations, but the ones implemented in JULES. For F_T the RothC formulation is also an option in JULES. The two F_T formulations do, however, give quite different respiration rates, with the original RothC formulation being about a factor 3 higher with correspondingly lower soil carbon pools. As the default JULES formulation described here gave the most realistic values compared to the average values given by the IPCC for boreal forests (2000 forest report) it was chosen over the original RothC formulation in our simulations.

$$A = A' * F \qquad 3\text{-}17$$

where A' is the rate of photosynthesis without ozone damage and F is a reduction factor due to the ozone flux, calculated as:

$$F = 1 - a * \max[F_{O3} - F_{O3crit}, 0] \qquad 3\text{-}18$$

Here F_{O3} is the ozone flux through stomata, F_{O3crit} is the critical level of ozone flux for when damage occurs, and a is a plant specific ozone sensitivity factor listed in Table 3.2, including the F_{O3crit} for the different plant types[7]. The ozone flux is originally calculated as:

$$F_{O3} = \frac{[O_3]}{r_{ab} + \frac{K_{O3}}{g_l}} \qquad 3\text{-}19$$

where $[O_3]$ is the ozone concentration, r_{ab} is the aerodynamic and boundary layer resistance, g_l is the leaf conductance, calculated in our case for CO_2 and K_{O3} is a convertion factor for leaf resistance from CO_2 to ozone. On our case we use the ozone concentration at leaf surface from WRF (see discussion on this in Chapter 4.2.2). The equation for ozone flux is then reduced to:

$$F_{O3} = \frac{[O_3] * g_l}{K_{O3}} \qquad 3\text{-}20$$

As we saw in chapter 3.1.2, the leaf conductance is itself a function of the rate of photosynthesis. As this is a linear function, it follows from Equation 3-17 that:

$$g_l = g_l' * F \qquad 3\text{-}21$$

where g_l' is the leaf conductance without ozone effect. To get a consistent calculation F, Equation 3-18, 3-20, and 3-21 must be solved analytically. This gives the following expression for the reduction factor[8]:

[7] The units of "a" has been corrected from the original table in Sitch et al. (2007) and confirmed by P. Cox (personal communication).

[8] This expression is in our case not quadratic, as Sitch et al found (2007), because the rab term is not included.

$$F = \min\left(\frac{1 + a * F_{O3crit}}{1 + \frac{a * [O_3] * g_l}{K_{O3}}}, 1\right) \quad \textit{3-22}$$

The ozone flux is then calculated as:

$$F_{O3} = \frac{[O3] * g_l' * F}{K_{o3}} \quad \textit{3-23}$$

	BT	**NT**	**C3**	**C4**	**Shrub**
$F_{O3crit}(\frac{nmol}{m^2 s})$	1.6	1.6	5.0	5.0	1.6
"High" a $\left(\frac{m^2 s}{nmol}\right)$	0.15	0.075	1.40	0.735	0.10
"Low" a $\left(\frac{m^2 s}{nmol}\right)$	0.04	0.02	0.25	0.13	0.03

Table 3.2: Ozone sensitivity parameter (a) and threshold uptake for when ozone damage occurs (F_{O3crit}) for broadleaved trees (BT), needleleaved trees (NT), C3 grass (C3), C4 grass (C4) and shrubs (shrub). Modified from Sitch et al. (2007)

3.2 Measurements

Comparing model results with observations is essential for all climate modeling. In our case, with a non-public model with a lot of new features that has not been tested by many users it is even more important. In the following we look at the observations and measurements that have been used to validate and adjust the models in this study.

3.2.1 EMEP

Ozone measurements from the EMEP[9] program was used to validate the ozone fields produced with WRF-chem. The EMEP program was established under the LRTAP convention to "regularly provide governments and subsidiary bodies under the LRTAP

[9] Co-operative Programme for Monitoring and Evaluation of the Long-range Transmission of Air Pollutants in Europe

Convention with qualified scientific information to support the development and further evaluation of the international protocols on emission reductions negotiated within the Convention" (EMEP, 2012). Its data are freely accessible online and summarized in annual reports. The ozone measurements for 2008 and 2009, including a lists of stations that provide data and their data capture, is described in Fjæraa and Hjellbrekke (2010) and Hjellbrekke et al. (2011), respectively.

3.2.2 SMEAR II

Data from the SMEAR II[10] station was used as a supplement to data from EMEP to validate WRF-Chem, and even more importantly to validate and adjust the Noah-MP model and its calculated fluxes. The SMEAR II station is located in a Scots pine forest in Hyytiälä Finland (61º51'N, 24 º17'E), and is aimed at improving our understanding of fluxes and storages in the land – atmosphere continuum and how this effects climate (Hari and Kulmala, 2005). Data from this station was used because it has been operating for a long time, and it includes many relevant quantities. This includes CO_2 flux, evapotranspiration and ozone flux between the atmosphere and the vegetation measured with the eddy covariance method (Keronen et al., 2003; Rannik et al., 2002). These data from the years 2008 and 2009 was kindly provided by the Department of Physical Sciences at the University of Helsinki.

The forest at the Hyytiälä stand, sowed in 1962, is far from any cities (nearest being Tampere about 60 km away) with the station lying in flat terrain (Hari and Kulmala, 2005). Rannik et al. (2009) reports that the dominant height of the stand around the station is about 14 m and the all sided LAI is about 6.

[10] Station for Measuring Forest Ecosystem-Atmosphere Relations

4. Results and discussion

The simulations in this study were carried out in two steps. First the WRF-chem model was run to produce meteorological fields and ozone concentration fields. Then the Noah-MP model was run offline to simulate the effect of ozone on vegetation.

4.1 Domain and simulation year

As the vegetation part of the carbon cycle takes centuries to reach a steady state, one would need to simulate many years to get an estimate of long time effects of ozone. Running the WRF-chem model for even the minimum required number of simulation points (100x100) requires, however, substantial computational resources, and simulating decades, much less centuries, would not be possible with the available resources for this study. Instead, the WRF-chem model was used to simulate one year, and the much less computationally expensive Noah-MP model was run with this forcing repeated until a steady state was reached. For this, the year 2009 was chosen as it was the most recent year with EMEP observational data available. With respect to observed summer ozone concentrations in northern Europe, this year was similar to the year before, but with low concentrations compared to the years before that (Hjellbrekke et al., 2011).

The focus in the present study was on the boreal forests in Northern Europe. Northern Europe is well covered with observations of ozone concentrations through the EMEP network. In addition, there are measurements of CO_2, ozone and water vapor fluxes from the SMEAR II station in the center of this region, measuring at a forest stand of the kind of interest here, namely evergreen needle leaf forest. The simulated domain is showed in Figure 4.1. The most northern land areas of northern Europe were not included in the domain, as it was assumed that the ozone effect here was small. Also, the northernmost part of the European continent was included in the domain so that the main areas of interest would not lie close to the boundaries. The figure also shows the vegetation types used in the simulations, taken from the USGS[11] 1/12 degree resolution database included in the WRF model. Some vegetation types not in focus in this study have been grouped together here for clarity. The same vegetation types were used in both WRF-chem and Noah-MP. The large

[11] U.S. Geological Survey

areas with evergreen needle-leaf forests in this domain are in Sweden and Finland, with smaller areas found in Norway, Russia and the Baltic countries.

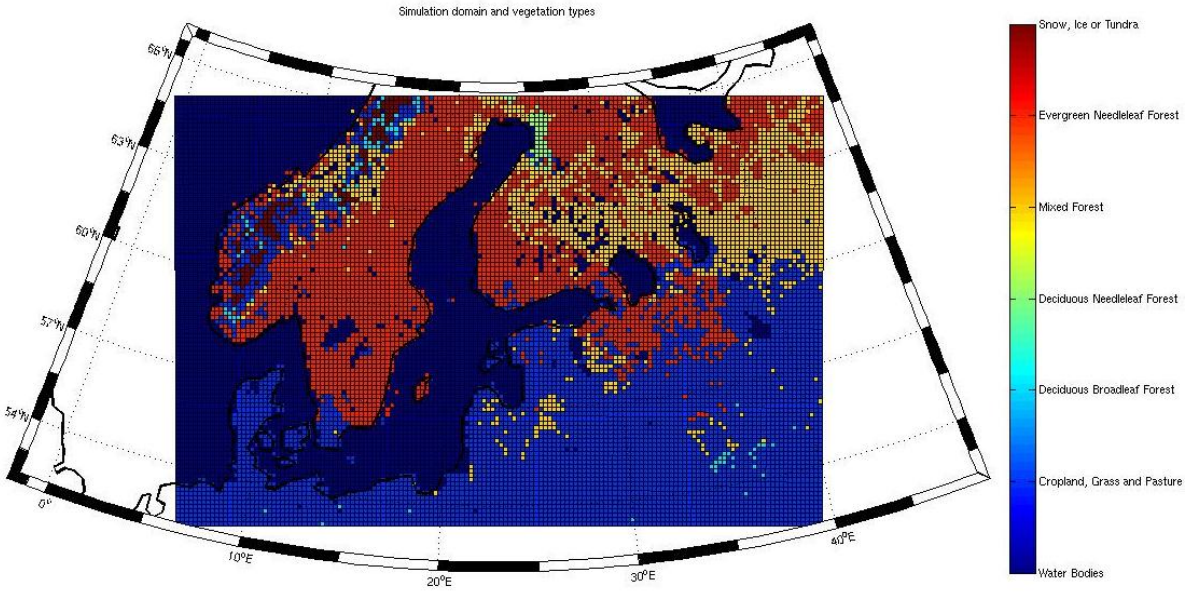

Figure 4.1: Simulation domain and vegetation types from the USGS data base. Several vegetation types have been grouped together in "Snow, Ice or Tundra" and "Cropland, Grass and Pasture".

4.2 WRF

4.2.1 Setup and tests

The WRF-chem model was first run for a test period of 10 days, from August 1st to August 10th 2008. Here different PBL schemes and surface layer (SL) schemes were tested, in addition to two different vertical resolutions and nudging. The resulting ozone concentrations were compared to the EMEP observations described in Chapter 3.2.1. Figure 4.2 shows the stations in the EMEP network in the domain. Only stations lying more than 5 grid points away from the boundaries were included. In addition, four stations in the southern part of the domain (in Germany and Poland) were excluded, as they differed a lot from the model and the other stations, and were believed to be substantially influenced by air from continental Europe outside of the domain.

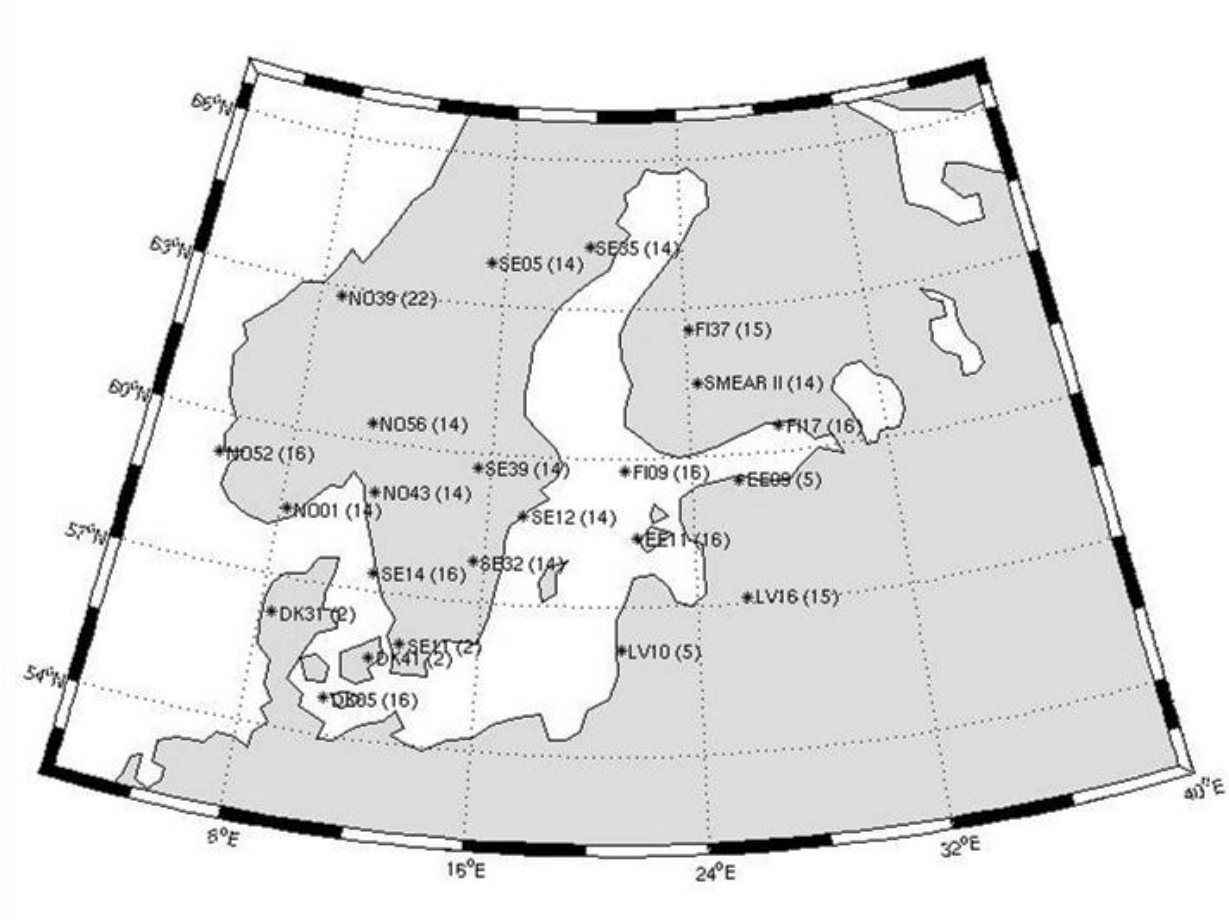

Figure 4.2: The SMEAR II station and EMEP stations located more than 5 grid boxes into the simulation domain, excluding stations in Germany and Poland, with vegetation type in the corresponding simulation grid box shown in parentheses: 2:"Dryland Cropland and Pasture", 5: "Cropland/Grassland Mosaic", 14: "Evergreen Needleleaf Forest", 15: "Mixed Forest", 16. "Water Bodies" and 22: "Mixed Tundra"

In the test simulations, the standard concentration profile was used as initial and boundary condition for the chemistry, rather than the data from the OsloCTM described in chapter 3. In addition, the SST update was turned off. The horizontal domain had 150x100 grid boxes, with a 15x15 km resolution. 35 vertical layers were used (except in the tests with the standard 28 vertical layers described below), with the lower ones taken from Hu et al. (2010), resulting in the cell center height of the lower layers lying at approximately 16, 58, 123 and 205 m. The Noah LSM land surface (LS) scheme was used, as it was considered most consistent with the offline simulations carried out with Noah-MP afterwards. Other details about the model setup can be found in the WRF-chem namelist in Appendix A, included for readers familiar with the WRF model.

The PBL, SL and LS schemes are responsible for sub-grid eddy transport and the calculations of surface fluxes of heat and moisture (Skamarock et al., 2008), and were

therefore considered most important in simulating the surface ozone concentrations. WRF has a considerable set of choices for each of these schemes. One cannot, however, use any combination of these, as some of the PBL schemes require the use of specific SL schemes, and only a few setups have been tested and found to work well together with WRF-chem (Peckham et al., 2011). Based on the suggestions in the WRF-chem user's guide, the following three combinations were tested: The YSU[12] PBL scheme with the required MM5 similarity surface layer scheme, the MYJ2.5[13] PBL scheme with the required Eta similarity surface layer scheme, and the MYNN[14] scheme (both PBL and SL). More details about the different schemes, including references, can be found in the ARW modeling system user's guide (Wang et al., 2012) and the NCAR technical note (Skamarock et al., 2008).

The results of the tests with the different schemes are summarized in Table 4.1. Shown in the table are the average bias, and root mean square error (RMSE), shown for both the whole simulation and for daytime[15] only, as well as the mean correlation between daily maximum ozone concentrations observed and simulated. All the statistics are averaged over all the 22 EMEP stations.

Schemes	RMSE	RMSE_day	BIAS	BIAS_day	Corr max day:
MYJ	8.3978	7.6100	1.2563	0.65691	0.55464
YSU	8.7372	7.8342	3.3185	2.0855	0.56255
MYNN	8.4906	7.8588	2.573	2.1975	0.55893

Table 4.1: Root mean square error (RMSE), root mean square error for daylight hours (RMSE_day), bias (BIAS), bias for daylight hours (BIAS_day) and correlation between simulated and observed daily maximum concentration (Corr max day) for three different PBL schemes from August 1-10, 2008. All values are averaged over the 22 EMEP stations in the domain, and all values, except for the correlations, are given in ppb.

As can be seen in Table 4.1, the three different schemes perform almost equally well. A difference of 1 ppb is relatively small when simulating ozone concentrations. Also, the daily maximum concentration correlations are approximately the same for the three schemes. Still,

[12] Yonsei University

[13] Mellor-Yamada-Janjic

[14] Mellor-Yamada Nakanishi and Niino Level 2.5

[15] Here the daytime was taken to be all the hours with short wave radiation greater than zero, excluding the first and the last hour.

the highest correlation is found using the YSU scheme, and the smallest bias using the MYJ scheme. A zero bias is, however, not necessarily better, as these results compare cell average concentrations in the WRF-chem model with surface observations from the EMEP network. As the dry deposition takes place at the surface, a smaller value could be expected here. A difference of 1-2 ppb from the surface to 16 m is similar to that observed at SMEAR II during the summer (Keronen et al., 2003). This can also to some extent explain the higher RMSE for YSU and MYNN.

These test results justify the use of any one of the three schemes. The YSU scheme was then chosen for the simulations in this study, as it gave the highest correlation with observed daily maximum values, and a bias within a range that was considered reasonable. Figure 4.3 shows the whole time series of the YSU test at selected stations in the main area of interest. There are considerable differences in model performance between the different locations, with the bias ranging from 1.9 to 8.9 ppb in these stations. Also, substantial temporal differences in the model performance can be seen. The model has problems reproducing the night time drop in ozone concentrations that is observed at many stations, especially. This may to some extent be attributed to the fact that the values are given for two different heights. During the night, a shallow, stable surface layer with little exchange of air with the rest of the PBL is common. As some dry deposition also takes place during night, this can result in very low concentrations of ozone close to the ground. This became even clearer when studying a costal station more closely. Figure 4.4 shows the simulated and observed ozone concentrations at the Finnish station FI17, together with the simulated winds. Here the drop in night time concentrations is not observed when the wind comes in from the ocean (south) where very little dry deposition is taking place, but only when there is little wind or wind from the surrounding land areas. Also presented in Figure 4.4 is the amount of short wave radiation, with an arbitrary scaling so that day and night can be clearly distinguished.

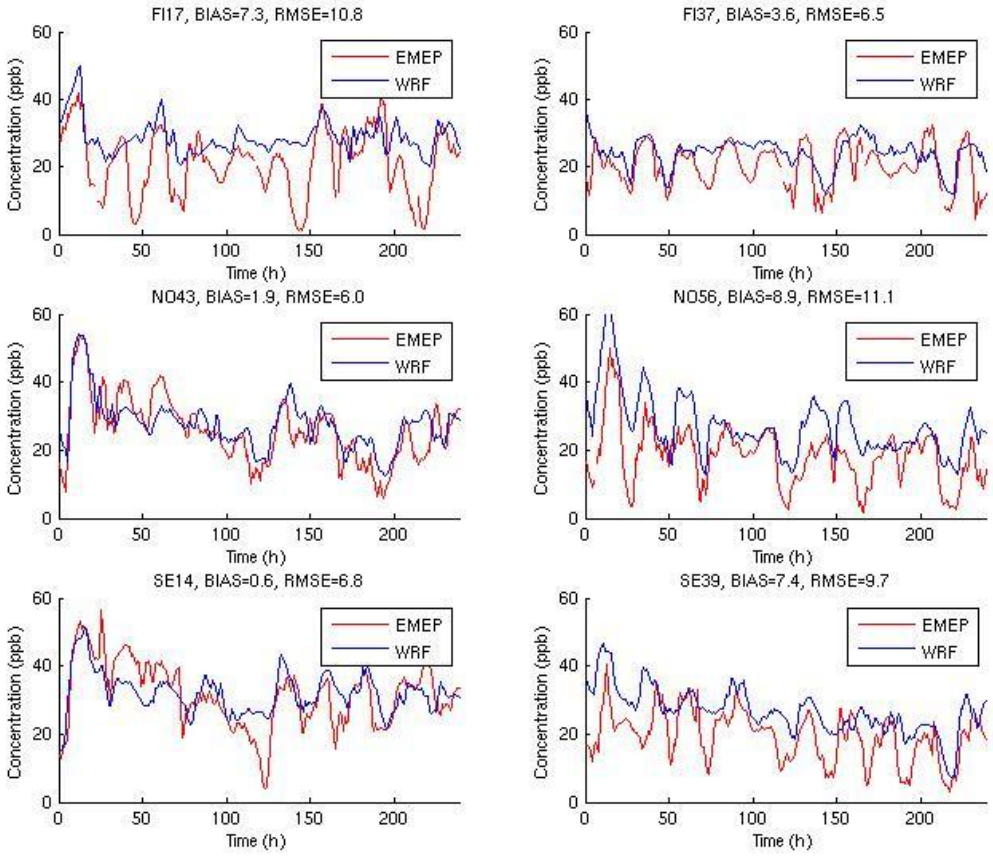

Figure 4.3: Simulated (lowest model layer; YSU scheme) and observed (2 m) ozone concentrations for selected EMEP stations from August 1-10, 2008, including station code, bias (ppb) and RMSE (ppb).

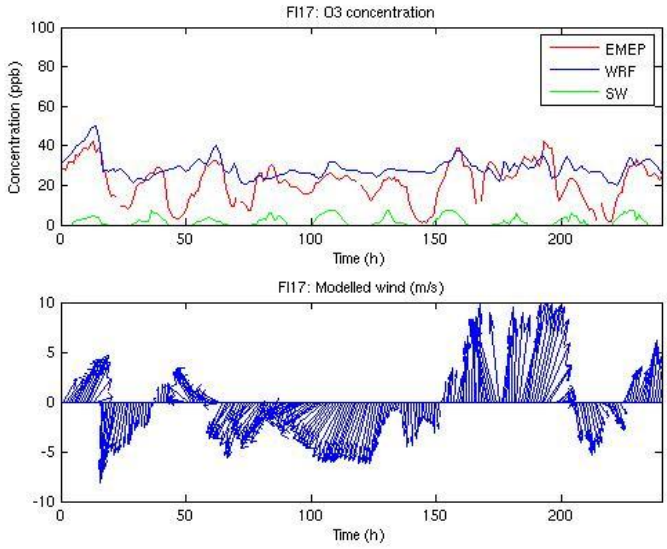

Figure 4.4: As in Figure 4.3 for the "FI17" station, but including also downward shortwave radiation with arbitrary unit to show the diurnal cycle (top) and simulated 10 m wind at the "FI17" station for the same time period (bottom).

Additional tests where performed with the chosen YSU scheme, with nudging and the original 28 vertical layer resolution. The results of these tests showed that increased resolution close to the ground had a positive impact on the performance with the YSU scheme, whereas nudging seemed to have a negative impact, both however relatively small.

4.2.2 Results

After the test simulations the WRF-chem model was run for the entire year of 2009. In these simulations the initial and boundary conditions from OsloCTM were used for the chemistry and SST update was on, including calculations of SST-skin. The rest of the setup options were the same as in the test simulations, and are shown in the namelist in Appendix A.

Figure 4.5 shows the resulting simulated daily mean ozone concentration at selected stations, and the corresponding EMEP observations. There is, again, considerable variation between the stations. Still, some tendencies are similar in all or most of these stations. First of all, the model seems to reproduce the observed concentrations quite well during winter, both in the beginning and end of the simulation year. For the most part, it captures both the average value and daily variations in the observed concentrations in this part of the year quite well. During spring, the model has, however, a tendency to underestimate the concentrations, although this varies between the stations. Sometime during summer, this tendency shifts, and a clear overestimation of concentrations is seen for all the stations. This yearly pattern becomes even clearer when looking at the monthly statistics in Table 4.2, which also show the biases when adjusting the concentrations to the reference height in the model (2 m) and to the leaf surface, with a method described under the next heading. These data, which again are averaged over all the 22 stations, show that there is indeed a consistent result for the whole domain that the model simulates too low spring concentrations and too high late summer and fall concentrations. They also reveal, however, that these monthly biases cancel each other out almost entirely, so that the yearly average bias, especially for the reference height, is practically zero.

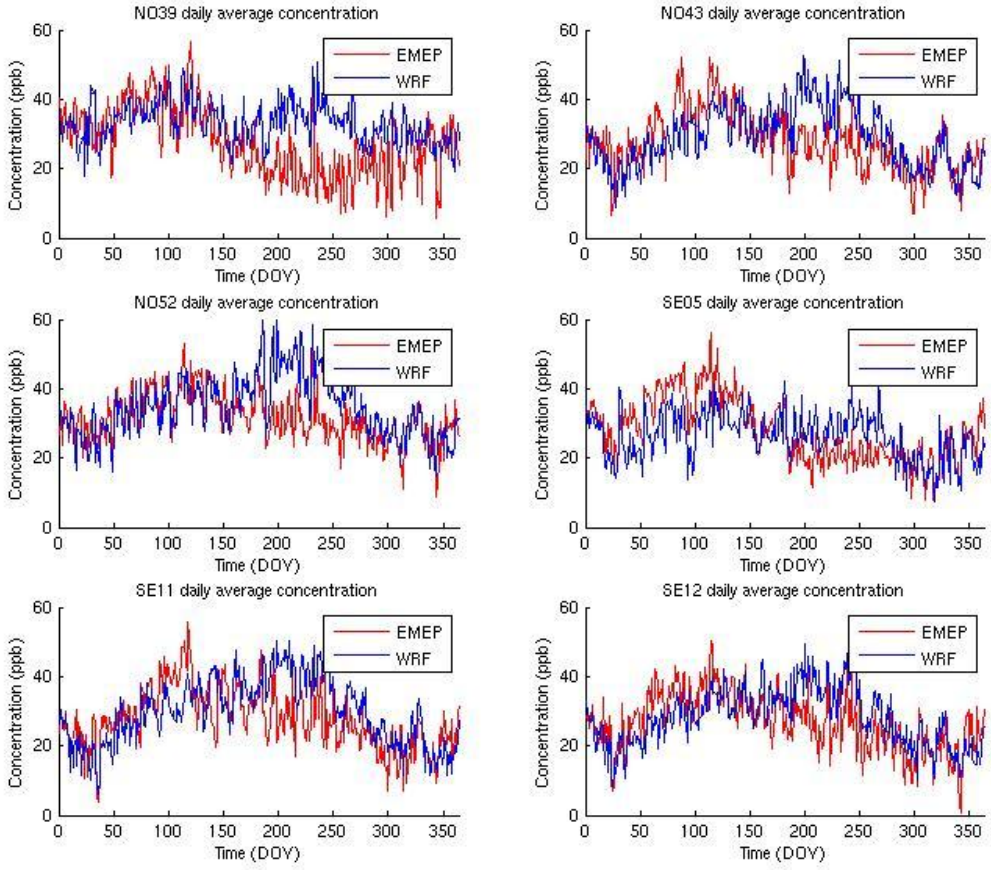

Figure 4.5: As in Figure 4.3, for a new set of selected stations and for the whole year of 2009.

	RMSE	RMSE_day	BIAS_cell	BIAS_ref	BIAS_leaf	Corr max day:
Jan09:	6,87	6,80	-2,20	-2,77	-3,98	0,67
Feb09:	8,33	8,41	-4,04	-4,69	-6,02	0,62
Mar09:	9,62	9,82	-5,96	-6,88	-9,02	0,56
Apr09:	13,00	12,48	-6,84	-8,82	-12,68	0,63
May09:	9,72	8,89	-2,32	-4,43	-8,51	0,43
Jun09:	8,20	7,41	2,02	-0,06	-4,02	0,44
Jul09:	12,33	11,44	10,34	7,83	3,12	0,51
Aug09:	11,78	10,88	10,48	8,11	3,83	0,55
Sep09:	9,69	8,37	8,15	6,42	3,36	0,63
Oct09:	6,78	6,10	3,74	2,50	0,47	0,63
Nov09:	6,11	5,87	1,76	1,02	-0,54	0,65
Dec09:	7,79	7,72	-2,04	-2,64	-3,73	0,53
MEAN:	9,18	8,68	1,09	-0,37	-3,14	0,57

Table 4.2: As in Table 4.1, but including also bias for reference height (BIAS_ref) and leaf surface (BIAS_leaf) and calculated for each month of 2009, including the average over all the months.

Ozone concentrations at leaf surface and reference height

With the resistances in the Wesely scheme (see Chapter 2.4) it is possible to adjust the concentration of ozone at the lowest model cell centre, to other levels in the pathway from the atmosphere to the surface. This can be useful when comparing with observations at other heights than that of the cell centre. As the Noah-MP model does not calculate all the resistances in this scheme, this was necessary to calculate the relevant concentrations for calculating ozone damage in this model, namely the leaf surface concentration.

This method exploits the fact that the same flux must go through all the resistances: Ra, Rb, and Rc (see e.g. Gerosa et al., 2005). This gives:

$$F = \frac{C_{cell}}{R_a + R_b + R_c} = \frac{C_{leaf}}{R_c} \qquad 4\text{-}1$$

Here C_{cell} is the ozone concentration at cell centre, and C_{leaf} is the concentration between the sub-laminar layer and the surface (leaf, cuticle or ground). C_{leaf} is then given as:

$$C_{leaf} = C_{cell} \frac{R_c}{R_a + R_b + R_c} \qquad 4\text{-}2$$

This concentration can then be used with the stomata resistance in Noah-MP to calculate the stomata flux. There is, however, an inconsistency in this method as the concentration calculated here does not take into account the flux from the Noah-MP model. If the stomatal resistances from the two models are very different, this could be important for the calculated stomatal flux. A too high stomatal resistance (low deposition) in the WRF-chem model would for instance lead to a too high concentration, which combined with a too low resistance in the Noah-MP model would give too high estimates of stomatal uptake.

Finding the concentration at the reference height in the WRF-chem model is achieved in much the same way. This reference height is not a part of the original Wesely scheme, but is used in the WRF-chem model, where the resistances Ra, Rb, and Rc are calculated for this height and the resulting deposition velocity (the inverse of the total resistance) is adjusted to give the deposition velocity at the cell centre height based on the height difference and the stability of the air. As above, if fluxes are the same through both heights the relationship between the two concentrations is given as follows:

$$F = \frac{C_{cell}}{(R_a + R_b + R_c)_{cell}} = \frac{C_{ref}}{(R_a + R_b + R_c)_{ref}} \qquad 4\text{-}3$$

Here C_{ref} is the concentration at reference height. Solving for C_{ref} and using the relationship between resistances and deposition velocity (Equation 2-2) gives:

$$C_{ref} = C_{cell}\frac{(R_a + R_b + R_c)_{ref}}{(R_a + R_b + R_c)_{cell}} = C_{cell}\frac{Vd_{cell}}{Vd_{ref}} \qquad 4\text{-}4$$

This is also shown and discussed by Rydsaa (2010) based on WRF-chem equations. Although not intended to give the actual concentration at 2 m height, as it does not account for whether this is above or below the canopy, C_{ref} is believed to be more representative for the concentration at the surface than the one given for the cell centre.

The methods described above require data for Ra, Rb, and Rc at both cell centre height and the reference height, in addition to the cell centre height concentration (C_{cell}). The three resistances were, however, only stored for the reference height, and not for the cell centre height. Adjustment of deposition velocity from reference height to the cell centre height in WRF-chem, is essentially done by adding an extra resistance to those at the reference height, which we will call Rx. In addition to the resistances at reference height, WRF-chem also calculates an aerodynamic resistance (Ra) at cell centre height, which is not used in the calculations of ozone deposition, but was also stored in our simulations. To find an approximate value for the total resistance at the cell centre height, Rb and Rc were taken to be the same for the reference height as well as the cell centre height, as these are properties of the surface. The total resistance for the cell centre height was then taken to be Ra at cell centre height plus Rb and Rc at reference height (instead of Ra, Rb and Rc at reference height plus the adjustment resistance Rx). When testing this approximation for two three-day-periods with all relevant data as output, it was found that it differed by only a few per cent from the actual total resistance at cell centre height.

4.3 Noah-MP

4.3.1 Setup and tests

As the Noah-MP model does not initially include ozone effects, the model was tested and adjusted without this effect. The tests were conducted for a single column[16], simulating the grid box from WRF-chem where the SMEAR II station in located. The focus in these tests was on achieving a good agreement with observed NEE and a reasonable LAI for an evergreen needle-leaf forest. How the carbon pools developed over time was also considered, although no observations were available for comparison. In addition, the simulated and observed evapotranspirations were compared, although this variable was not considered to be as important as NEE for the carbon calculations studied here. Also, the data capture from SMEAR II station was not as good for this variable as for the NEE. As will be clear in the next section, these tests revealed a need for rather substantial changes before the model could produce meaningful results for our purposes. In the following, the initial model performance and the main steps in subsequent correction and adjustment of the model will be presented. One should have in mind that the version of Noah-MP used here was not a public version, and that the carbon calculations used in this study are only used when the DV option is used. The model performance without this option could have a very different performance.

Initial model preformance

The model was initially run for 25 years with the same one-year forcing from WRF. The forcing data needed to run the model are solar radiation, downward longwave radiation, precipitation, air temperature, wind speed (E-W and N-S directions separately), surface pressure and specific humidity. Noah normally uses data for these variables at 2 m height. WRF, on the other hand, produces winds at 10 m height. Simple tests assuming WRF 10 m winds to represent 2 m, 10 m and 16 m showed only minor differences. This inconsistency was therefore accepted.

[16] The Noah model is run for each column independently in any case, so the results would not have been different for this grid point if the model had been run for a larger domain.

Figure 4.6 shows the simulated and observed NEE for the 15th simulation year, with negative values representing a flux to the surface (uptake). The 15th simulation year was chosen here because at this stage the whole model, apart from the long lived carbon pools (wood and soil), has reached a steady state. Leaf, stem and root carbon pools, and other model variables like soil moisture, were stabilized during the first couple of years. Also, since all the other carbon pools other than leaves had no influence on the rest of the model, the only difference between NEE for the different years after this comes from changes in carbon release back to the atmosphere through respiration. To get truly comparable data for NEE one would, however, need some way of initializing the carbon pools as the magnitude of NEE is dependent on the magnitude of the respiration, and therefore the carbon pools. Such data was unfortunately not available. Still, the uptake of carbon is not affected by other carbon pools than the leaves, so the shape of the NEE curve is largely comparable to the observed values, even when the respiration terms are uncertain.

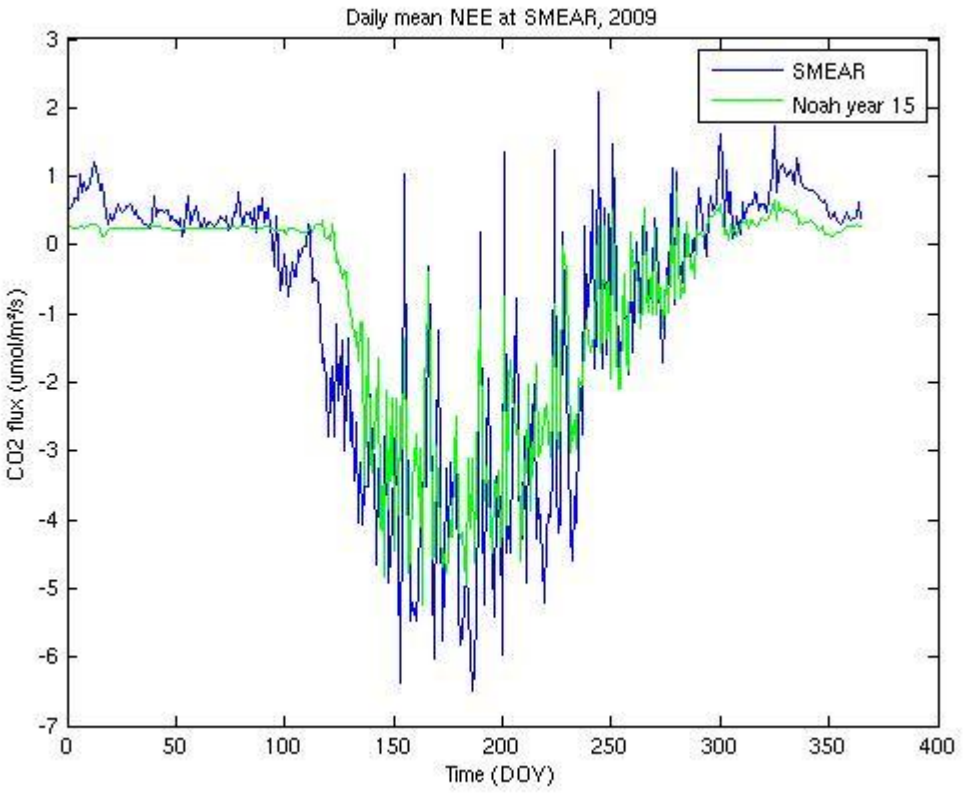

Figure 4.6: Simulated (year 15) and observed daily mean NEE at the SMEAR II station for the whole year of 2009, using the initial Noah-MP model.

With this in mind, the figure indicates a good general model performance when it comes to reproducing NEE. It captures the yearly cycle and the days with very low carbon uptake

during summer. There are some clear differences, however. First of all, Noah-MP seems to start the growing season too late. Secondly, the model has too little release of carbon (respiration) during winter, and very little variation during this part of the year. Much of the reason for this can be found when looking at the LAI in Figure 4.7. Here the LAI goes to a minimum value close to zero during winter, which is clearly wrong for an evergreen forest. As the carbon uptake is directly linked to the amount of leaves, this could explain the late spring in the model. Instead of having a large amount of needles available to carry out photosynthesis when sunlight and temperature allow it, the model must gradually build up these needles in the same fashion as for deciduous trees. The lack of needles during winter could also explain the low respiration activity, as leaves are responsible for much of the carbon release through respiration.

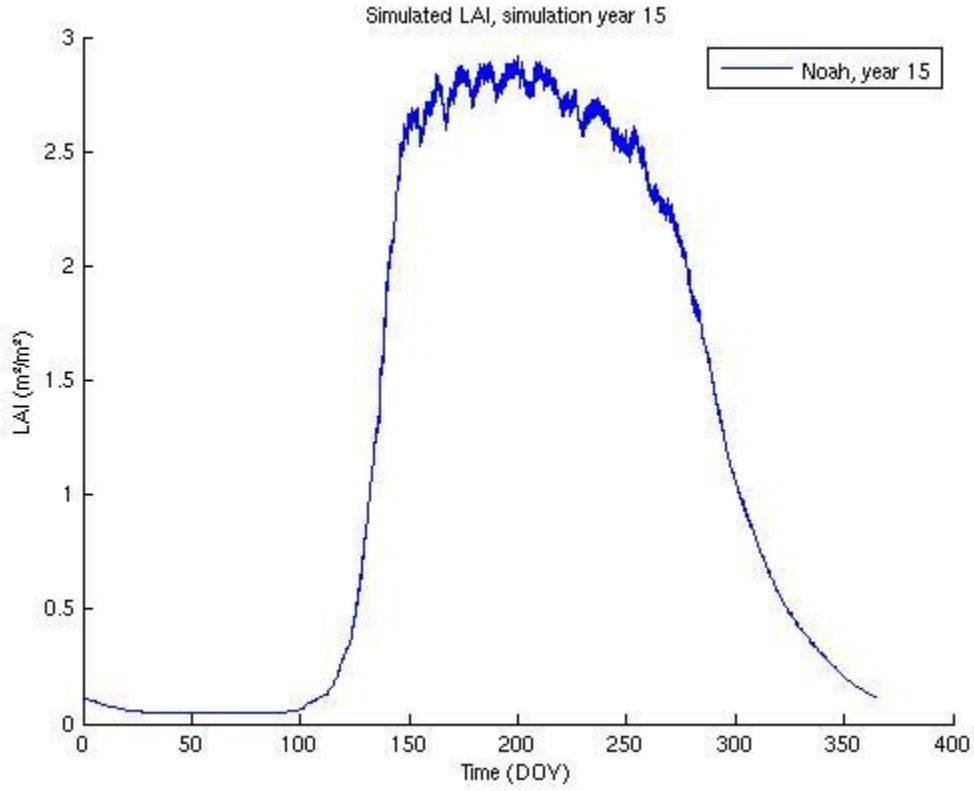

Figure 4.7: Simulated LAI at the SMEAR II station for the 15th simulation year, using the initial Noah-MP model.

Figure 4.8 shows the simulated and observed evapotranspiration, which in the model is the sum of the evaporation of intercepted water, soil surface evaporation, and transpiration. As noted earlier, the data capture from the SMEAR II station is not as good for this variable as for NEE. This can also be seen in the figure where the daily mean values are missing for

some days for the “SMEAR” curve. Incomplete observational data could also lead to biased daily mean values for some days, as the mean here is only taken from the available data without taking into account for what part of the day data is missing. Still, a generally good agreement between the model and observations can be seen. In the first part of the year (winter), the model does, however, show too little activity. Also, the onset of spring is not captured correctly, although here it seems as if the model simulates the spring too early rather than too late.

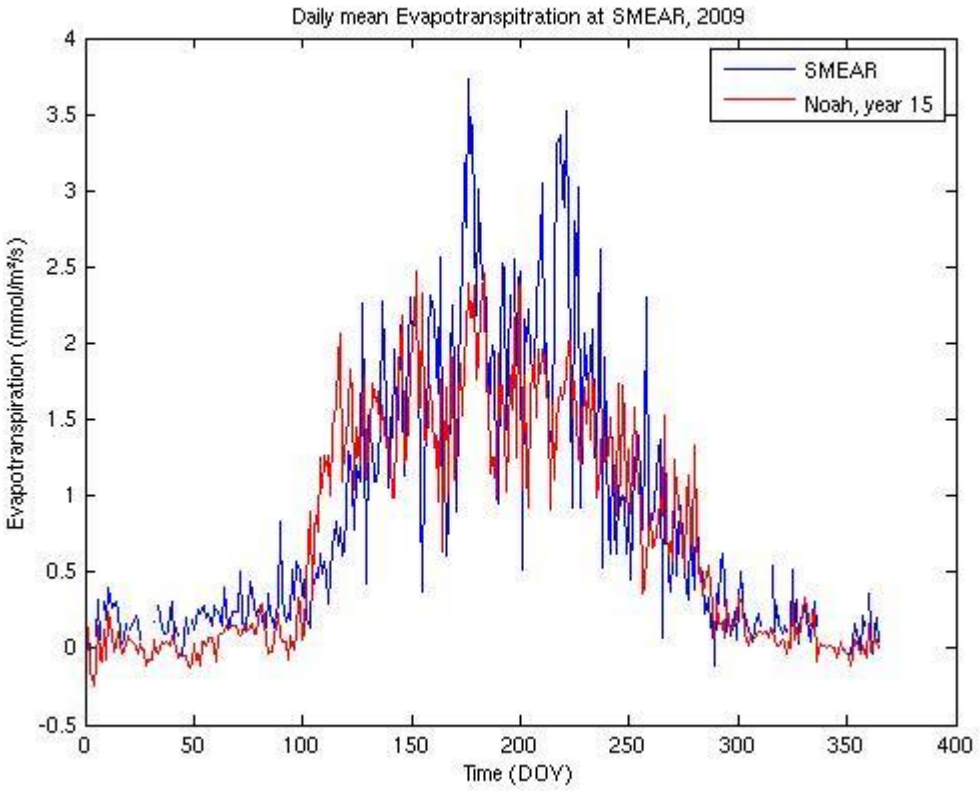

Figure 4.8: Simulated (year 15) and observed daily mean evapotranspiration at the SMEAR II station for the whole year of 2009, using the initial Noah-MP model.

Figure 4.9 shows the development of the different carbon pools over the 25 years of simulation. Here, again, the leaf carbon mass drops to a minimum value during winter. The same is true of the stem carbon mass. Also, as indicated before, only the wood and soil carbon pools need more than a few years to stabilize. For wood, this seems realistic as a few years is a relatively short time in a tree’s life cycle. For the fast soil carbon pool this does not, however, seem to be in line with its lifetime, as outlined by Dickinson et al. (1998), who gave this carbon pool a respiration rate under favorable conditions of 5 x 10^{-8} s^-1, which gives it a lifetime of less than a year. For the slow carbon pool on the other hand, there are,

as described above, no loss mechanisms and this pool will therefore never reach a steady state.

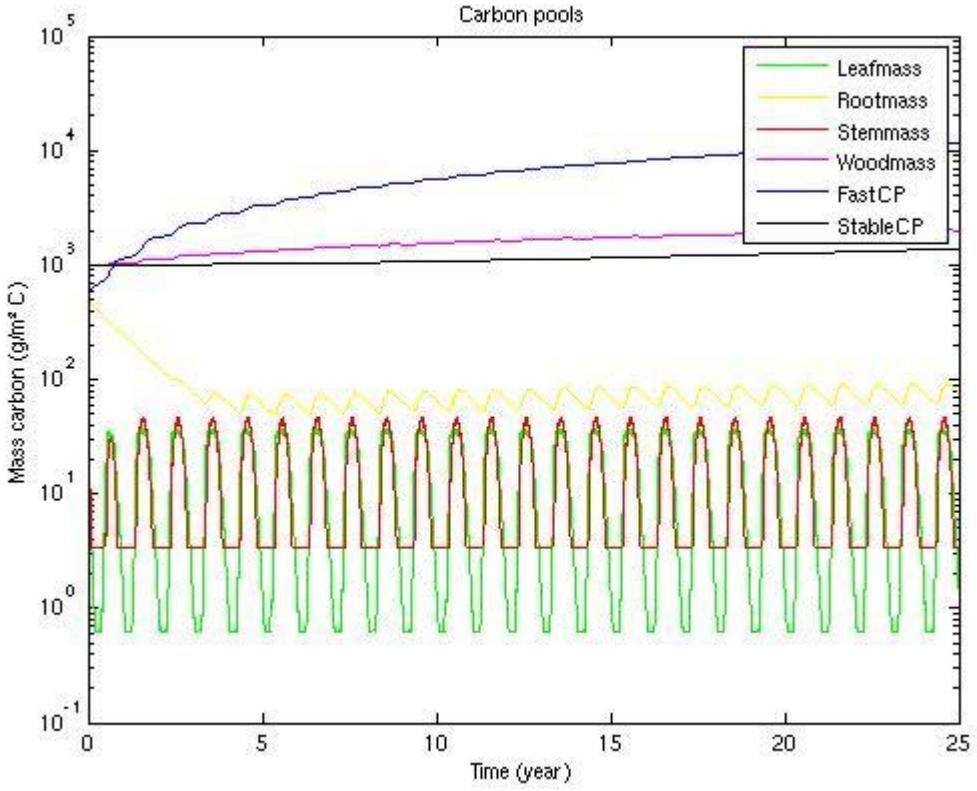

Figure 4.9: Simulated carbon mass in the different carbon pools at the SMEAR II station for a 25 years simulation, using the initial Noah-MP model.

Errors and bugs

Together the results from the initial model tests revealed that there was a need to take a closer look at the carbon calculations in Noah-MP and its different parameters and functions. In particular, when comparing the daily net carbon uptake and the change in carbon pools, it was evident that these two did not match. More carbon was added to the vegetation than was taken up through photosynthesis, as shown in Figure 4.10. This error was fairly pronounced, and could be quite important when studying the long term carbon budgets.

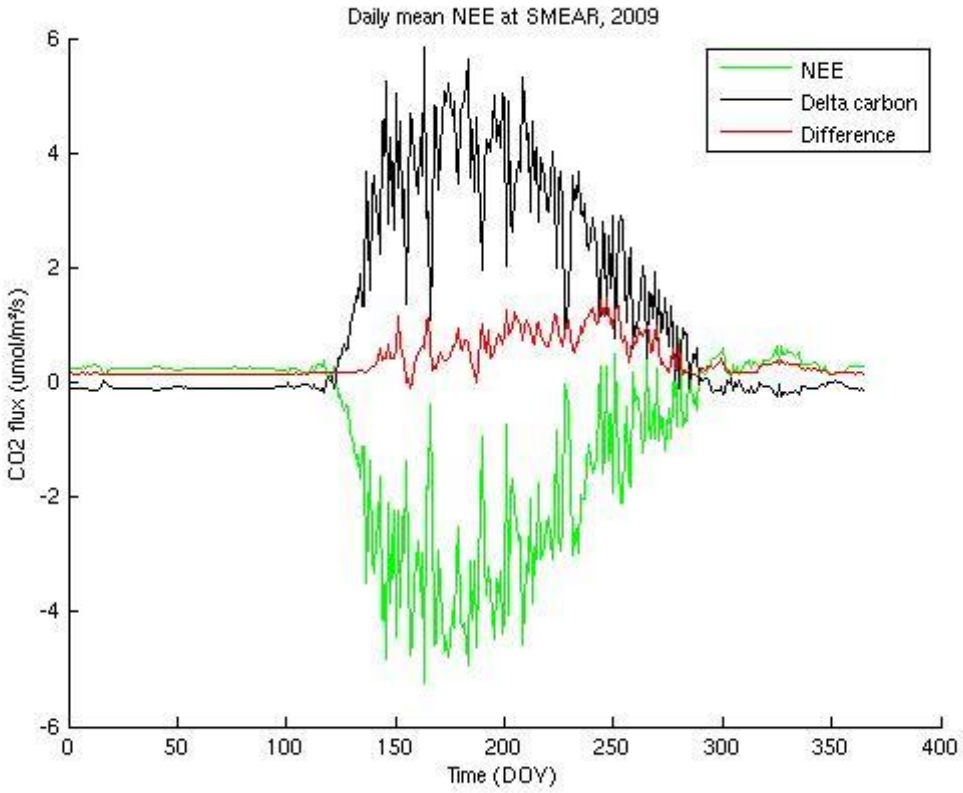

Figure 4.10: Simulated daily mean NEE and change in total carbon in all carbon pools for the 15th simulation year with the initial Noah-MP model. "Difference" shows the difference between the two for each day, which represents an inconsistency in the model, as NEE includes all carbon fluxes.

Looking into the code revealed quite a few clear bugs, most of which were related to the stem carbon pool and it's fluxes that were not originally part of Dickinson's DV model. This carbon pool and its fluxes were typically missing in many equations involving all or some of the carbon pools. For instance, the carbon lost from stems through drought and cold stress was not added to the soil carbon, and its respiration terms were not included in the calculation of NEE. Correcting these errors removed some of the difference between carbon uptake and accumulation. The major part of the difference was, however, due to a less obvious error. When calculating the net carbon flux through photosynthesis and respiration for leaves and stem, the initial model had a restriction that this should not be negative. This restriction was, however, not linked to the calculation of carbon fluxes, which meant that whenever respiration for these plant parts was greater than the carbon assimilated to these parts through photosynthesis (as is the case every night) a net carbon release was simulated without reducing the carbon pools. This restriction had an important function in keeping the leaf and stem pools from reaching negative values during winter (although this really should

not be a problem when simulating evergreen forests). It was, however, clearly wrong whenever these pools contained enough carbon to simulate respiration. To deal with this, another restriction was removed, which kept the loss term from cold and drought stresses from reaching negative values (making them production terms instead). As this was the last term to be calculated, it was restricted by the amount of carbon left in the pools. Removing the first restriction meant that there could actually be less carbon than the minimum value, and in this case the last loss term would compensate for this instead of further removing carbon. As it is linked to the adding of carbon to the soil, this ultimately meant that this carbon was taken from the fast soil carbon pool. Physically, when considering the different processes independently, this makes no sense. Numerically, this was, however, taken to be the best solution as it both ensured consistent calculation of carbon fluxes and pools[17], and it prevented the leaf and stem pools from dropping below their minimum values.

Adjustments of parameters

Although the corrections described above were important to gain a more reliable model, it did not solve the main issues from the initial test results; too little winter activity and late onset of spring, too low LAI during winter, and the fast carbon pool that that seemed to have too long a lifetime. In order to do something with these issues, the different parameters and equations would have to be changed.

A set of different parameter adjustments was tested in order to deal with these issues. This included reducing the leaf carbon loss rates both collectively and individually, changing the relative portioning of carbon to the different pools, and changing the equation for fast soil carbon respiration to be more in line with the formulation outlined in Dickinson et al. (1998). The latter change gave the fast soil carbon shorter lifetimes and had scientific basis, but was made obsolete by the implementation of the RothC soil carbon model. For the NEE and LAI calculations, two key parameters had very unrealistic values in the model. First it was the turnover rate for needle leaves in the model that was set to 0.5×10^{-6} s^-1 for evergreen needle leaf forests, about the same as for deciduous broadleaf forests. This gives a lifetime for leaf carbon of about 23 days, whereas in reality that value is more in the order of 3 years,

[17] A full consistency in calculation of carbon pools and fluxes was still not reached, but the difference was now so small that it was not given more consideration.

although it varies for different species and regions (personal communication: Daniel Rasse). Secondly the specific leaf area (SLA) that relates LAI to the leaf carbon mass was unrealistic. It was initially 80 m^2/kg, making the model reach a LAI of 3 with only about 27 g/m^2 of leaf carbon. In reality about one order of magnitude more carbon is needed (personal communication: Daniel Rasse)[18]. The leaf turnover rate for evergreen forests, and the SLA, were therefore multiplied with the factors 0.02 and 0.1 respectively.

Although these two changes made improvements in the NEE and LAI calculations, the simulated LAI still reached unrealistically low values during winter. This was due to the effect of cold and drought stresses, which at after the changes above where the dominating loss mechanisms for leaf carbon. Tests without these mechanisms gave much more realistic LAI values. These mechanisms were later included again with a changed minimum temperature from 278 K to 228 K, as described in section 3.1.2., giving almost identical results to those without cold and drought stresses. Finally, the stem carbon part of the model was removed by allocating the whole leaf portion of the assimilated carbon to the leaf pool (see section 3.1.2).

The resulting LAI is shown in Figure 4.11, with values that vary from about 2.5 during winter to 3.5 during summer, in good agreement with the vegetation being evergreen, and with the reported all-sided LAI of 6 by Rannik et al. (2009). Figure 4.12 shows the simulated NEE for simulation year 15. Here we also see a somewhat better agreement with observations, especially in the first 50 days, where the initial model showed almost no activity. The onset of spring is, however, still not very well captured, and is now too early instead of too late. Figure 4.13 gives a more detailed account of the model performance in reproducing NEE, giving the hourly NEE for the first week of April, June, and August. Here again the overestimation of carbon uptake in clear from the first week of April, but a very good model performance in June and August, both when it comes to the magnitude, capturing day and night variations, and capturing variations from day to day.

[18]Because of the way carbon is allocated to leaves as a function of LAI it is more meaningful to talk about how much carbon there is in the leaves for a given LAI, although the model actually calculates the amount of carbon, and finds the LAI based on that.

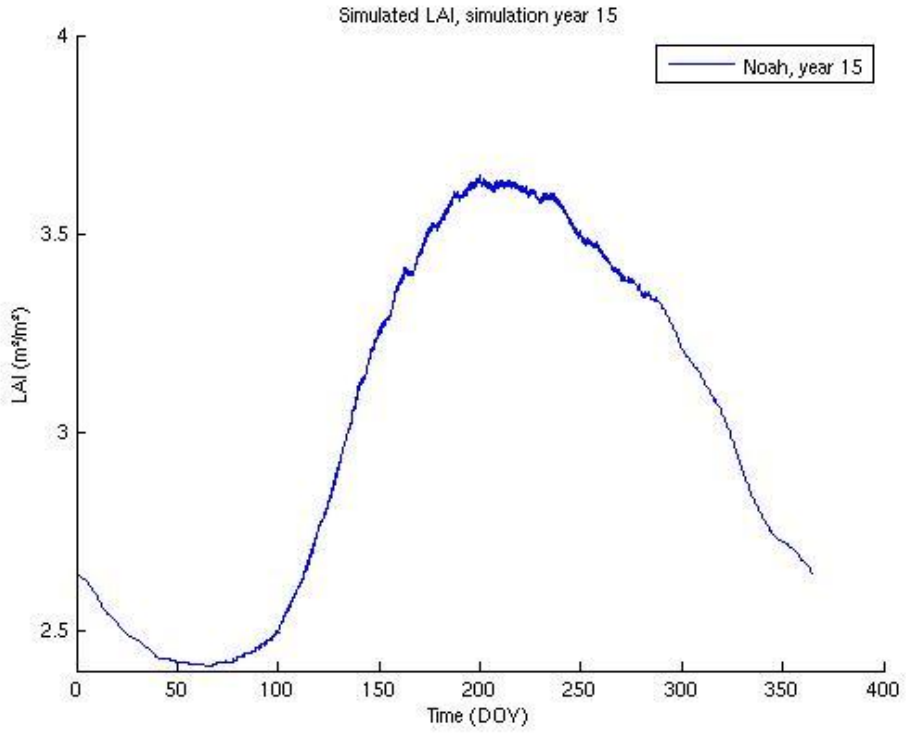

Figure 4.11: As in Figure 4.7 but after having fixed the bugs and completed all parameter adjustments.

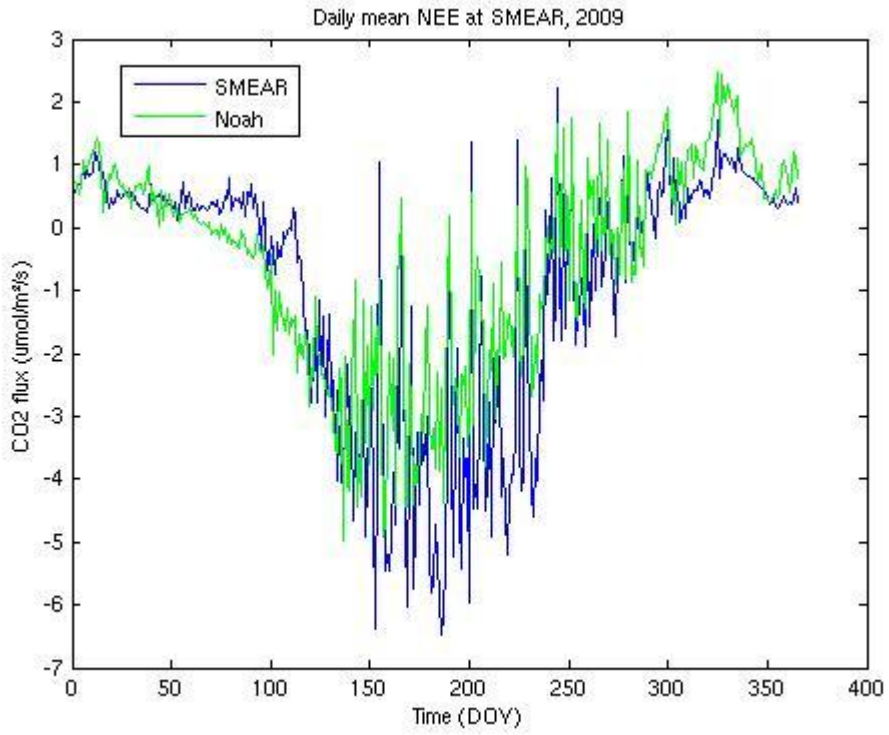

Figure 4.12: As in Figure 4.6 but after having fixed the bug and completed all parameter adjustments.

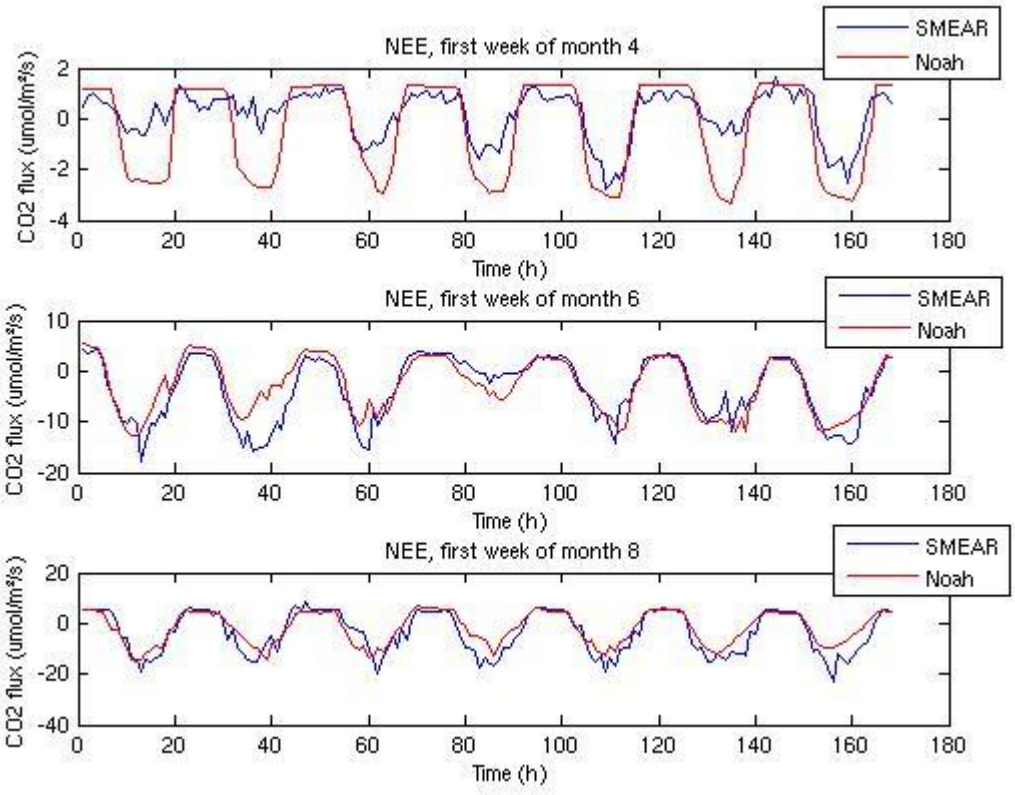

Figure 4.13: Simulated (year 15) and observed hourly mean NEE at the SMEAR II station for the first week of months 4, 6, and 8 of year 2009, using the Noah-MP model, after having fixed the bugs and completed all parameter adjustments.

New soil carbon scheme

As the main portion of carbon in boreal ecosystems is in the soil (IPCC, 2000b), it is not possible to get an estimate of the full terrestrial carbon budget without a proper simulation of soil carbon. This was not the case in the original soil carbon formulation in Noah-MP, as it included no sinks for the slow soil carbon pool and therefore it would grow infinitely. This could have been dealt with by introducing a single respiration term for the slow soil carbon pool, with an appropriate respiration time. However, as the RothC model (described in Chapter 3.1.3) is already in use for climate simulations and was described in available literature with enough details to be implemented without any prior knowledge or crude assumptions, it was considered a better alternative.

The implementation of the RothC soil carbon scheme did not affect other Noah-MP results than the NEE (through changed soil respiration) and the soil carbon pools in themselves. Only the carbon pool budgets from the simulation with this new scheme are therefore

presented here. Also, as the change in NEE with this implementation is mainly due to new initialization, only the simulated total carbon is presented. This is shown in Figure 4.14, which shows the amount of carbon in the different pools for 3 years at steady state with the new soil carbon scheme. To make it comparable to Figure 4.9, the four soil carbon pools have been grouped in two, so that "FastCP" is now the sum of DPM and RPM and "SlowCP" is the sum of BIO and HUM.

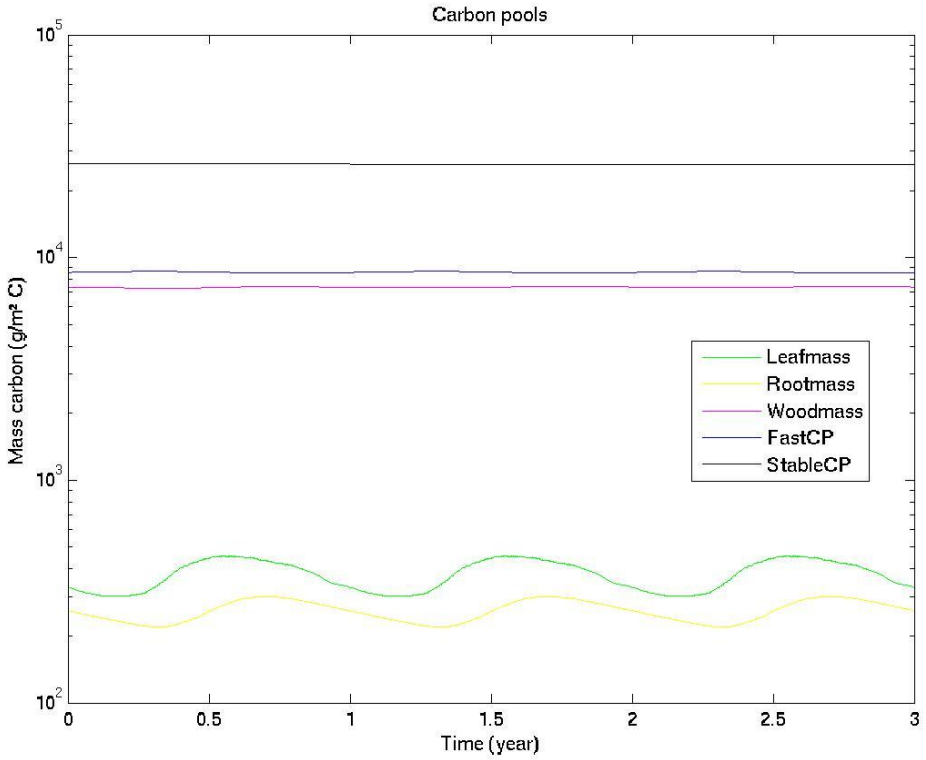

Figure 4.14: Same as in Figure 4.9, but with having fixed the bugs and completed the parameter adjustments, without stem carbon pool and with the RothC model for soil carbon. "FastCP" is the sum of DPM and RPM and "StableCP" is the sum of BIO and HUM for 3 years after using an equilibrium accelerator.

Spin-up

By considering only the maximum respiration rates for the soil carbon pools in Table 3.1 we find that the lifetime of the slowest pool (HUM) is at least 50 years. With the actual respiration rate being considerably less, we understand that a simulation time of several hundred years to reach steady state would be needed. Without data to initialize the carbon pools, the steady state values are the most meaningful values to compare for simulations

with and without ozone effects. To reduce simulation time, an equilibrium accelerator (EA) was therefore developed. This was done based on the mass balance equation:

$$\frac{\partial C}{\partial t} = P - l * C \qquad 4\text{-}5$$

where C is the mass of a pool (or concentration in atmospheric chemistry), P is the production rate and l is the loss rate constant, so that $l * C$ gives the loss rate. At equilibrium the left hand side is zero and C can be found as:

$$C = \frac{P}{l}. \qquad 4\text{-}6$$

This can be applied to our carbon pools as well, with a few necessary assumptions. The loss rate constants for the carbon pools vary with different conditions and can therefore only be found as constants when averaging over a year, and only when the same forcing is used every year. The resulting mass found with this equation is therefore only meaningful for the pools that have lifetimes that are long compared to a year. Based on the information from Table 3.1 and from Figure 4.9 we can see that these are the wood (W), RPM (R), BIO (B) and HUM (H) carbon pools. The root pool has a relatively short lifetime, but does not reach equilibrium until the wood has reached equilibrium, because of the way their production rates are linked. In a similar way, the DPM has a short lifetime, but its production rate is dependent on the total wood mass. We will come back to how this was dealt with later, and assume for now that these pools do reach equilibrium after a few years.

The equations for the four long lived carbon pools could then be solved analytically, based on the yearly average production and loss rate terms. In the following equations W, R, B and H denote the mass of the carbon pools, and Px denotes the production rate and lx the loss rate constant of carbon pool X, both averaged over a year. Px,y is the production rate of pool Y from pool X averaged over a year, fx,y is the part of the loss rate constant of carbon pool X that is transferred to Y, and Lc,x is the production rate of carbon pool X from litter from living parts excluding wood, averaged over a year. When considering which pools contribute to which (described in Section 3.1.2 and Section 3.1.3), the four equilibrium masses are then given as:

$$W = \frac{P_W}{l_W} \qquad 4\text{-}7$$

$$R = \frac{P_R}{l_R} = \frac{(f_{W,R} * W + L_{c,R})}{l_R} = \frac{(f_{W,R} * \frac{P_W}{l_W} + L_{c,R})}{l_R} \qquad 4\text{-}8$$

$$B = \frac{P_B}{l_B} = \frac{f_{R,B} * R + f_{H,B} * H + P_{D,B}}{l_B} \qquad 4\text{-}9$$

$$H = \frac{P_H}{l_H} = \frac{f_{R,H} R + f_{B,H} * B + P_{D,H}}{l_H} \qquad 4\text{-}10$$

These equations show that when all the average values are known, W can be found directly. Having W, we can also find R. B and H can be found when combining their equations, which gives the following equation for B:

$$B = \frac{R\left(f_{R,B} l_H + f_{H,B} f_{R.H}\right) + f_{H,B} P_{D,H} + P_{D,B} l_H}{l_B l_H - f_{H,B} f_{B,H}} \qquad 4\text{-}11$$

This gives us an equilibrium solution for all the long lived carbon pools on a yearly average.

There are, however, some issues that arise when implementing the above describe EA. First of all, we assume that the other variables in the model are in equilibrium. For that to be the case, a certain spin-up time is needed. The average fluxes from the first year after the spin-up period could then be used as a basis for the adjustment of the slow carbon pools at the end of that year. Secondly, there is a problem with the wood loss rate constant (l_W), which is a combination of the maintenance respiration and the growth respiration. Whereas the maintenance rate constant is actually the same for all years, a growth rate constant cannot be found for all years as the wood growth respiration is not a linear function of wood mass. Nor will the growth respiration be zero at steady state, as there will always be some growth during spring and summer that is balanced by a net loss during fall and winter.

To deal with these problems, the carbon pools were adjusted several times with new calculations of average values between each adjustment. Here the growth respiration was included in l_W, leading to a small error in the calculation of W, which decreases for each year as the yearly growth approaches the equilibrium growth. Finding the equilibrium in several steps was also beneficial in connection with the short-lived pools that are dependent on wood (root and DPM). Furthermore, the combined production rate for wood and root

minus the yearly average loss rate of root was used as the production for wood (P_W), minimizing the root problem. This assumes that the loss rate of root carbon is closer to the equilibrium value than the production rate. This was not proven mathematically, but it seemed reasonable and improved the results in the tests.

The EA method was tested with a 25 years simulation, with three different initial conditions for the carbon pools. Here a two year spin-up time was used before calculating the average values. Adjustments of the pool masses were then done after the years 3-8. Figure 4.15 shows that a close to equilibrium state is reached for all the four long lived pools[19]. When comparing the masses in the last time step, the difference was found to be in the order of a few thousandths of the mass for each pool. Based on these results, further simulations were conducted with a total of ten years of simulation time: two years spin-up time, six years with adjustments, and two years after the last adjustment, the last one being used as the equilibrium state results.

[19] This test was conducted with a different model setup with different respiration rates than the other results presented in this study, and the equilibrium values are therefore not comparable with the other results.

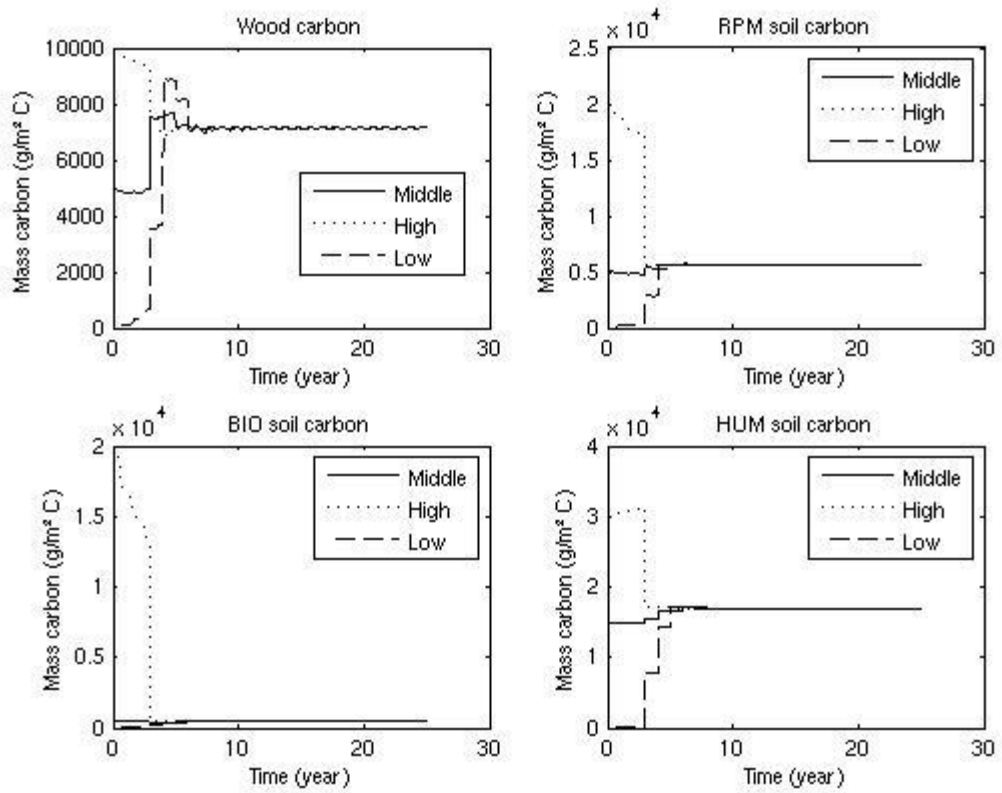

Figure 4.15: Simulated carbon masses in the wood, RPM, BIO and HUM carbon pools for a 25 year simulation with an equilibrium accelerator adjusting the masses after the years 3 to 8.

4.3.2 Results

So far we have looked at simulation results from a single column with the vegetation type 'evergreen needleleaf forest' (ENF). As many of the adjustments to the model described above were done specifically for this vegetation type, the model was considered only valid for this kind of vegetation and therefore only this vegetation type was simulated. As Figure 4.1 shows, this vegetation type covers large areas of our domain. We notice, however, that the vegetation type 'mixed forest' (MF) covers another large part of our domain. In reality, many of the same types of trees are growing in both of these groups, and excluding MF entirely from our simulations would therefore exclude a large fraction of the actual forest that is of interest in our domain. As a simple approach to account for this, half of the MF grid points were included as ENF. This was achieved by using a random generator at each grid point, with a 50% chance of changing the vegetation type from MF to ENF. The resulting domain is shown in Figure 4.16.

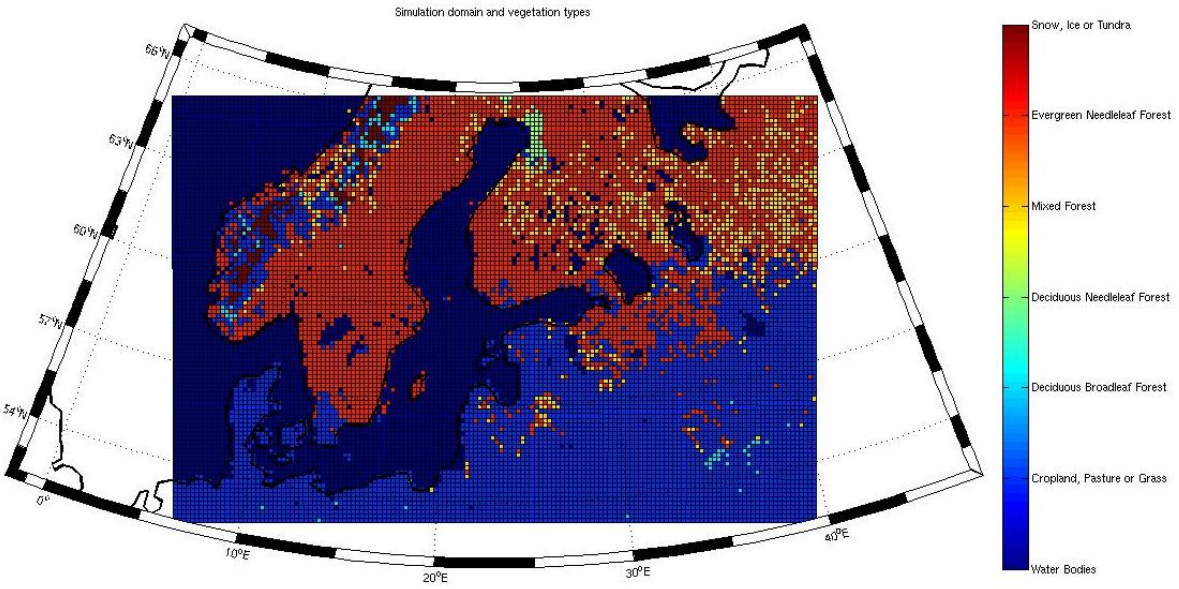

Figure 4.16: As in Figure 4.1,but having changed half the "Mixed forest" areas to "Evergreen Needleleaf Forest" with a random generator.

This domain was then used in the simulations, using forcing data from 2009, and running the model to equilibrium state with the method described above. In addition to this, the model was run with ozone and CO_2 concentrations representative of the year 1900, and the year 2100 using the SRES A2 scenario (IPCC, 2000a). In all of these simulations, the atmospheric forcing was unchanged. This gives a change in land carbon that is only due to O_3 and CO_2 effects, but excludes many important feedback mechanisms. The ozone fields for the years 1900 and 2100 were attained by multiplying the concentrations found with WRF-chem with a monthly average ozone scaling factor, which again was found by comparing results from the OsloCTM for the different years. In this way, the variations in concentrations within each individual month were retained, but the average value was adjusted. Figure 4.17 and Figure 4.18 shows the scaling factors for 1900 and 2100 respectively, averaged over the whole year. All the individual monthly adjustment factors are listed in Appendix B. The scaling factors for the year 2100 are on average substantially lower than the corresponding value of about 1.5 found when comparing the simulated global average tropospheric ozone burdens for the two years in the IPCC report (IPCC, 2001). This is, however, as expected as emissions of NO_x and VOCs are declining in Europe (Fowler et al., 2008). The development in ozone concentrations in our domain is therefore a combination of declining emissions in Europe and the counteracting effect of rising background concentrations. This is especially the case in the A2 scenario, which describes a

very heterogeneous world when it comes to technical and economic development (IPCC, 2000a), leading to large regional differences in emissions.

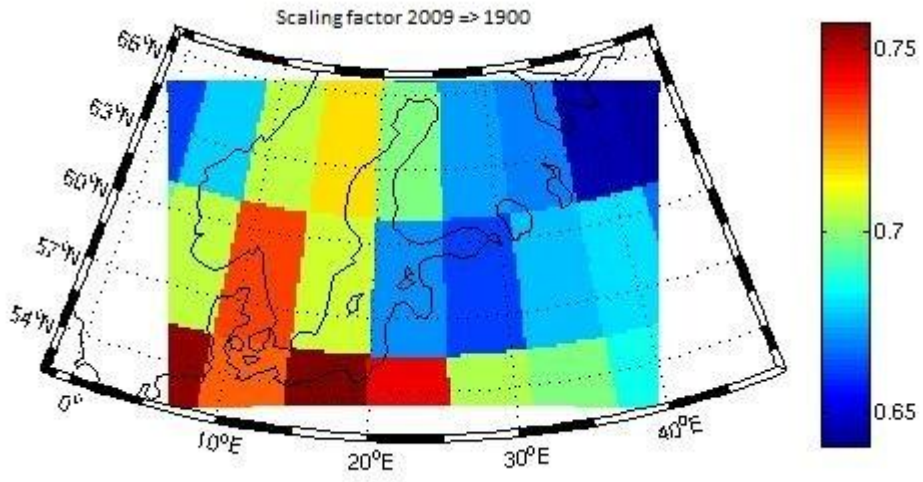

Figure 4.17: Average of 12 monthly scaling factors from 2009 to 1900, calculated from OsloCTM results for the two years.

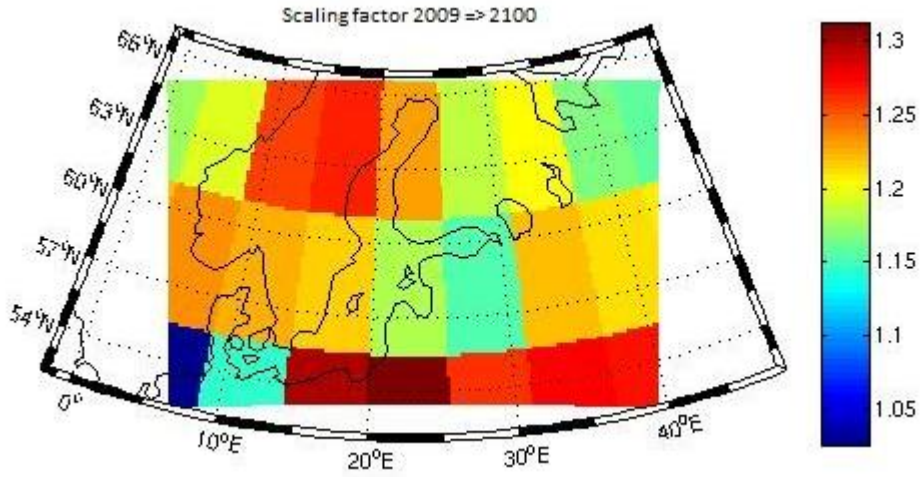

Figure 4.18: Same as Figure 4.17, but for the scaling from 2009 to 2100.

The Noah-MP model uses a single value for the CO_2 mixing ratio. For the year 1900, this was set to 300 ppm, based on figures of historical atmospheric CO_2 concentrations (Forster et al., 2007). For the years 2009 and 2100 the values were taken as the average of the two model simulations of the A2 scenario in the third IPCC assessment report, which were 388 ppm and 846 ppm respectively (IPCC, 2001). For the year 2009, observational data could have been used, but it differed from the assessment report by only a few ppm.

AOT40

Before looking at the simulated changes in carbon uptake and storage, it is interesting to look at the AOT40 for the years 1900, 2009, and 2100, as it gives a measure of damage based only on concentrations. In agreement with the LRTAP convention the AOT40 was taken to be the temporal integration over a growing season (April to October) of ozone concentrations above 40 ppb, for hours with global solar radiation above 50 W/m^2 (Mills et al., 2010). Figure 4.19 shows the results for the three years. Here one can see that the concentration in 1900 is practically never above 40 ppb during daylight hours in the growing season in our domain. In 2009, on the other hand, a considerable concentration burden can be seen in many areas. Much of southern Sweden has more than 1 ppm h AOT40, and the coastal areas in the south west of both Norway and Sweden have AOT40 values above 3 ppm h. In the northern and eastern parts of the domain, the AOT40 value is mostly well below 1 ppm h. In 2100 there is an even stronger gradient, with values as high as 12 ppm h in the south west, but well under 2 ppm h in the whole eastern part of our domain. In the southern part of Sweden, the values are around 4-6 ppm h, and declining to values below 2 ppm h towards the north of Norway and Sweden.

Together this shows a picture of high concentration burdens in south west of the domain for 2009, but declining eastward and northward. The same geographical distribution is found for 2100, but with even higher values in the most exposed areas, and sharper decline. In 1900 the concentration burden is neglectable for the whole domain when measured with the AOT40. This is interesting to have in mind when looking at the actual uptake of ozone by plants, which, as mentioned earlier, is taken to be a more reliable measure of ozone damage.

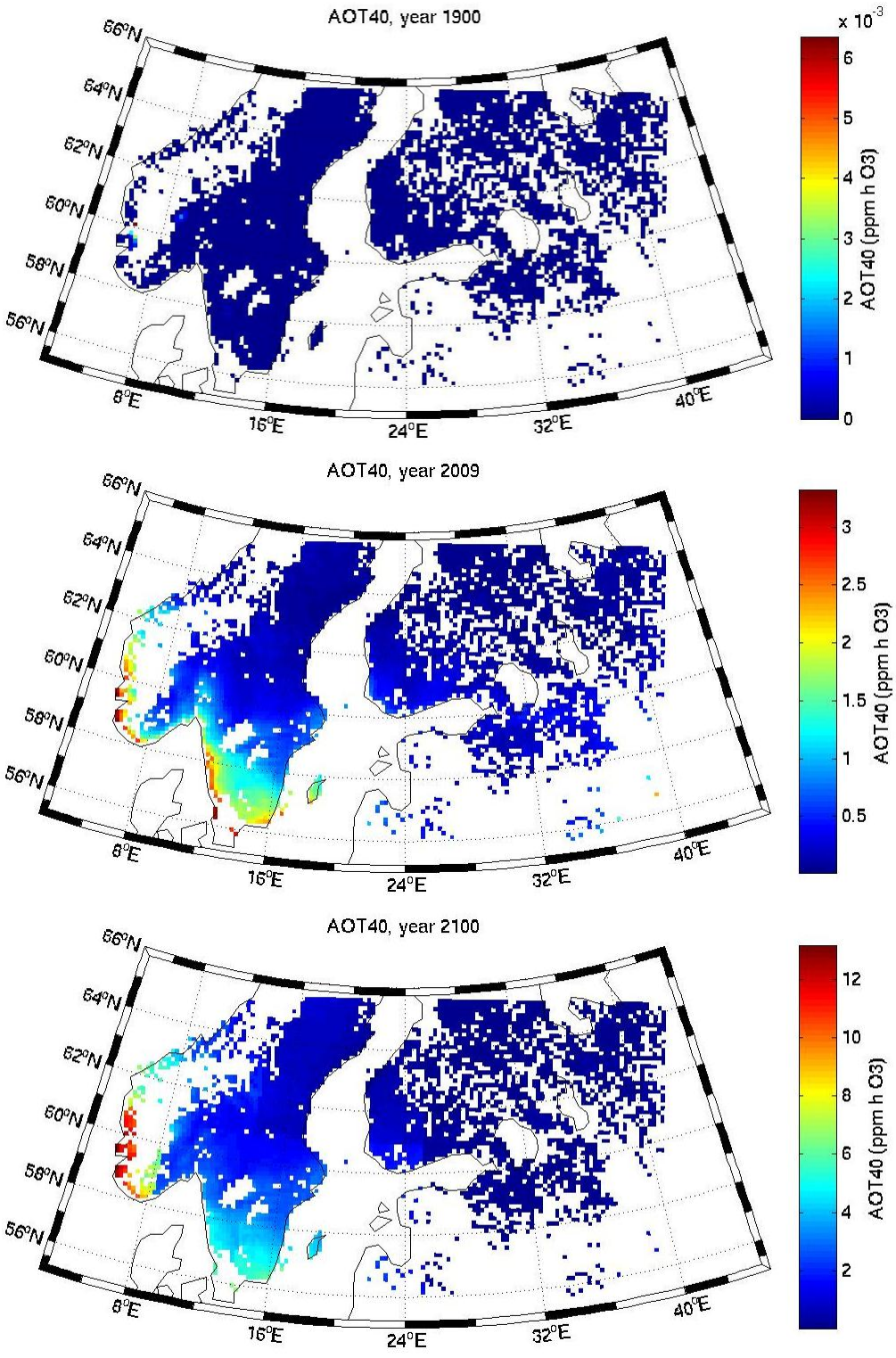

Figure 4.19: Simulated AOT40 for the Noah-MP domain (only evergreen needleleaf forest) for year 1900 (top), year 2009 (middle), and year 2100 according to the A2 scenario (bottom).

POD1.0

The POD1.0[20] for the same growing season (April to October) is shown in Figure 4.20. Here the results from the high ozone sensitivity simulations are shown. These simulations give smaller POD1.0 values than for the low sensitivity or no ozone effect cases, as the stomatal closure due to ozone is greater. The same geographical distribution of damage as found with AOT40 for 2009 and 2100 can be seen, but the values of POD1.0 are much more equal in size for the three years, with 2009 standing out as the year with the highest values. Although not directly comparable as they already include some stomatal closure due to ozone, these values are well below the critical level of 8 mmol/m^2 POD1.0, for which damage has been reported with statistical significance in the LRTAP convention (Mills et al., 2010). If we, however, assume that the flux – response function found by the LRTAP convention can be used also below this level, a POD1.0 of 1 mmol/m^2 corresponds to 0.24 % annual reduction in biomass growth, and the doses of up to about 2.5 mmol/m^2 found in southwest of Sweden correspond to an 0.6 % annual reduction in biomass growth. This assumption is in line with the method used by Sitch et al. (2007), which is used in the present study, where a flux above the threshold Y immediately results in a reduced stomatal conductance.

For the years 1900 and 2100 only coastal areas in the south west of the domain are exposed to doses above 0.4 mmol/m^2, with values in 2100 that are even smaller than in 1900. As the climate is the same for all of these simulations (same atmospheric forcing), the decline in ozone dose from 2009 to 2100 must be attributed to the increasing CO_2 concentrations, as the concentrations in themselves would give a clear increase, at least for the most exposed areas, which is evident in Figure 4.19. The effect of rising CO_2 concentrations becomes even clearer when looking at the POD1.0 found when adjusting the ozone concentrations alone to 2100 level, and keeping the CO_2 concentration at 2009 level, as shown in Figure 4.21. Here much of the same geographical distribution of ozone dose is found, but with a clear increase in the ozone dose found for the whole southern part of Sweden and Norway. The eastern part of the domain does, however, see a small decrease in ozone dose rather than increase, reflecting the low adjustment factors for the summer months from the OsloCTM simulations (see Appendix B).

[20] The POD1.0 is here used as the measure of flux damage as it is the one used in the LRTAP convention for trees (Mills et al., 2010), although the actual damage was calculated with POD1.6 to be consistent with Sitch et al (2007).

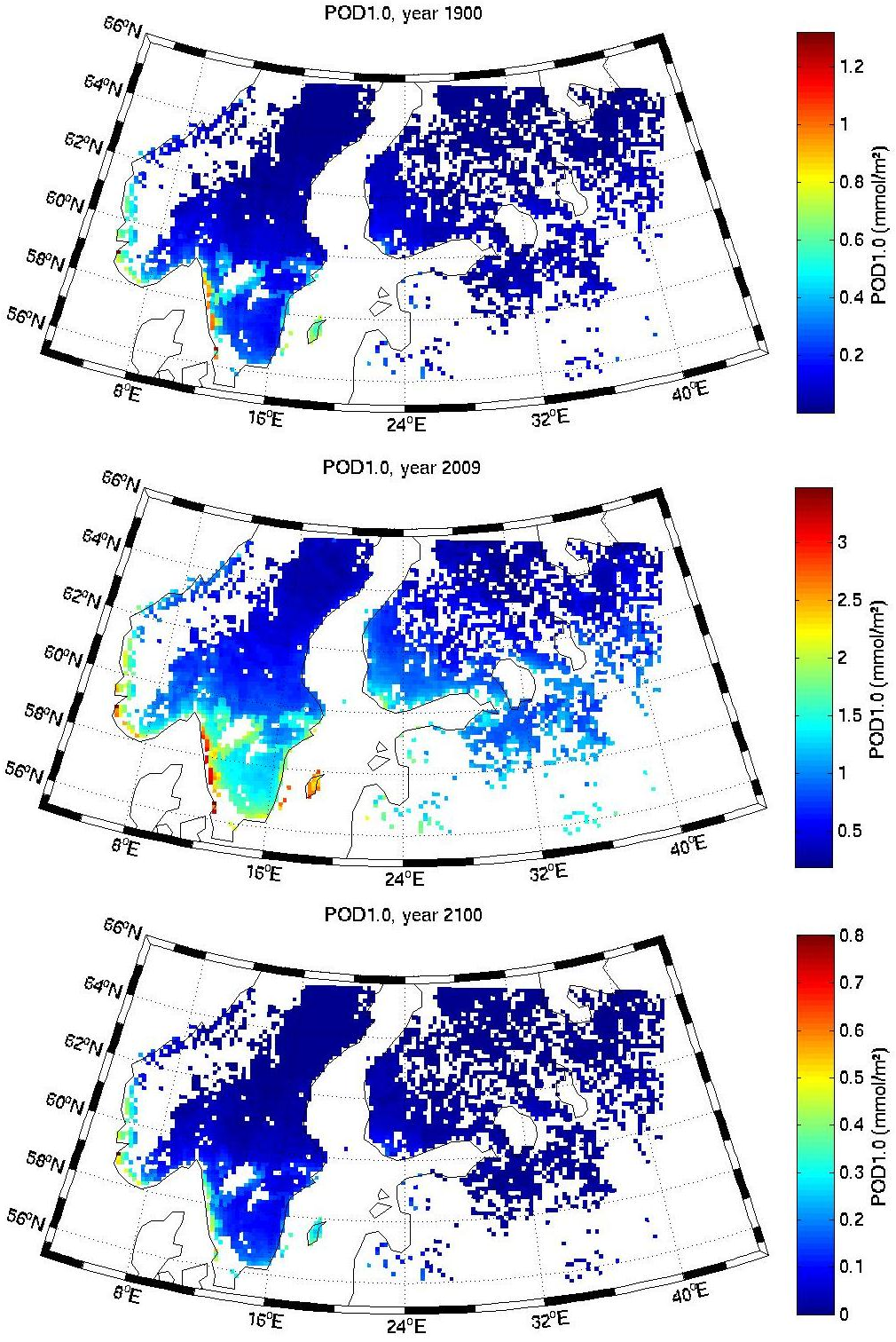

Figure 4.20: Simulated POD1.0 for the Noah-MP domain (only evergreen needleleaf forest) for the high ozone sensitivity cases, for year 1900 (top), year 2009 (middle), and year 2100 according to the A2 scenario (bottom).

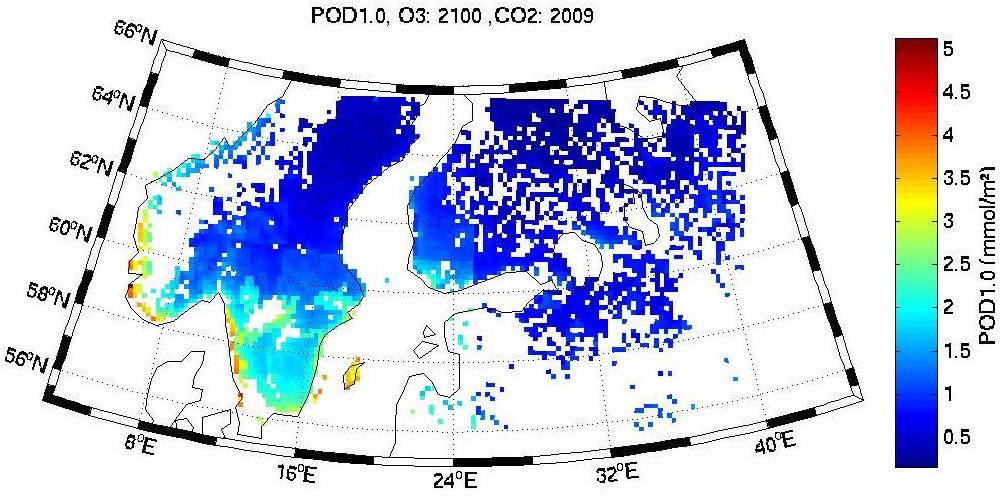

Figure 4.21: As in Figure 4.20 (bottom), but for the case with CO_2 concentration held at 2009 level.

Land carbon

The main focus of this study is how ozone affects the land carbon. Figure 4.22 shows the total land carbon (vegetation and soil) at equilibrium state for the high ozone sensitivity simulation for the year of 2009. Here the total land carbon in most of the domain is between 35 kg/m^2 and 50 kg/m^2, in good agreement with the average value of 40.8 kg/m^2 in boreal ecosystems reported by the IPCC (IPCC, 2000b), especially when considering that the equilibrium state is higher than the actual situation in 2009. In parts of Norway and Sweden, especially the mountain areas, much higher amounts of carbon can be seen. These same areas also show higher LAI (proportional to leaf carbon mass), as seen in Figure 4.23. The LAI does, however, also show very strong spatial variation that does not correspond to differences in elevation. When comparing with the different soil types in the domain, shown in Figure 4.24, it becomes clear that these differences are linked to differences in soil parameters. Most notably, there are great differences in the parameters connected to soil moisture, which is directly linked to photosynthetic rate through the β-factor described above. The soil moisture and its parameters for determining wilting point and saturation are also of great importance for the respiration rates. This can explain the strong correlation between both LAI and total land carbon with the different soil types.

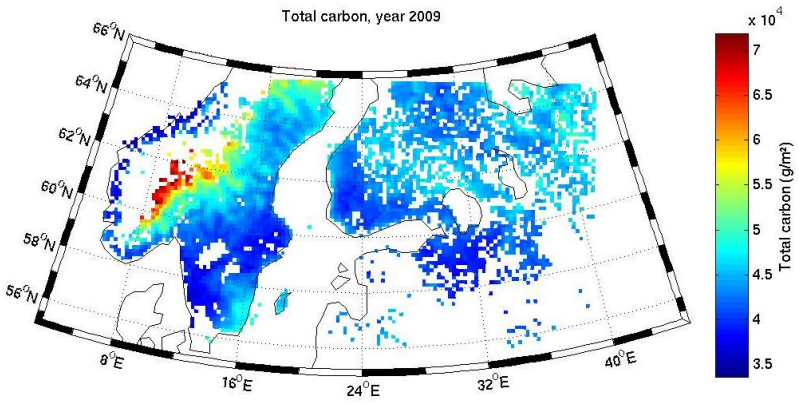

Figure 4.22: Simulated total land carbon for the Noah-MP domain (only evergreen needleleaf forest) for the high ozone sensitivity case, year 2009.

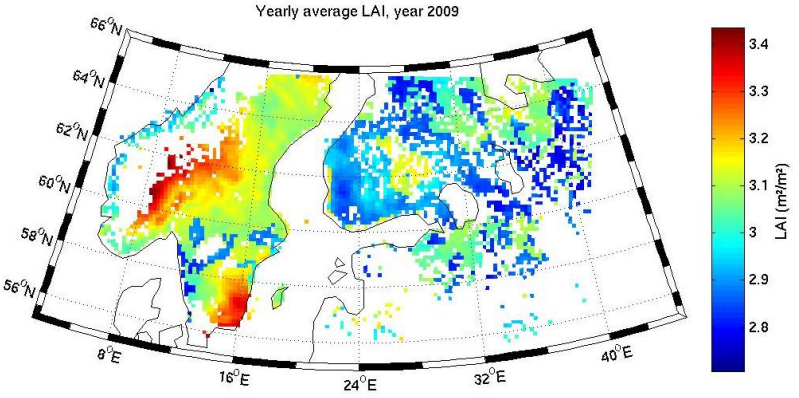

Figure 4.23: Simulated LAI for the Noah-MP domain (only evergreen needleleaf forest) for the high ozone sensitivity case, year 2009.

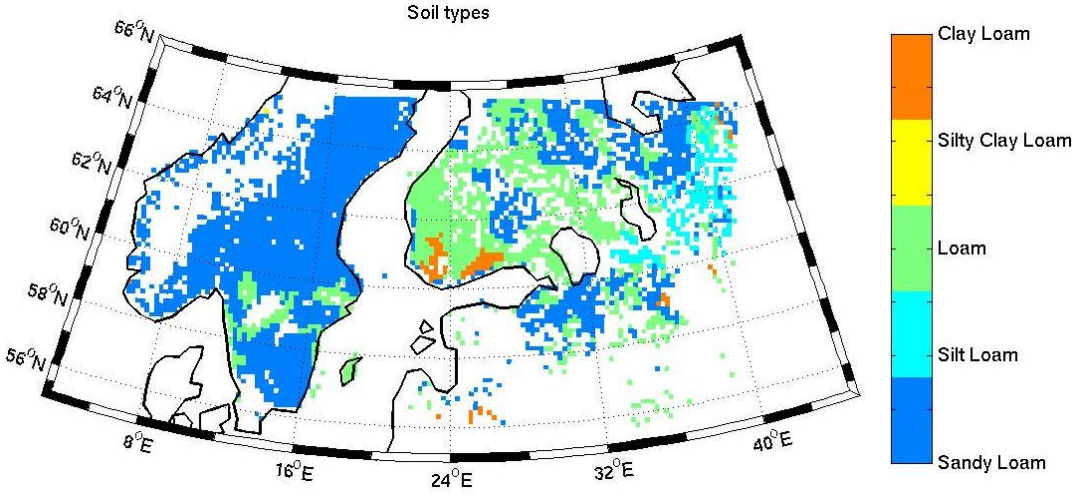

Figure 4.24: Soil types in the Noah-MP domain (only evergreen needleleaf forest) in all simulations, taken from the USGS database in WRF.

Figure 4.25 shows the reduction in total land carbon due to ozone in 2009 for the low and high sensitivity simulations, found by comparing these simulations with a simulation without

O_3 damage. Here again, the dependence on soil type is evident, with pronouncedly stronger reductions in the soil types with lower LAI. Also clear is the almost identical distribution of ozone damage in the two simulations, but with about a three times stronger reduction in carbon in the high sensitivity simulation.

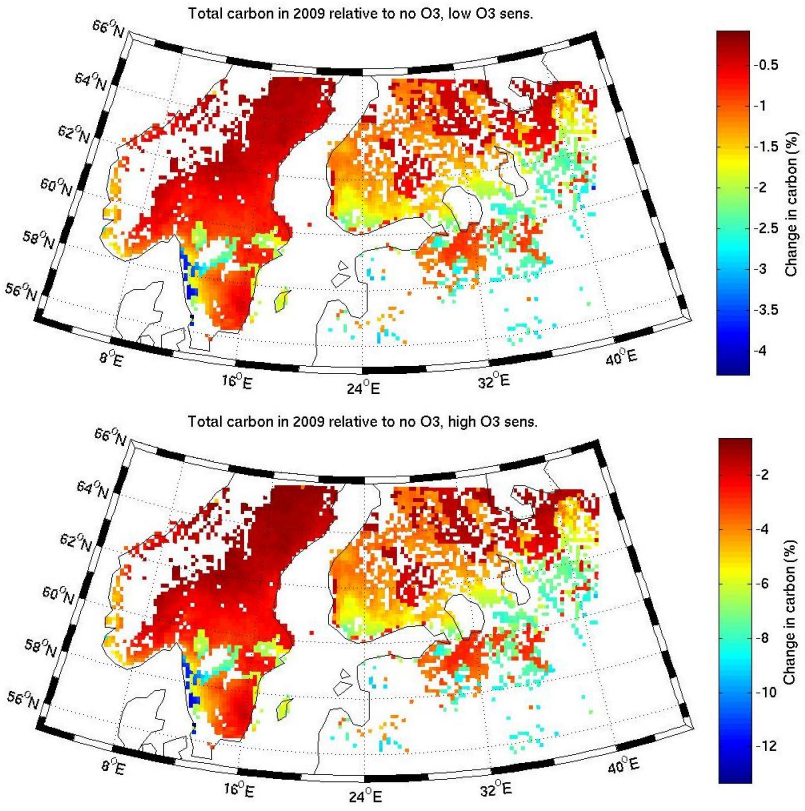

Figure 4.25: Relative change in total land carbon from no ozone damage to the low ozone sensitivity case (top) and high ozone sensitivity case (bottom) for the year of 2009.

Figure 4.26 (top) and (bottom) show the change in total carbon from 1900 to 2009 and from 2009 to 2100 for the high ozone sensitivity case, respectively. Here a general increase in stored carbon is seen in both cases, strongest for the last time interval. This reflects the increase in atmospheric CO_2 concentrations in the two periods. It is, however, interesting to see that although the relative increase in CO_2 concentrations is much stronger in the second case, 120% compared to 30%, the increase in stored carbon is only 2-3 times higher. As the increases in both ozone concentrations and fluxes are much higher between1900 and 2009 than from 2009 to 2100, this shows a strong non-linearity in the carbon storage's dependence on atmospheric CO_2, which suggests that other factors are limiting the photosynthetic rate in the latter case.

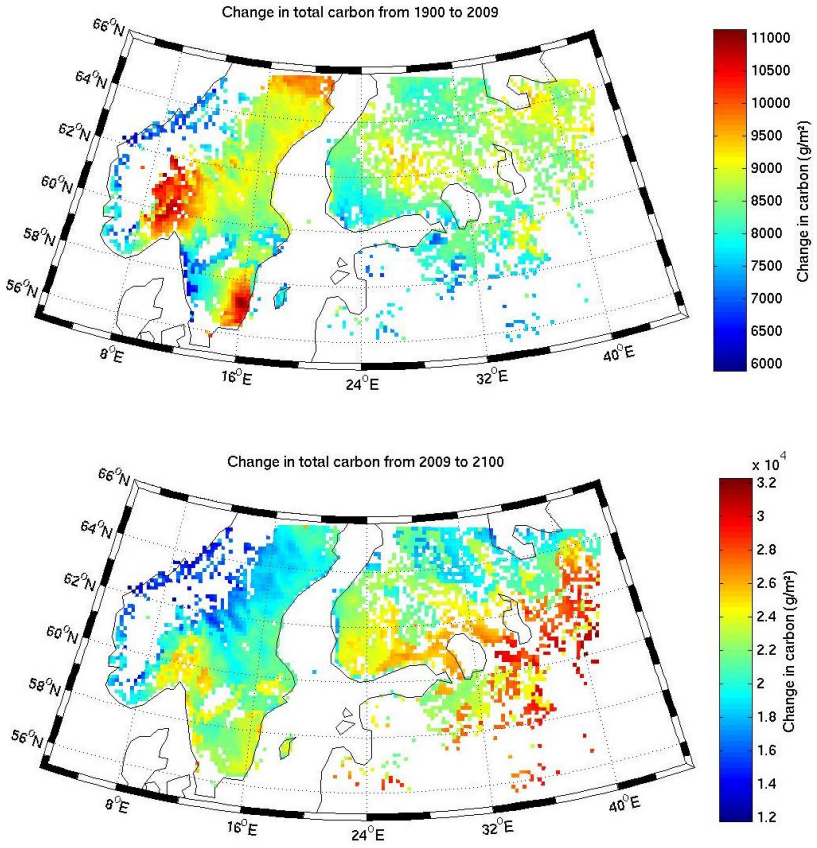

Figure 4.26: Absolute change in total land carbon for the high sensitivity cases from 1900 to 2009 (top) and 2009 to 2100 (bottom).

Figure 4.27 (top and bottom) show how much lower (or higher) the increase in land carbon for the two intervals are, compared to keeping the ozone concentrations at 1900 and 2009 levels, respectively. Here the damaging effect of ozone is clear for the first time interval, with much of the domain seeing a reduced carbon increase of 5-30 %. The spatial distribution again shows a strong correlation with soil types, and is in general much the same as for the 2009 cases compared to no ozone. For the second time interval the effect is much less pronounced, and large areas even see an increase in total stored carbon relative to the fixed ozone case. Averaged over the whole domain there is actually a small increase in total carbon, when holding the ozone concentration at 2009 levels. This is a result of the low adjustment factors from the OsloCTM simulations, discussed above.

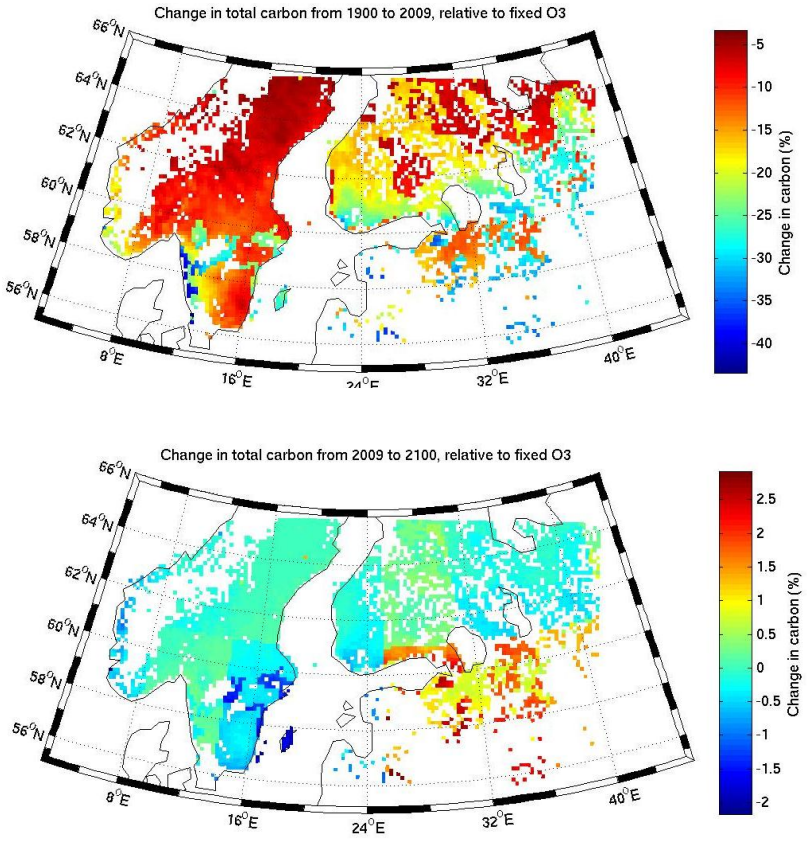

Figure 4.27: Relative change in total land carbon from 1900 to 2009, compared to ozone concentrations held at 1900 level (top), and from 2009 to 2100, compared to ozone concentrations held at 2009 level (bottom), both for the high ozone sensitivity case.

A considerable source of uncertainty in the long time carbon storage results presented here is the model setup chosen for these simulations. As we have seen, the soil parameters are of great importance for the estimated ozone damage. The Noah-MP model offers three choices for estimating the soil moisture factor (β) described in chapter 3.1.2. Ideally, one should test the importance of this for our result, but for now we can only acknowledge that this might be of importance. The choice of temperature function for soil respiration is also of great importance for the size of the soil carbon pools, as these differed considerably in magnitude. This does not influence the relative changes in total stored carbon or carbon fluxes, but will have influenced the calculations of absolute sizes and changes in this study substantially. As the two options for this function differed by approximately a factor 3, and the soil carbon pools dominate the total carbon, the absolute values in the results and the calculations of changes in atmospheric CO_2 and RF below must be considered to contain substantial uncertainties.

GPP

The GPP, being in our simulations independent of the state of all other carbon pools except the leaf pool, is a good measure of the effect of ozone for a single year, in contrast to the steady state changes we have looked at so far. Figure 4.28 shows the GPP for the year of 2009 for the high ozone sensitivity simulation. Here between 1.0 kg and 2.0 kg carbon is assimilated per m^2 per year in our domain. The highest productivity is seen in the south and in the different 'loam' soil types. These values are almost a factor 2 higher than the globally averaged values for humid boreal evergreen forest, reported by Luyssaert et al. (2007).

The effect of ozone on GPP for the year of 2009 is shown in Figure 4.29, where the relative GPP for the low and high sensitivity runs are compared to the simulation without ozone. Here we see the same geographical distribution of ozone damage as we saw with the changes in steady state total carbon, but with a smaller relative reduction and with a much greater difference between the low and high sensitivity runs, at least for the most damaged areas. Averaged over the whole domain the reduction in GPP are 0.58% and 1.86%, for the low and high sensitivity runs respectively.

Change in CO_2 concentration

The main underlying question for this study is what past, present and future ozone concentrations mean for atmospheric CO_2 concentrations and through that, the radiative balance of the atmosphere. To answer this in a proper way one would need transient simulations for the whole time of interest to get comparable results for the carbon pools with different ozone burdens. This should be done with evolving climate, and ideally also with a full coupling between the chemistry, vegetation and climate. As such simulations are far beyond what could be done with the available time and resources allotted for the present study, the following results and discussion are based on a set of rather crude estimates and should be received accordingly.

Most importantly, we need to make some assumptions about how the changes in steady state carbon pools relate to the actual change over a given time period. To do so, we must first find a single lifetime for the total carbon (vegetation and soil), and find the change in land carbon for a given period based on this, together with the change in steady state carbon presented above. This lifetime, which is the inverse of the loss rate constant (l) described

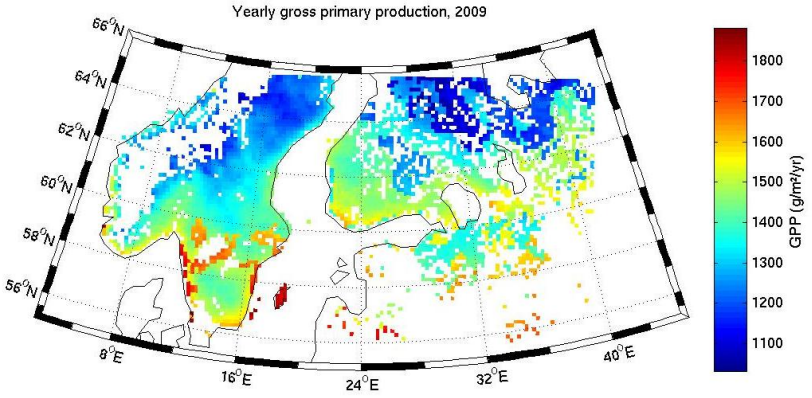

Figure 4.28: Simulated yearly GPP for the Noah-MP domain (only evergreen needleleaf forest) for the high ozone sensitivity case, year 2009.

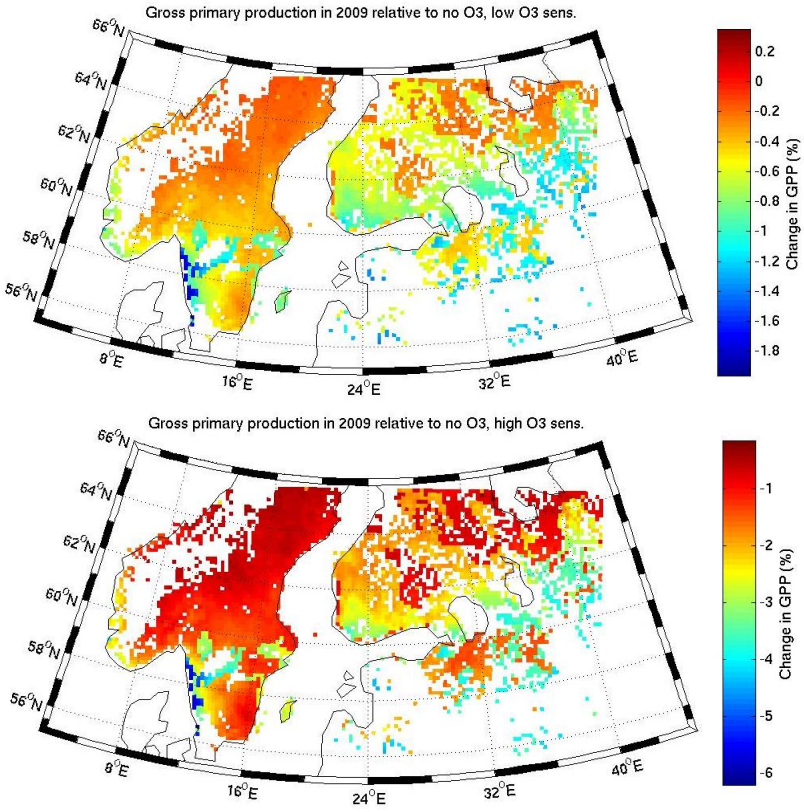

Figure 4.29: Relative change yearly GPP from no ozone damage to the low ozone sensitivity case (top) and high ozone sensitivity case (bottom) for the year 2009.

above, can be found with the mass balance equation (see Chapter 4.3.1.), which at a steady state gives:

$$\frac{1}{\tau} = l = \frac{P}{C} \qquad 4\text{-}12$$

Here τ is the lifetime, P is the production rate and C is the total mass of carbon. Treating the whole system as one, the total production rate is the GPP. The actual change in land carbon over a given time period, T, is then found as:

$$C(T) = C_{tot} * \left(1 - e^{-\frac{T}{\tau}}\right) \qquad 4\text{-}13$$

where C_{tot} is the total change in carbon at steady state.

This method was applied for the entire domain, finding the masses in each grid box by multiplying the masses per unit area presented above by the area of 15x15 km. Here the map scaling factor, which relates the area in the model to the actual geographical area, was ignored for simplicity, leading to an overestimation of the calculated area of up to about 1% for the points in the northern end of the domain. The resulting change in total carbon for the 2009 simulations with high and low sensitivity is shown in Table 4.3, including the corresponding change in global CO_2 concentrations. Here the results for a 30 years period gives an estimate of the change in land carbon now, if one assumes that the total damage of ozone for our domain corresponds to 30 years of ozone damage with 2009 concentrations. Instead of presenting the corresponding results from the year 2100 simulations, which we have seen had similar ozone damage as today when ignoring the effect of increasing CO_2, we look at the hypothetical case where the 2009 simulation would be repeated for 120 years. All the calculations here were done individually for each grid box, but on average the lifetime of carbon was estimated to about 31 years.

	Carbon (GtC)			dCO2(ppm)		
	Eq state:	**30 years:**	**120 years:**	**Eq state:**	**30 years:**	**120 years:**
Low sens.	0,39	0,24	0,39	0,19	0,11	0,18
High sens.	1,27	0,79	1,24	0,60	0,37	0,58

Table 4.3: Change in total carbon in the entire simulated Noah-MP domain at equilibrium state (Eq state), 30 years, and 120 years, calculated with a single timescale for the total carbon in each grid box, for low and high ozone sensitivities, and the corresponding change in globally averaged CO_2 concentration before adjusting for increased uptake by vegetation and the ocean.

The resulting changes in total land carbon shows that under the assumptions described above, the present day effect of ozone is quite substantial with more than half the steady state change having already taken place. Seeing the same conditions for another 90 years will bring us practically to a steady state, but the total change in carbon over these years will be considerably less than what we have seen until today.

Radiative forcing

Following Sitch et al. (2007) we can relate the change in CO_2 concentration to radiative forcing by assuming an air bourn fraction of 50%, and finding the indirect radiative forcing of ozone, RF_{O3_i}, with the following equation:

$$RF_{O3\_i} = 5.35 \ln\left(1 + \frac{dCO2(O3)}{CO2(0)}\right) \qquad 4\text{-}14$$

Here $dCO2(O3)$ is the change in atmospheric CO_2 concentration due to ozone damage and $CO2(0)$ is the pre-industrial CO_2 concentration (280 ppm). Table 4.4 shows the resulting global RF ('averaged'), and the corresponding numbers when scaling up the results to represent the whole land surface area of the earth ('scaled'). The latter can be compared with the IPCC estimate of the direct RF from tropospheric ozone in 2005, which was 0.35 (W/m^2) with the 5 to 95 % confidential level being 0.25 to 0.65 (W/m^2), respectively (Forster et al., 2007). Sitch et al (2007) found the indirect effect studied here to cover about the same range of values for the low and high sensitivity in year 2000. The values of RF found here for the scaled, 30 years case, spans almost exactly the same range of values as found by the IPCC for the direct RF of ozone as well as those found by Sitch et al. for this indirect effect. It is, however, far from clear that these scaled values should be the same as those found globally by Sitch et al., as the domain chosen for the present study contains much more carbon per unit area than the global average. On the other hand, the vegetation type studied here (evergreen needle leaf forest) is considered to be less sensitive to ozone than many other vegetation types. Also, the ozone concentrations seen in our domain are substantially lower than those seen for instance the tropics, which contain another substantial part of the earth's land carbon.

	RF averaged (mw/m^2)			RF scaled (w/m^2)		
	Eq state:	30 years:	120 years:	Eq state:	30 years:	120 years:
Low sens.	1,77	1,09	1,73	0,32	0,20	0,32
High sens.	5,71	3,53	5,57	1,04	0,65	1,02

Table 4.4: Calculated global averaged RF for the change in atmospheric CO_2 found in Table 4.3. after assuming an air borne fraction of 50 % (averaged), and when scaling up the change in CO_2 concentration with a factor relating the simulated area to the total area of land surface.

4.3.3 Simulation year and time scales

The results presented above show a clear impact of ozone in northern Europe for the present day simulations, and substantially less ozone damage in both the 1900 and the 2100 A2 simulations. Having simulated only one year in each case, even with the same meteorology for all the three cases, the resulting values for stored land carbon can, however, not be taken as measures of the actual state for the different years. The impact of ozone on the long lived soil carbon pools in 2009 could, for instance, be expected to be far less than the steady state change presented above. To get estimates of the actual state for a specific year one would have to conduct a transient simulation where both climate and concentrations were time evolving. Both the steady state results, and the 30 year and 120 year results, should therefore be seen as results for the hypothetical case of fixing climate and concentrations at a certain year, and cannot be linked directly to the actual state in any one year.

Also, because these results are based on single years repeated to steady state, it is not clear whether we can expect a steady decline in ozone damage over the next century, as the 2009 and 2100 results indicate. Instead, if the ozone concentrations in our domain increase relatively more over the next decades than the CO_2 concentrations, we might see a peak in ozone damage to vegetation sometime in the first half of this century. A transient simulation, like the one conducted by Sitch et al. (2007), could reveal whether this is the case, and show when we could expect the maximum ozone damage in our domain for this scenario, as well as the magnitude of this maximum damage. Simulating the years 2030 or 2050, in the way that 2100 was simulated in this study, could also cast some light on whether the peak of ozone damage has been reached in this domain or not.

Finally, repeating a single year over and over again makes the conditions in that year much more significant than when simulating several subsequent years. Although the year 2009 is

believed to be a representative year for the present day climate and concentrations, there might have been anomalies this year, that when repeated over and over would make the results less representative for the actual present day situation.

5. Summary and concluding remarks

5.1 Summary

In this study we have seen that ozone is of great importance for plant growth in northern Europe with present concentrations. Both the GPP and the long term carbon storage are reduced by several percent due to ozone, leading to a significant reduction in CO_2 uptake by vegetation. Here there is substantial spatial variation even for relatively similar concentrations, which coincided with variations in soil type.

This decrease in stored carbon leads to an increase in atmospheric CO_2 concentration, compared to the hypothetical case without ozone. As a very rough estimate, we find that this difference in present day CO_2 concentration could be between 0.11 and 0.37 ppm, which we estimate to have a global radiative forcing between 1.55 and 5.0 (mW/m^2) after adjusting for increase in other uptakes. This is a small number in itself, but it accounts for a very small fraction of the total land area. The global effect of ozone suppression of CO_2 uptake is probably of much greater significance.

The change in steady state total land carbon from the 1900 simulation to the 2009 simulation is offset by 5-10% in much of Sweden, 15-25% for large parts of Finland and western Russia, and as much as 40% for some areas in south west Sweden, where we find the highest ozone concentrations. This is due to the strong increase in ozone concentrations over this time period, with a relatively smaller increase in CO_2 concentrations. From 2009 to 2100 in the A2 scenario, we see the opposite with strong increase in CO_2 concentration, a relatively small increase in ozone concentration, and even a decrease in ozone concentration in some areas during the summer months. This results in a decrease in ozone damage for our domain in this period with even lower POD1.0 values in 2100 than in 1900. This is, however, not likely to be the case in most other regions of the world where emissions of ozone precursors are still rising. Combined with rising background concentrations, the continued rise in ozone precursors could give increasing ozone damage in many areas in this time period, even with increasing CO_2 concentrations.

I conclusion, these results show that we are now in a period where the effect of ozone is substantial, and measures to control emissions of ozone precursors in Europe would have a clear positive effect on carbon uptake. As both ozone and most of its precursors are

relatively short lived, the effect of reducing emissions now would have and almost immediate effect and could be important over the next decades. In the future such reductions will not have the same effect, as our results suggest that the increase in CO_2 will limit the effect of ozone through reduced stomatal conductance.

5.2 Further work

There are a number of further research projects that could be of interest in connection with the work done here. First of all, the present study is greatly limited in area and vegetation type, and is therefore not suited to give an estimate of the global effect of ozone on carbon uptake. To come closer to such an estimate it would be necessary to simulate other areas and other vegetation types. By conducting a similar study of a tropical region, e.g. the Amazonas, one could arguably improve the understanding of the global effect considerably. Including also a grassland region and a savanna region, one would represent biomes containing well above 50% of the total land carbon (IPCC, 2000b). By scaling the effect from the simulated regions with concentrations from a global CTM, we believe it would be possible to find a global estimate based on simulations with as high spatial and temporal resolution as in this study, while still using a reasonable amount of computer resources. A full global simulation would of course be desirable, but could not be carried out with the same resolution as used here.

There is also a potential to increase the robustness of the results in the present study by simulating several consecutive years, instead of just one. First of all, this would better represent the effect of ozone on different time scales, and could thereby give an estimate of the actual change in stored carbon due to ozone at a given time. Secondly, it would reduce the effect of anomalies in a given year, and therefore be more representative for the actual climate at any time.

We must also acknowledge that several ozone precursors, especially NO_2, have other important indirect effects on the climate, which should ideally be studied together with the effect studied here. In their calculation of global temperature potential for different ozone precursors, Collins et al. (2010) make estimates of the magnitude of several of these processes, including fertilization through increased nitrogen deposition and increasing nitrate aerosol formation, with a direct RF effect and an indirect effect through increased diffuse fraction of sunlight reaching vegetation, all of which have cooling effects for an increase in

NO_2. To account for such processes in some way would give a better picture of the total climate effect of ozone related chemical species.

Finally, we believe there is a potential to validate the models with observations to a greater extent than what has been done in this study. As we have seen, it was of vital importance for our results to use observations to discover unrealistic parameters in the Noah-MP model, and to get a final version that could be used with some confidence. Still, much more observational data is available, especially in Europe where the Integrated Carbon Observation System (ICOS) offers "long-term observations required to understand the present state and predict future behavior of climate, the global carbon cycle and greenhouse gases emissions" (ICOS, 2012). Comparing the calculated fluxes which these observations could offer valuable insight in how the Noah-MP model captures spatial differences in this region. In addition to the ICOS data, a global data base of data on carbon stocks and fluxes in forest ecosystems, described by Luyssaert el al. (2007) is available. In addition to offering flux data to compare with for other regions, this database could also make it possible to initiate the carbon pools in the model, making both the flux results and changes in carbon pools over time possible to simulate with a new realism.

References

Ashmore, M.R., 2005. Assessing the future global impacts of ozone on vegetation. Plant Cell and Environment, 28(8): 949-964.

Ball, J.T., Woodrow, I.E., Berry, J.A., 1987. A model predicting stomatal conductance and its contribution to the control of photosynthesis under different environmental conditions. In: Biggins, J. (Ed.), Process in Photosynthesis Research. Martinus Nijhoff, Dordrecht, Netherlands, pp. 221-224.

Clark, D.B. et al., 2011. The Joint UK Land Environment Simulator (JULES), model description - Part 2: Carbon fluxes and vegetation dynamics. Geoscientific Model Development, 4(3): 701-722.

Coleman, K., Jenkinson, D.S., 1999. ROTHC-26.3 A model for the turnover of carbon in soil. Rothamsted Research.

Collins, W.J., Sitch, S., Boucher, O., 2010. How vegetation impacts affect climate metrics for ozone precursors. Journal of Geophysical Research-Atmospheres, 115.

de Beeck, M.O., Low, M., Verbeeck, H., Deckmyn, G., 2007. Suitability of a combined stomatal conductance and photosynthesis model for calculation of leaf-level ozone fluxes. Plant Biology, 9(2): 331-341.

Denman, L.K. et al., 2007. Couplings Between Changes in the Climate System and Biogeochemistry, Climate Change 2007: The Physical Science Basis. Cambridge University Press, Cambridge, United Kingdom and New York, NY, USA.

Dickinson, R.E., Shaikh, M., Bryant, R., Graumlich, L., 1998. Interactive canopies for a climate model. Journal of Climate, 11(11): 2823-2836.

Dickson, B., Osterhus, S., 2007. One hundred years in the Norwegian Sea. Norsk Geografisk Tidsskrift-Norwegian Journal of Geography, 61(2): 56-75.

ECMWF, 2009. IFS documentation CY33r1, http://www.ecmwf.int/research/ifsdocs/CY33r1/index.html. Accessed: 29.05.2012

EMEP, 2012. http://www.emep.int/index_facts.html. Accessed: 14.04.2012

Fjæraa, A.M., Hjellbrekke, A.G., 2010. Ozone measurements 2008, Norwegian Institute of Air Research, Chemical Co-ordinating Centre og EMEP, Kjeller, Norway.

Forster, P. et al., 2007. Changes in Atmospheric Constituents and in Radiative Forcing, Climate Change 2007: The Physical Science Basis. Cambridge University Press, Cambridge, United Kingdom and New York, NY, USA.

Fowler, D. et al., 2008. Ground-level ozone in the 21st century: future trends, impacts and policy implications, The Royal Society, London, UK.

Gerosa, G. et al., 2005. Ozone uptake by an evergreen Mediterranean Forest (Quercus ilex) in Italy. Part I: Micrometeorological flux measurements and flux partitioning. Atmospheric Environment, 39(18): 3255-3266.

Hari, P., Kulmala, M., 2005. Station for measuring ecosystem-atmosphere relations (SMEAR II). Boreal Environment Research, 10(5): 315-322.

Hicks, B.B., Baldocchi, D.D., Meyers, T.P., Hosker, R.P., Matt, D.R., 1987. A PRELIMINARY MULTIPLE RESISTANCE ROUTINE FOR DERIVING DRY DEPOSITION VELOCITIES FROM MEASURED QUANTITIES. Water Air and Soil Pollution, 36(3-4): 311-330.

Hjellbrekke, A.G., Solberg, S., Fjæraa, A.M., 2011. Ozone measurements 2009, Norwegian Institute of Air Research, Chemical Co-ordinating Centre og EMEP, Kjeller, Norway.

Hodnebrog, Ø., 2008. Impacts of fine scale variability on large scale atmospheric chemistry, University of Oslo, Oslo, Norway, 99 pp.

Hodnebrog, Ø. et al., 2012. A model study of the Eastern Mediterranean ozone levels during the hot summer of 2007. Atmos. Chem. Phys. Discuss., 12(3): 7617-7675.
Hu, X.M., Nielsen-Gammon, J.W., Zhang, F.Q., 2010. Evaluation of Three Planetary Boundary Layer Schemes in the WRF Model. Journal of Applied Meteorology and Climatology, 49(9): 1831-1844.
ICOS, 2012. http://www.icos-infrastructure.eu/. Accessed: 29.05.2012
IPCC, 2000a. Emissions Scenarios, Cambridge, United Kingdom.
IPCC, 2000b. Land Use, Land Use Change and Forestry, Cambridge, United Kingdom.
IPCC, 2001. Climate Change 2001: The Scientific Basis. Contribution of Working Group 1 on the Third Assessment Report of the Intergovernmental Panel on Climate Change. Cambridge University Press, Cambridge, United Kingdom and New York, NY, USA, 881 pp.
Jacob, D.J., 1999. Introduction to Atmospheric Chemsitry. Princeton University Press, Princeton, New Jersey.
Jarvis, P.G., 1976. INTERPRETATION OF VARIATIONS IN LEAF WATER POTENTIAL AND STOMATAL CONDUCTANCE FOUND IN CANOPIES IN FIELD. Philosophical Transactions of the Royal Society of London Series B-Biological Sciences, 273(927): 593-610.
Jiang, X.Y., Niu, G.Y., Yang, Z.L., 2009. Impacts of vegetation and groundwater dynamics on warm season precipitation over the Central United States. Journal of Geophysical Research-Atmospheres, 114.
Keronen, P. et al., 2003. Ozone flux measurements over a scots pine forest using eddy covariance method: performance evaluation and comparison with flux-profile method. Boreal Environment Research, 8(4): 425-443.
Kuenen, J., van der Gon, H.D., Visschedijk, A.C., van der Brugh, H., van Gjilswijk, R., 2011. High resolution European emission inventory for the years 2003–2007 TNO, Utrecht, Netherland.
Loya, W.M., Pregitzer, K.S., Karberg, N.J., King, J.S., Giardina, C.P., 2003. Reduction of soil carbon formation by tropospheric ozone under increased carbon dioxide levels. Nature, 425(6959): 705-707.
Luyssaert, S. et al., 2007. CO(2) balance of boreal, temperate, and tropical forests derived from a global database. Global Change Biology, 13(12): 2509-2537.
Manninen, S., Huttunen, S., Tommervik, H., Hole, L.R., Solberg, S., 2009. Northern Plants and Ozone. Ambio, 38(8): 406-412.
Mills, G. et al., 2010. Chapter 3: Mapping Critical Levels for Vegetation, Manual on Methodologies and Criteria for Modelling and Mapping Critical Loads & Air Pollution Effects, Risks and Trends.
Mills, G. et al., 2011. New stomatal flux-based critical levels for ozone effects on vegetation. Atmospheric Environment, 45(28): 5064-5068.
Mitchell, K., 2005. THE COMMUNITY Noah LAND-SURFACE MODEL (LSM) User's Guide. Noah User's Guide.
NCEP/MMAB, 2012. http://polar.ncep.noaa.gov/sst/oper/Welcome.html. Accessed: 30.05.2012
Niu, G.Y. et al., 2011. The community Noah land surface model with multiparameterization options (Noah-MP): 1. Model description and evaluation with local-scale measurements. Journal of Geophysical Research-Atmospheres, 116.
Nobel, P.S., 2005. Physicochemical and Environmental Plant Physiology. Elsevier Academic Press, Burlington, MA, 567 pp.
Peckham, S.E. et al., 2011. WRF/Chem Version 3.3. User's Guide. WRF/Chem User's Guide.

Rannik, U. et al., 2002. Fluxes of carbon dioxide and water vapour over Scots pine forest and clearing. Agricultural and Forest Meteorology, 111(3): 187-202.
Rannik, U., Mammarella, I., Keronen, P., Vesala, T., 2009. Vertical advection and nocturnal deposition of ozone over a boreal pine forest. Atmospheric Chemistry and Physics, 9(6): 2089-2095.
Rydsaa, J.H., 2010. Formation of ozone due to chemical precursors and its impact on vegetation, University of Oslo, Oslo, Norway, 114 pp.
Sitch, S., Cox, P.M., Collins, W.J., Huntingford, C., 2007. Indirect radiative forcing of climate change through ozone effects on the land-carbon sink. Nature, 448(7155): 791-U4.
Skamarock, W.C. et al., 2008. A Description of the Advanced Research WRF Version 3, NCAR TECHNICAL NOTE.
Sovde, O.A., Gauss, M., Smyshlyaev, S.P., Isaksen, I.S.A., 2008. Evaluation of the chemical transport model Oslo CTM2 with focus on arctic winter ozone depletion. Journal of Geophysical Research-Atmospheres, 113(D9).
Stockwell, W.R., Middleton, P., Chang, J.S., Tang, X.Y., 1990. THE 2ND GENERATION REGIONAL ACID DEPOSITION MODEL CHEMICAL MECHANISM FOR REGIONAL AIR-QUALITY MODELING. Journal of Geophysical Research-Atmospheres, 95(D10): 16343-16367.
Wang, W. et al., 2012. ARW Version 3 Modeling System User's Guide. Mesoscale & Microscale Meteorology Division - NCAR.
Wesely, M.L., 1989. PARAMETERIZATION OF SURFACE RESISTANCES TO GASEOUS DRY DEPOSITION IN REGIONAL-SCALE NUMERICAL-MODELS. Atmospheric Environment, 23(6): 1293-1304.
Yang, Z.L. et al., 2011. The community Noah land surface model with multiparameterization options (Noah-MP): 2. Evaluation over global river basins. Journal of Geophysical Research-Atmospheres, 116.
Zeng, X.B., Beljaars, A., 2005. A prognostic scheme of sea surface skin temperature for modeling and data assimilation. Geophysical Research Letters, 32(14).

Appendix A

Full namelist for the WRF-chem simulations (shown for January 2009):

```
&time_control
 run_days                            =30,
 run_hours                           = 0,
 run_minutes                         = 0,
 run_seconds                         = 0,
 start_year                          = 2009, 2999, 2999,
 start_month                         = 01,   06,   06,
 start_day                           = 01,   11,   11,
 start_hour                          = 23,   12,   12,
 start_minute                        = 45,   00,   00,
 start_second                        = 00,   00,   00,
 end_year                            = 2009, 2999, 2999,
 end_month                           = 01,   06,   06,
 end_day                             = 31,   12,   12,
 end_hour                            = 45,   12,   12,
 end_minute                          = 00,   00,   00,
 end_second                          = 00,   00,   00,
 interval_seconds                    = 21600,
 input_from_file                     = .false.,.true.,.true.,
 history_interval                    = 60,   60,   60,
 frames_per_outfile                  = 24, 1000, 1000,
 restart                             = .true.,
 restart_interval                    = 1440,
 auxinput4_inname                    = "wrflowinp_d<domain>"
 auxinput4_interval                  = 360, 360, 360,
 auxinput5_interval_m                = 60, 60, 60
 io_form_history                     = 2
 io_form_restart                     = 2
 io_form_input                       = 2
 io_form_boundary                    = 2
 io_form_auxinput4                   = 2
 io_form_auxinput5                   = 2
 io_form_auxinput6                   = 2
 debug_level                         = 00
 /

 &domains
 time_step                           = 90,
 time_step_fract_num                 = 0,
 time_step_fract_den                 = 1,
 max_dom                             = 1,
 e_we                                = 150,    112,   94,
 e_sn                                = 100,    97,    91,
 e_vert                              = 35,    20,    20,
 dx                                  = 15000, 20000, 6666.66,
 dy                                  = 15000, 20000, 6666.66,
 p_top_requested                     = 5000,
 num_metgrid_levels                  = 38,
 num_metgrid_soil_levels             = 4,
```

```
 eta_levels                          =
1.0,0.996,0.99,0.98,0.97,0.96,0.95,0.94,0.93,0.92,0.91,0.895,0.88,0
.865,0.85,0.82,0.779,0.729,0.678,0.592,0.514,0.443,0.380,0.324,0.27
3,0.228,0.188,0.152,0.121,0.094,0.069,0.048,0.030,0.014,0.000
 grid_id                             = 1,     2,     3,
 parent_id                           = 0,     1,     2,
 i_parent_start                      = 1,     30,    30,
 j_parent_start                      = 1,     20,    30,
 parent_grid_ratio                   = 1,     3,     3,
 parent_time_step_ratio              = 1,     3,     3,
 feedback                            = 0,
 smooth_option                       = 0,
 /

 &physics
 mp_physics                          = 4,     2,     2,
 progn                               = 0,     0,     0,
 naer                                = 1e9
 ra_lw_physics                       = 1,     1,     1,
 ra_sw_physics                       = 2,     2,     2,
 radt                                = 15,    10,    10,
 sf_sfclay_physics                   = 1,     1,     1,
 sf_surface_physics                  = 2,     2,     2,
 bl_pbl_physics                      = 1,     1,     1,
 bldt                                = 0,     0,     0,
 cu_physics                          = 5,     5,     0,
 cudt                                = 0,     1,     1,
 isfflx                              = 1,
 ifsnow                              = 1,
 icloud                              = 1,
 surface_input_source                = 1,
 num_soil_layers                     = 4,
 sf_urban_physics                    = 0,     0,     0,
 maxiens                             = 1,
 maxens                              = 3,
 maxens2                             = 3,
 maxens3                             = 16,
 ensdim                              = 144,
 cu_rad_feedback                     = .true.,
 cu_diag                             = 1,
 sst_update                          = 1,
 tmn_update                          = 1,
 lagday                              = 150,
 sst_skin                            = 1,
 /

 &dynamics
 w_damping                           = 0,
 diff_opt                            = 1,
 km_opt                              = 4,
 diff_6th_opt                        = 0,       0,       0,
 diff_6th_factor                     = 0.12,    0.12,    0.12,
 base_temp                           = 290.
 damp_opt                            = 0,
 zdamp                               = 5000.,   5000.,   5000.,
 dampcoef                            = 0.2,     0.2,     0.2
```

```
khdif                               = 0,      0,      0,
kvdif                               = 0,      0,      0,
non_hydrostatic                     = .true., .true., .true.,
moist_adv_opt                       = 2,      1,      1,
scalar_adv_opt                      = 2,      1,      1,
chem_adv_opt                        = 2,      1,      1,
/

&bdy_control
spec_bdy_width                      = 5,
spec_zone                           = 1,
relax_zone                          = 4,
specified                           = .true., .false.,.false.,
nested                              = .false., .true., .true.,
/

&chem
kemit                               = 5,
chem_opt                            = 1,        2,
bioemdt                             = 1.5,       30,
photdt                              = 15,       30,
chemdt                              = 1.5,       2.,
!frames_per_emissfile               = 12,
io_style_emissions                  = 1,
emiss_inpt_opt                      = 1,        1,
emiss_opt                           = 2,        3,
chem_in_opt                         = 0,        0,
phot_opt                            = 3,        1,
gas_drydep_opt                      = 1,        1,
aer_drydep_opt                      = 1,        1,
bio_emiss_opt                       = 3,        1,
dust_opt                            = 0,
dmsemis_opt                         = 0,
seas_opt                            = 0,
gas_bc_opt                          = 1,        1,
gas_ic_opt                          = 1,        1,
aer_bc_opt                          = 1,        1,
aer_ic_opt                          = 1,        1,
gaschem_onoff                       = 1,        1,
aerchem_onoff                       = 0,        1,
wetscav_onoff                       = 0,        0,
cldchem_onoff                       = 0,        0,
vertmix_onoff                       = 1,        1,
chem_conv_tr                        = 1,        1,
biomass_burn_opt                    = 0,        0,
plumerisefire_frq                   = 30,       30,
aer_ra_feedback                     = 0,        0,
have_bcs_chem                       = .true., .false.,
/

&namelist_quilt
nio_tasks_per_group = 0,
nio_groups = 1,
/
```

Appendix B

Scaling factor from 2009 O3 concentrations to 1900 O3 concentrations (cell average longitude (horizontal) and latitude (vertical) in bold):

	0	**5,625**	**11,25**	**16,875**	**22,5**	**28,125**	**33,75**	**39,375**	**45**
	January								
63,68	0,848	0,903	0,941	0,925	0,914	0,874	0,794	0,738	0,721
58,14	0,977	1,047	1,135	1,039	1,009	1,048	1,056	1,023	1,007
52,61	1,235	1,274	1,420	1,460	1,449	1,335	1,330	1,280	1,189
	February								
63,68	0,996	1,079	1,282	1,470	1,375	1,345	1,362	1,299	1,276
58,14	1,097	1,190	1,424	1,262	1,107	1,184	1,223	1,238	1,192
52,61	1,477	1,498	1,452	1,363	1,322	1,200	1,239	1,157	1,127
	March								
63,68	0,835	0,846	0,864	0,890	0,909	0,854	0,857	0,854	0,827
58,14	0,886	0,933	1,005	0,919	0,910	0,940	0,867	0,860	0,815
52,61	0,995	1,076	0,950	0,946	0,928	0,871	0,919	0,924	0,910
	April								
63,68	0,688	0,704	0,705	0,667	0,624	0,551	0,534	0,521	0,511
58,14	0,711	0,766	0,754	0,672	0,605	0,556	0,529	0,544	0,555
52,61	0,815	0,891	0,681	0,630	0,593	0,559	0,525	0,558	0,549
	May								
63,68	0,591	0,566	0,531	0,518	0,508	0,467	0,488	0,497	0,483
58,14	0,643	0,607	0,529	0,538	0,532	0,512	0,512	0,541	0,555
52,61	0,583	0,558	0,465	0,516	0,508	0,531	0,539	0,543	0,574
	June								
63,68	0,635	0,612	0,569	0,497	0,487	0,406	0,418	0,408	0,385
58,14	0,629	0,581	0,543	0,567	0,474	0,372	0,380	0,416	0,410
52,61	0,521	0,457	0,424	0,500	0,492	0,438	0,428	0,442	0,479
	July								
63,68	0,519	0,474	0,461	0,450	0,487	0,481	0,501	0,485	0,478
58,14	0,509	0,462	0,443	0,477	0,441	0,378	0,438	0,458	0,485
52,61	0,546	0,514	0,485	0,508	0,476	0,474	0,477	0,466	0,476
	August								
63,68	0,473	0,478	0,478	0,464	0,434	0,415	0,463	0,492	0,509
58,14	0,495	0,498	0,480	0,502	0,478	0,436	0,485	0,499	0,519
52,61	0,502	0,436	0,432	0,478	0,501	0,513	0,503	0,478	0,484
	September								
63,68	0,490	0,473	0,461	0,453	0,419	0,380	0,382	0,387	0,399
58,14	0,498	0,476	0,453	0,453	0,423	0,374	0,393	0,418	0,434
52,61	0,515	0,488	0,487	0,508	0,492	0,468	0,446	0,486	0,514
	October								
63,68	0,585	0,600	0,627	0,642	0,621	0,636	0,615	0,574	0,575
58,14	0,576	0,565	0,579	0,580	0,555	0,537	0,569	0,572	0,552

52,61	0,610	0,563	0,550	0,577	0,583	0,534	0,502	0,531	0,555
	Noveber								
63,68	0,529	0,549	0,588	0,599	0,606	0,632	0,634	0,587	0,628
58,14	0,519	0,502	0,491	0,511	0,552	0,591	0,635	0,645	0,630
52,61	0,484	0,461	0,511	0,596	0,622	0,636	0,625	0,616	0,592
	Deceber								
63,68	0,762	0,852	0,972	1,020	0,999	1,041	0,972	0,901	0,927
58,14	0,782	0,845	0,983	0,969	0,966	1,020	1,042	0,943	0,865
52,61	0,841	0,835	0,930	1,010	0,965	0,889	0,847	0,758	0,700

Scaling factor from 2009 O3 concentrations to 2100 O3 concentrations (cell average longitude (horizontal) and latitude (vertical) in bold):

	0	**5,625**	**11,25**	**16,875**	**22,5**	**28,125**	**33,75**	**39,375**	**45**
	January								
63,68	1,253	1,283	1,337	1,304	1,165	1,087	1,022	0,940	0,991
58,14	1,407	1,424	1,489	1,348	1,266	1,263	1,400	1,364	1,375
52,61	1,652	1,478	1,649	1,816	1,954	1,848	1,879	1,804	1,777
	February								
63,68	1,350	1,469	1,772	2,053	1,929	1,948	2,015	1,952	1,909
58,14	1,530	1,646	1,911	1,674	1,534	1,812	1,972	1,999	1,864
52,61	2,045	1,966	1,883	1,815	1,920	1,852	2,035	2,072	2,099
	March								
63,68	1,224	1,257	1,316	1,358	1,382	1,293	1,325	1,338	1,298
58,14	1,376	1,463	1,546	1,423	1,445	1,490	1,386	1,349	1,297
52,61	1,318	1,349	1,288	1,444	1,492	1,408	1,492	1,502	1,540
	April								
63,68	1,201	1,218	1,276	1,233	1,207	1,014	0,972	0,958	0,931
58,14	1,293	1,428	1,402	1,292	1,215	1,013	0,964	0,940	1,004
52,61	1,160	1,272	1,190	1,247	1,176	1,099	1,010	1,040	1,083
	May								
63,68	1,286	1,248	1,182	1,112	1,092	0,998	1,070	1,114	1,081
58,14	1,523	1,411	1,096	1,139	1,215	1,089	1,054	1,107	1,142
52,61	0,935	0,963	1,023	1,117	1,030	1,044	1,064	1,077	1,143
	June								
63,68	1,498	1,441	1,294	1,095	1,116	0,965	1,039	1,049	0,948
58,14	1,442	1,355	1,170	1,244	1,124	0,892	0,844	0,912	0,932
52,61	0,961	0,877	0,997	1,134	1,033	0,941	0,912	0,913	0,950
	July								
63,68	1,139	1,063	1,010	0,975	1,047	1,017	1,069	1,033	0,939
58,14	1,094	1,008	0,951	1,044	1,000	0,825	0,878	0,900	0,927
52,61	0,874	0,850	1,011	1,102	0,995	0,940	0,935	0,888	0,865
	August								
63,68	0,897	0,963	0,983	0,974	0,933	0,845	0,956	1,005	0,965
58,14	0,942	1,006	0,983	1,056	1,072	0,914	0,938	0,963	0,990
52,61	0,702	0,627	0,911	1,064	1,059	1,028	0,971	0,921	0,923
	September								
63,68	0,940	0,904	0,946	0,966	0,910	0,862	0,901	0,882	0,844
58,14	0,940	0,871	0,893	0,942	0,859	0,825	0,926	0,947	0,984
52,61	0,704	0,617	0,886	1,057	1,076	1,035	1,003	1,088	1,149
	October								
63,68	1,114	1,154	1,263	1,325	1,277	1,323	1,269	1,139	1,137
58,14	1,044	1,046	1,046	1,148	1,112	1,120	1,236	1,206	1,170
52,61	0,956	0,798	0,907	1,115	1,154	1,088	1,083	1,183	1,284
	Noveber								
63,68	0,956	0,971	1,110	1,129	1,075	1,116	1,149	1,054	1,246

58,14	0,901	0,852	0,781	0,844	0,891	0,967	1,182	1,206	1,272
52,61	0,692	0,519	0,752	1,024	1,155	1,208	1,266	1,321	1,333
	Deceber								
63,68	1,233	1,374	1,594	1,647	1,611	1,745	1,669	1,535	1,621
58,14	1,191	1,301	1,461	1,456	1,456	1,614	1,865	1,663	1,522
52,61	1,095	0,997	1,250	1,629	1,716	1,657	1,662	1,463	1,368